

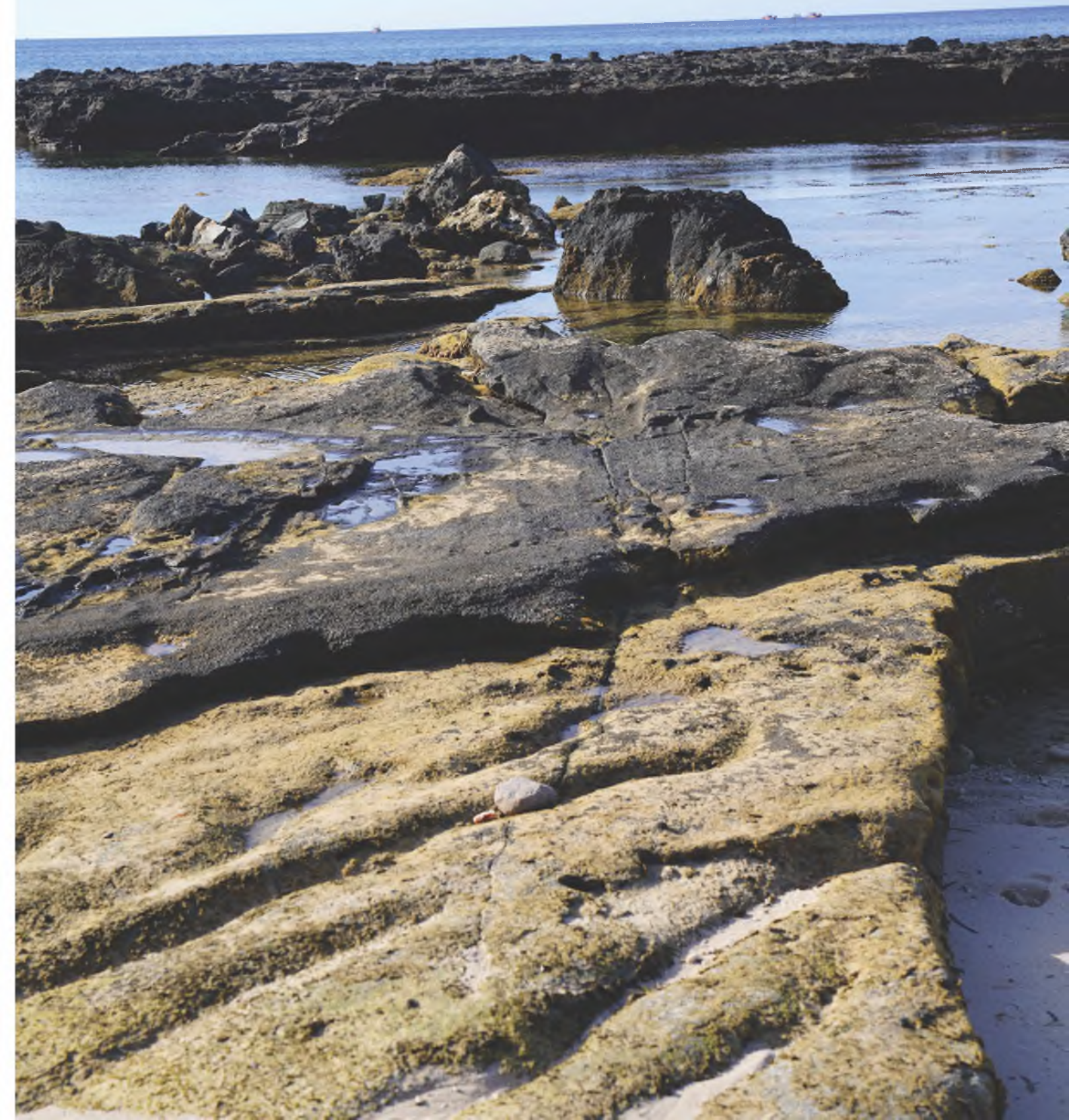
PETROVIETNAM JOURNAL



An Official Publication of the Vietnam National Oil and Gas Group Vol. 6 - 2022

ISSN 2615-9902

PETROVIETNAM Vol. 6 - 2022





EDITOR-IN-CHIEF

Dr. Le Xuan Huyen

DEPUTY EDITOR-IN-CHIEF

Dr. Le Manh Hung

Dr. Phan Ngoc Trung

EDITORIAL BOARD MEMBERS

Dr. Trinh Xuan Cuong

Dr. Nguyen Anh Duc

MSc. Vu Dao Minh

M.A. Tran Thai Ninh

MSc. Duong Manh Son

MSc. Le Ngoc Son

Assoc. Prof. Dr. Le Van Sy

Eng. Le Hong Thai

M.A. Bui Minh Tien

MSc. Nguyen Van Tuan

MSc. Pham Xuan Trung

Dr. Tran Quoc Viet

SECRETARY

MSc. Le Van Khoa

M.A. Nguyen Thi Viet Ha

DESIGNED BY

Le Hong Van

MANAGEMENT

Vietnam Petroleum Institute

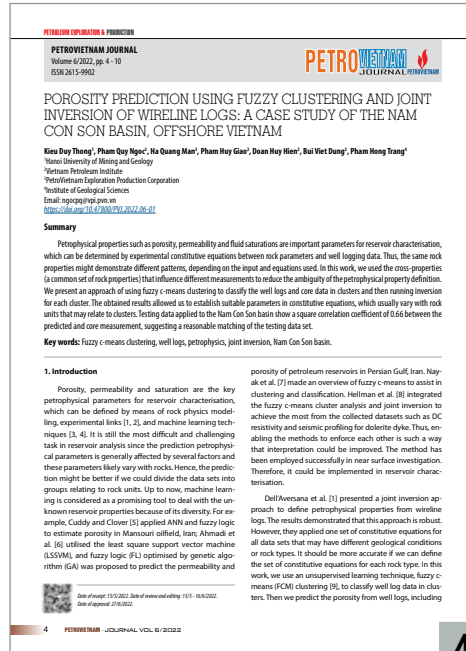
CONTACT ADDRESS

16th Floor, VPI Tower, Trung Kinh street, Yen Hoa ward, Cau Giay district, Ha Noi

*Tel: (+84-24) 37727108 * Fax: (+84-24) 37727107 * Email: tcdk@pvn.vn/pvj@pvn.vn*

Mobile: (+84)982288671

Cover photo: Ly Son Island, Quang Ngai, Vietnam. Photo: Le Van



4



11

SCIENTIFIC RESEARCH



PETROLEUM EXPLORATION & PRODUCTION

4. Porosity prediction using fuzzy clustering and joint inversion of wireline logs: A case study of the Nam Con Son basin, offshore Vietnam

11. Impact of deposition and diagenesis on quality of sandstone reservoirs: A case study in Cuu Long basin, offshore Vietnam

27. Supervised machine learning application of lithofacies classification for a hydrodynamically complex gas - condensate reservoir in Nam Con Son basin

36. Activation of a non-eruptive well by using an electrical pump to optimise production

43. Design of continuous gas-lift for a dead well and step-up of its productivity

49. Assessing the effect of gas temperature on gas well performance



PETROVIETNAM JOURNAL
 Volume 6/2022, pp. 27 - 35
 ISSN 2615-9902

PETROVIETNAM JOURNAL

SUPERVISED MACHINE LEARNING APPLICATION OF LITHOFACIES CLASSIFICATION FOR A HYDRODYNAMICALLY COMPLEX GAS - CONDENSATE RESERVOIR IN NAM CON SON BASIN

Nguyen Ngoc Tan, Tran Ngoc Thi Hong, Hoang Ky Son, Tran Vu Tung
 Nam Con Son Petroleum Operating Company (NCSOC) PSC
 Email: tanh@nscdongoc.vn
<https://doi.org/10.47862/PVJ.2022.26-35>

Summary

Conventional integration of rock physics and seismic inversion can quantitatively evaluate and contrast reservoir properties. However, the available output attributes are occasionally not a perfect indicator for specific information such as lithology or fluid saturation due to technology constraints. Each attribute commonly exhibits a combination of geological characteristics that could lead to subjective interpretations and provides only qualitative results. Meanwhile, machine learning (ML) is emerging as an independent interpreter to synthesise all parameters simultaneously, mitigate the uncertainty of biased cut-off, and objectively classify lithofacies on the accuracy scale.

In this paper, multiple classification algorithms including support vector machine (SVM), random forest (RF), decision tree (DT), K-nearest neighbours (KNN), logistic regression, Gaussian, Bernoulli, multinomial naive Bayes, and linear discriminant analysis were executed on the seismic attributes for lithofacies prediction. Initially, all data points of five seismic attributes of acoustic impedance, Lambda-Rho, Mu-Rho, density (ρ), and compressional wave to shear wave velocity (Vp/Vs) within 25-metre radius and 25-metre interval offset top and base of reservoir were orbitally extracted on 4 wells to create the datasets. Cross-validation and grid search were also implemented on the best four algorithms to optimise the hyper-parameters for each algorithm and avoid overfitting during training. Finally, confusion matrix and accuracy scores were exploited to determine the ultimate model for discrete lithofacies prediction. The machine learning models were applied to predict lithofacies for a complex reservoir in an area of 163 km².

From the perspective of classification, the random forest method achieved the highest accuracy score of 0.907 compared to support vector machine (0.896), K-nearest neighbours (0.895), and decision tree (0.892). At well locations, the correlation factor was excellent with 0.88 for random forest results versus sand thickness. In terms of sand and shale distribution, the machine learning outputs demonstrated geologically reasonable results, even in undrilled regions and reservoir boundary areas.

Key words: Lithofacies classification, reservoir characterisation, seismic attributes, supervised machine learning, Nam Con Son basin.

1. Introduction

Sand30 is a major gas - condensate reservoir in Hai Thach field. This reservoir has one exploration well and three production wells with very different production performance [1]. Many studies have been conducted to better understand, characterise and model Sand30 [1 - 4]. Reservoir extent and lithofacies distribution are the main focus of the current study.

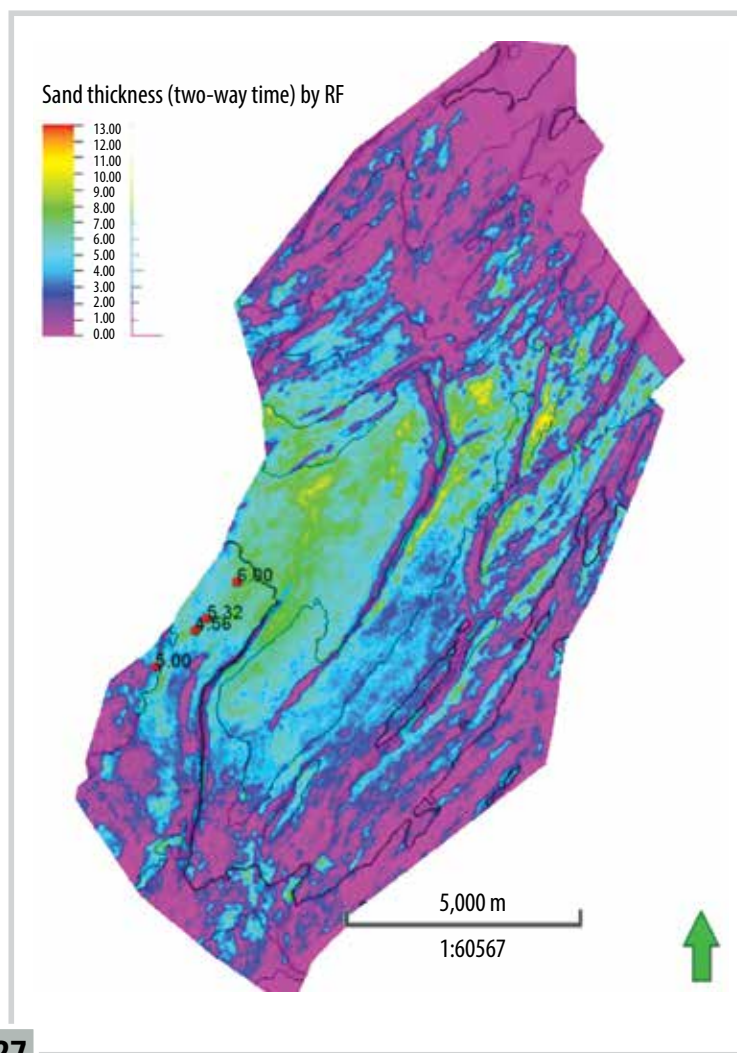
Machine learning has been shown to be capable of complementing and elevating human analysis by objectively examining input data and automatically repeating the calculation until the best output is determined. Because of this benefit, machine learning has been widely used in recent years in the oil and gas business, such as for lithofacies classification [5 - 7], depositional facies prediction [8, 9], well log correlation [10, 11], seismic facies classification [12, 13], and seismic facies analysis [14].

In this study, supervised machine learning was used to predict lithofacies using classification techniques in-

Date of receipt: 15/02/2022, Date of review and editing: 15/1 - 20/02/2022, Date of approval: 17/02/2022.

PETROVIETNAM JOURNAL, VOL. 6/2022 27

27



PETROLEUM TECHNOLOGIES

59. Micro/nanostructured ZnO-based superhydrophobic steel surface with enhanced corrosion protection

POROSITY PREDICTION USING FUZZY CLUSTERING AND JOINT INVERSION OF WIRELINE LOGS: A CASE STUDY OF THE NAM CON SON BASIN, OFFSHORE VIETNAM

Kieu Duy Thong¹, Pham Quy Ngoc², Ha Quang Man³, Pham Huy Giao², Doan Huy Hien², Bui Viet Dung², Pham Hong Trang⁴

¹Hanoi University of Mining and Geology

²Vietnam Petroleum Institute

³PetroVietnam Exploration Production Corporation

⁴Institute of Geological Sciences

Email: ngocpq@vpi.pvn.vn

<https://doi.org/10.47800/PVJ.2022.06-01>

Summary

Petrophysical properties such as porosity, permeability and fluid saturations are important parameters for reservoir characterisation, which can be determined by experimental constitutive equations between rock parameters and well logging data. Thus, the same rock properties might demonstrate different patterns, depending on the input and equations used. In this work, we used the cross-properties (a common set of rock properties) that influence different measurements to reduce the ambiguity of the petrophysical property definition. We present an approach of using fuzzy c-means clustering to classify the well logs and core data in clusters and then running inversion for each cluster. The obtained results allowed us to establish suitable parameters in constitutive equations, which usually vary with rock units that may relate to clusters. Testing data applied to the Nam Con Son basin show a square correlation coefficient of 0.66 between the predicted and core measurement, suggesting a reasonable matching of the testing data set.

Key words: Fuzzy c-means clustering, well logs, petrophysics, joint inversion, Nam Con Son basin.

1. Introduction

Porosity, permeability and saturation are the key petrophysical parameters for reservoir characterisation, which can be defined by means of rock physics modelling, experimental links [1, 2], and machine learning techniques [3, 4]. It is still the most difficult and challenging task in reservoir analysis since the prediction petrophysical parameters is generally affected by several factors and these parameters likely vary with rocks. Hence, the prediction might be better if we could divide the data sets into groups relating to rock units. Up to now, machine learning is considered as a promising tool to deal with the unknown reservoir properties because of its diversity. For example, Cuddy and Clover [5] applied ANN and fuzzy logic to estimate porosity in Mansouri oilfield, Iran; Ahmadi et al. [6] utilised the least square support vector machine (LSSVM), and fuzzy logic (FL) optimised by genetic algorithm (GA) was proposed to predict the permeability and

porosity of petroleum reservoirs in Persian Gulf, Iran. Nayak et al. [7] made an overview of fuzzy c-means to assist in clustering and classification. Hellman et al. [8] integrated the fuzzy c-means cluster analysis and joint inversion to achieve the most from the collected datasets such as DC resistivity and seismic profiling for dolerite dyke. Thus, enabling the methods to enforce each other is such a way that interpretation could be improved. The method has been employed successfully in near surface investigation. Therefore, it could be implemented in reservoir characterisation.

Dell'Aversana et al. [1] presented a joint inversion approach to define petrophysical properties from wireline logs. The results demonstrated that this approach is robust. However, they applied one set of constitutive equations for all data sets that may have different geological conditions or rock types. It should be more accurate if we can define the set of constitutive equations for each rock type. In this work, we use an unsupervised learning technique, fuzzy c-means (FCM) clustering [9], to classify well log data in clusters. Then we predict the porosity from well logs, including



Date of receipt: 15/5/2022. Date of review and editing: 15/5 - 16/6/2022.

Date of approval: 27/6/2022.

resistivity, sonic velocity, and gamma ray by means of the joint inversion method for each cluster.

2. Methodology

2.1. Constitutive equations

In this work, we use constitutive Equations (1), (2) and (3) that link rock properties with well-log measurements [2].

$$V_p = (1 - \phi)^2 V_0 + \phi V_f \tag{1}$$

$$R = \frac{1}{S_w^n \left(\frac{\phi^m}{a R_w} + \frac{v_c}{R_c} \right)} \tag{2}$$

$$GR = (1 - v_c) GR_q + v_c GR_c \tag{3}$$

where V_p , GR, and R are p-wave velocity, gamma ray and resistivity, respectively; V_0 and V_f are the compressional wave velocities of the solid matrix and the pore fluid, respectively; ϕ is the porosity of the rock; v_c is the volumetric fractions of clay; S_w is water saturation; GR_q and GR_c are the specific values of gamma ray of quartz and clay; R_w is the resistivity of water; a is the tortuosity (we set a equal to 1.0 in this work); m is the cementation exponent (1.3 and 2.5 for most sedimentary rocks, and close to 2.0 for sandstones) and n is the saturation exponent (generally assumed to be 2 but can vary as well), thus we set m and n equal 2.0 in our process. The clay fraction in Equation (2) is calculated by using gamma ray logs (Equation 3).

2.2. Using fuzzy c-means clustering

Generally, various rock units formed in different geological conditions demonstrate some particular relationships between physical parameters. If a correlation between physical parameters can be defined correctly then the formulated set of petrophysical characteristics in a unit may represent a geological unit, which is distinguished from others in terms of geophysical properties by using clustering techniques. One of the powerful data analysis techniques is “fuzzy clustering”, a method that separates data into subsets according to degrees of the measured similarity. Some studies using FCM to analyse geophysical data were conducted [10, 11].

2.3. Choosing optimal parameters for each cluster

To choose the optimal parameters in Equations (1), (2) and (3), we define the error between calculated values (Equations 1 and 2) and well logs data as follows:

$$Error = \sqrt{\frac{\sum(y_{cal} - y_{mea})^2}{N}} \tag{4}$$

where y_{cal} and y_{mea} are calculated and measured values, respectively; N is number of samples. When the Error is minimum, the parameters are supposed to be optimal.

2.4. Inversion

Forward modelling: The V_p and resistivity are linked to porosity and fluid saturation by using constitutive equations as seen in Equations (1) and (2).

Inversion: The objective function is defined as the sum of the L2 norms of the misfits between the measurements d^{mea} (V_p and electrical well logs) and the data d^{cal} from the coupled-models; the inverse problem solution \tilde{m} is obtained, at each depth location, by minimising the objective function within the domain Ω_m of the model parameters.

$$\tilde{m} = argmin_{m \in \Omega_m} \sum_{lo=1}^{N_{lo}} w_i \|d_{lo}^{mea} - d_{lo}^{cal}\|_2 + \beta \|m - m_0\|_2 \tag{5}$$

where lo is the number of well logs used in the system of equations (in our case $lo = 2$ for V_p and resistivity) and w_i is the weight to scale the influence of each log due to different scales and noise levels of the well log measurements. β is the regularisation parameter and m_0 is the initial model parameters.

3. Case study of Nam Con Son basin

The Nam Con Son basin is one of the largest Tertiary sedimentary basins offshore Vietnam. It is situated in the southern

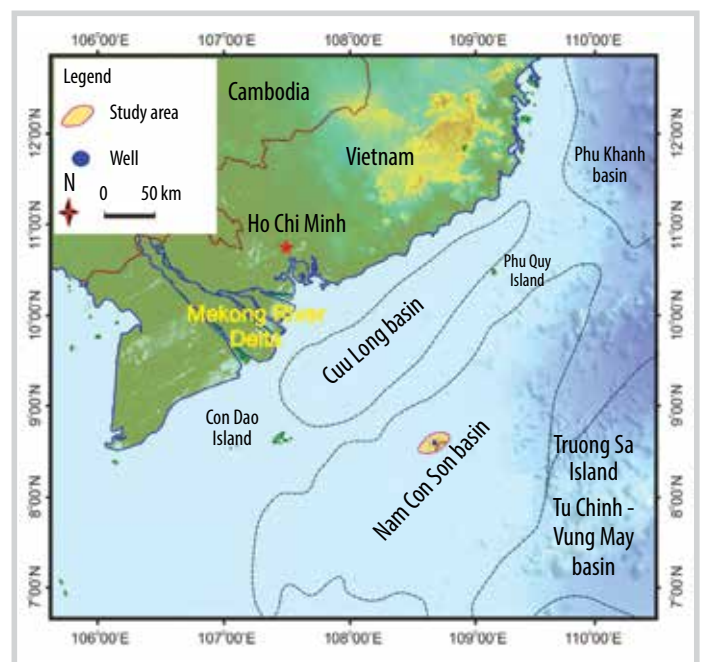


Figure 1. Location of the Nam Con Son basin within the East Vietnam Sea [12].

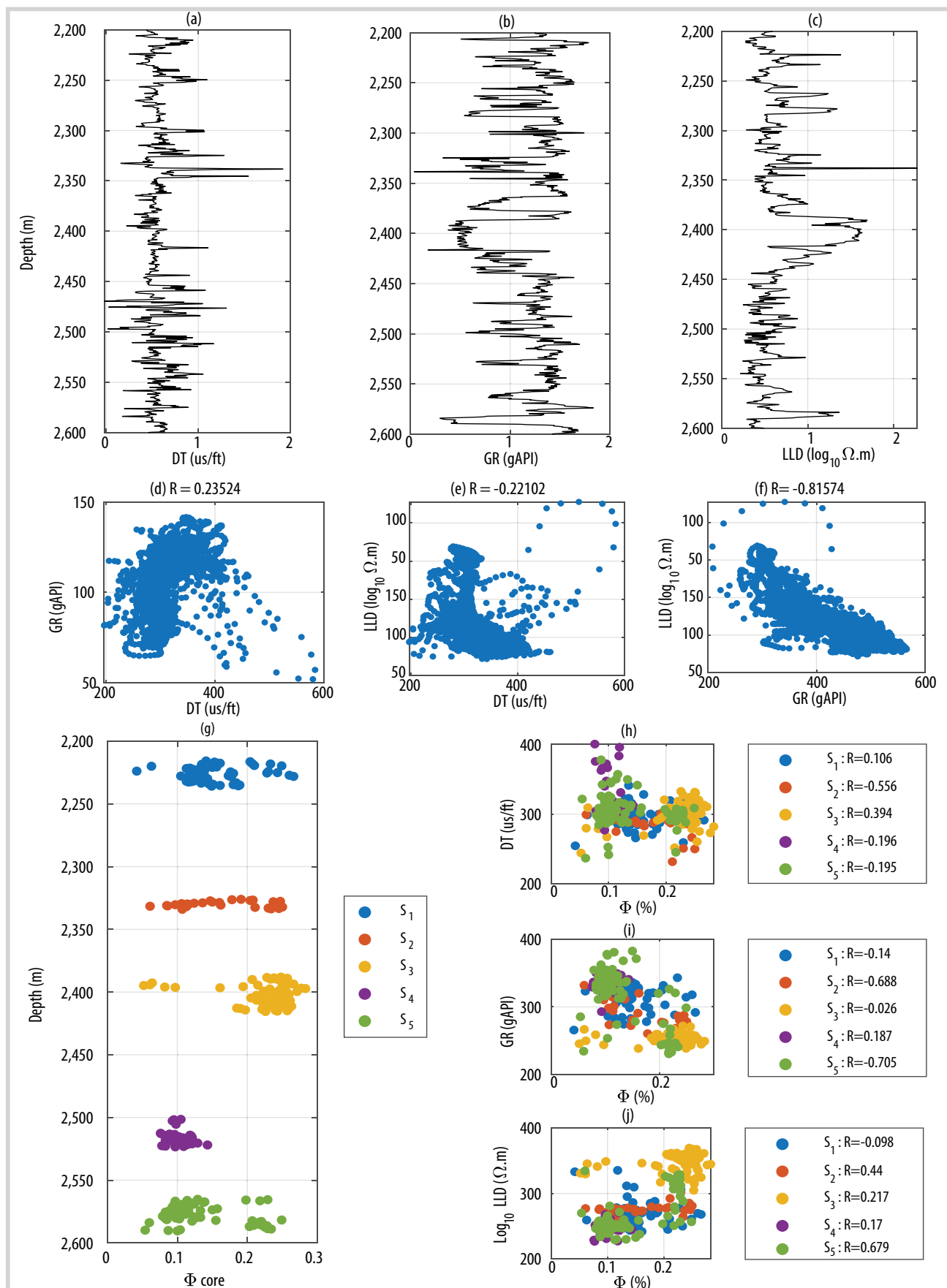


Figure 2. Well logs and core data: (a) p-wave travel time; (b) gamma ray; (c) resistivity; (d), (e), (f) correlation between well log curves; (g) porosity of core measurement at five depth sections: S1, S2, S3, S4, and S5; and (h), (i), (j) correlation between well logs and porosity of core measurement with colour coded by depth sections.

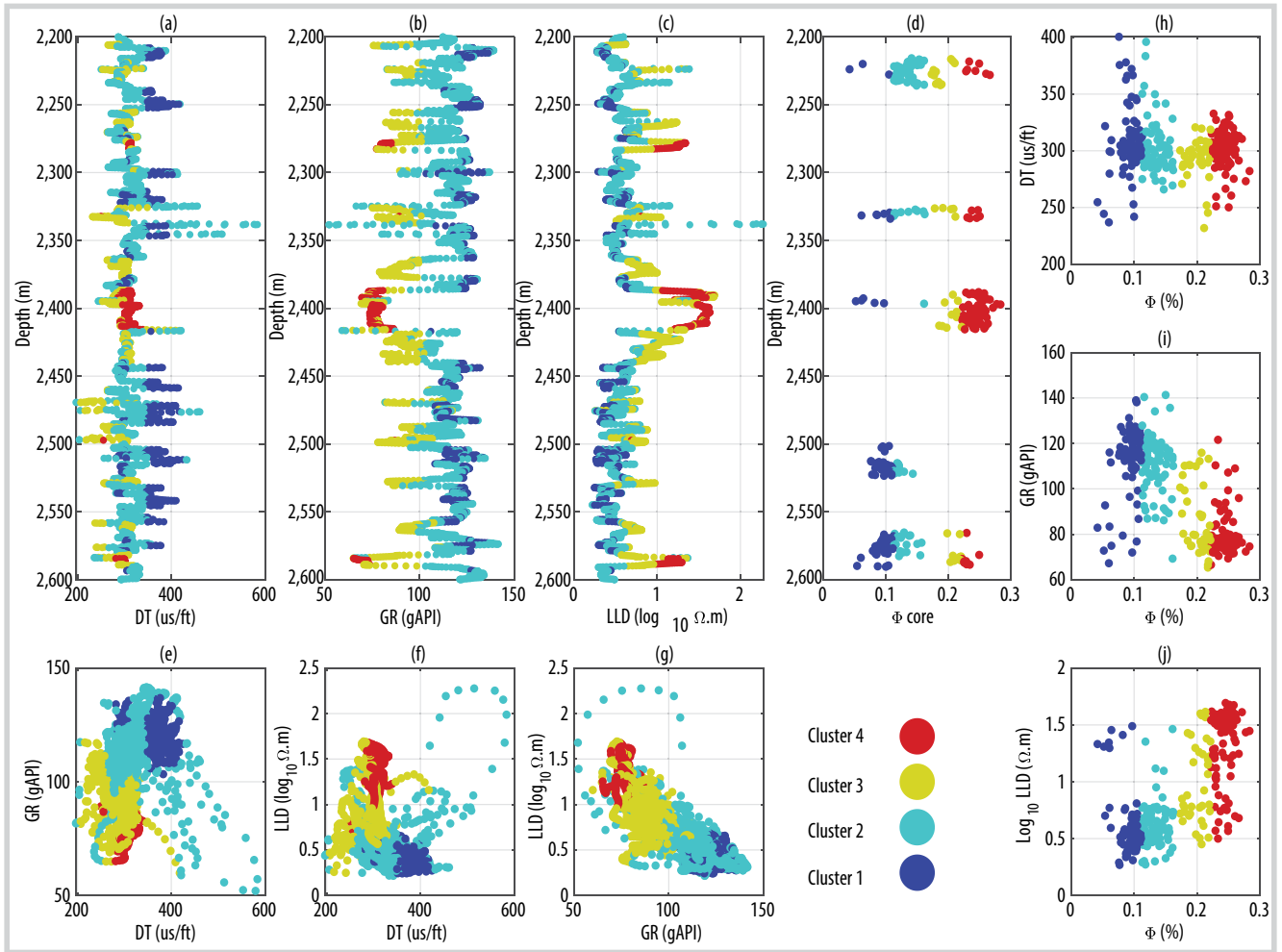


Figure 3. Clustering results. The cluster numbers are defined by data analysis and geological conditions.

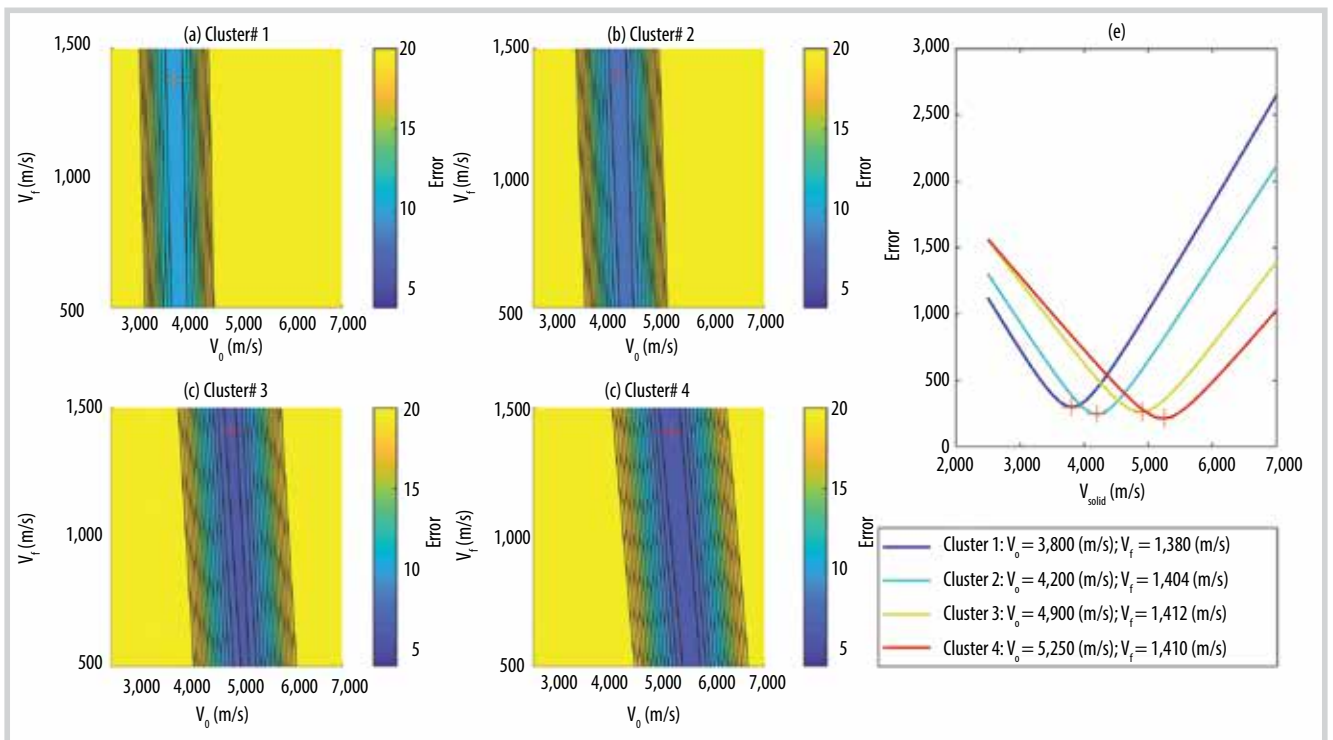


Figure 4. Error between the calculated and measured V_p for each cluster. We choose the optimal pair values of V_0 and V_f for each cluster (marked by red cross).

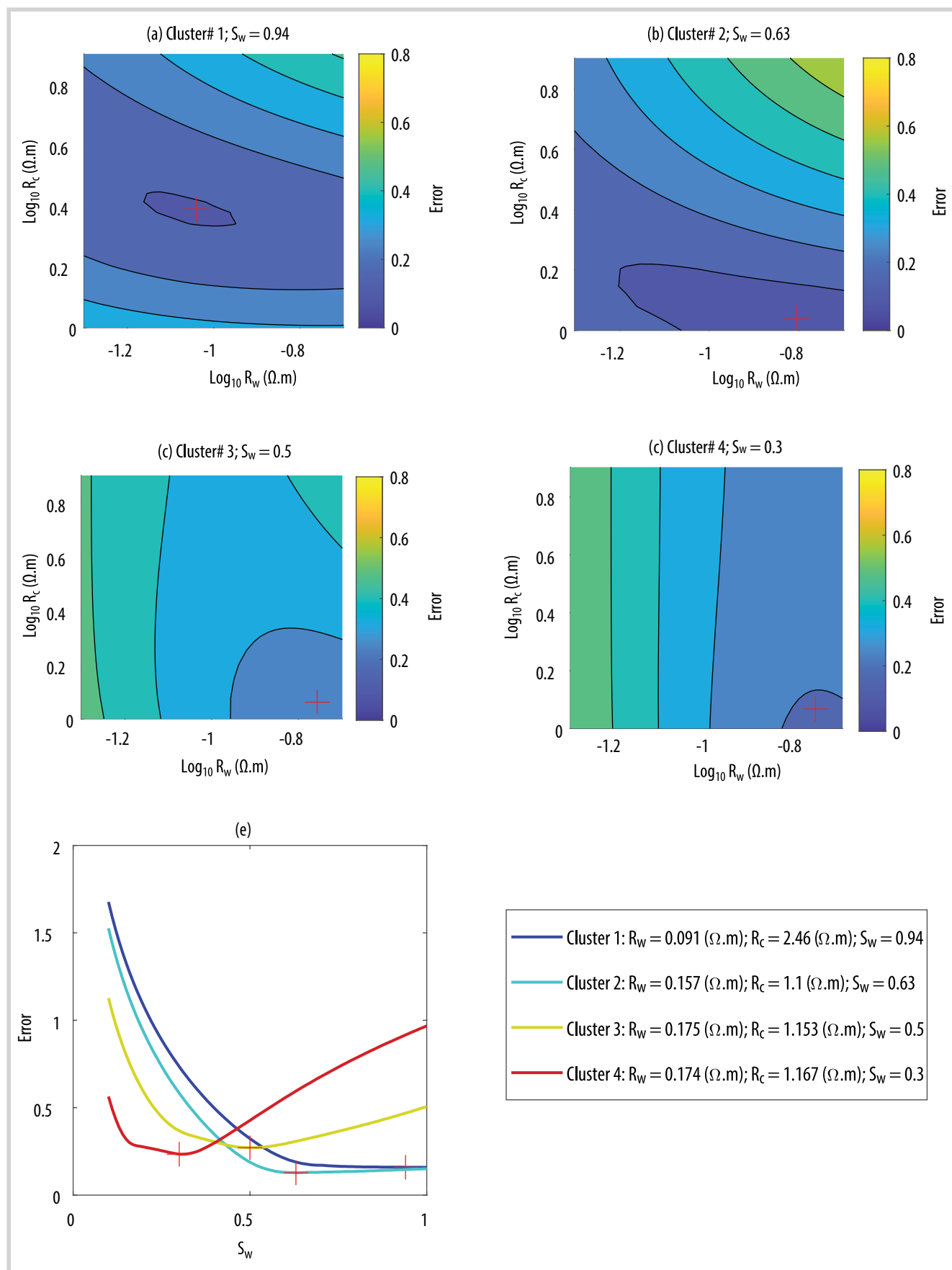


Figure 5. Error between the calculated and measured resistivity for each cluster. We choose the optimal values of R_w , R_c and S_w for each cluster (marked by red cross).

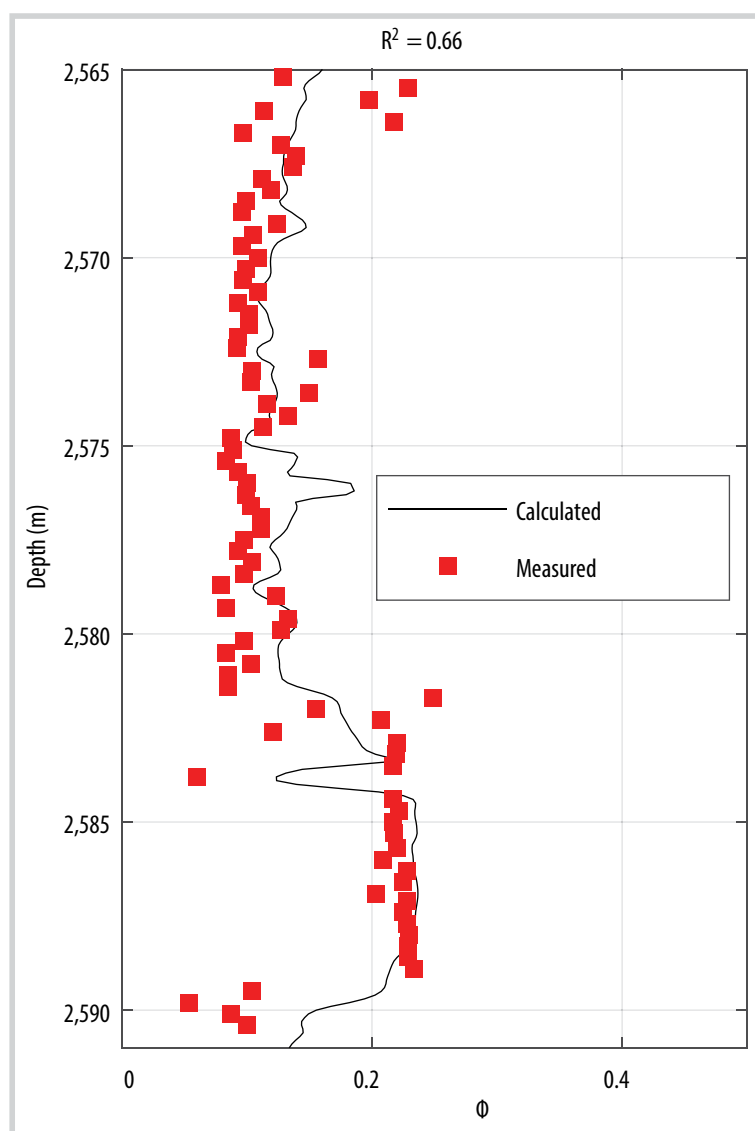


Figure 6. Estimation of porosity of testing data set, S5.

East Vietnam Sea (Figure 1), where numerous wells have been drilled for oil and gas exploration and production purposes.

The well log data tested in this study is taken from the Nam Con Son basin, which is located in the southern Vietnam continental shelf (Figure 1). The basin has an area of about 110,000 km². Hydrocarbons were discovered in the Nam Con Son basin in three different types of reservoirs: pre-Cenozoic weathered and fractured basement, Oligocene - Miocene clastics and Miocene carbonates.

We applied the process to a well log data set containing p-wave velocity, resistivity, gamma ray and core measurement (Figure 2) for a clastic reservoir interval from 2,200 m TVD to 2,600 m TVD of a well in the Nam Con Son basin. The core data are available for five depth ranges: S1 (66 samples), S2 (26 samples), S3 (91 samples), and S4 (41 samples) for data analysis; S5 (83 samples) for the final test.

The well logs and core data were employed in the FCM cluster-

ing process, and the results are presented in Figure 3. The Error (Equation 4) was used to define the optimal parameters in Equations (1) and (2). The error between the calculated p-wave velocity (using Equation 1) and the measured p-wave velocity defines the optimal pair of values V_0 and V_f (Figure 4). The error between the calculated resistivity (using Equation 2) and the measured resistivity (LLD logs) defines the optimal values of R_w , R_c and S_w (Figure 5). The inversion of testing data, S5 is presented in Figure 6, showing a good correlation between the inverted and measured porosity values. Noting that this data set is excluded in any previous FCM analysis process.

4. Conclusions

We present an approach of using fuzzy c-means clustering to classify the well logs and core data in clusters and then running inversion for each cluster. The basic idea of doing this is to set suitable parameters in the constitutive equations, which usually vary with rock units that may relate to clusters. We demonstrate the process by using well logs and core data of one well in the Nam Con Son basin, Vietnam. The prediction shows reasonable results for testing data set, S5. The square correlation coefficient between the predicted and core measurement is 0.66.

Acknowledgements

This research is funded by the Vietnam National Foundation for Science and Technology Development (NAFOSTED) under the grant number 105.99-2019.324.

References

- [1] Paolo Dell'Aversana, Giancarlo Bernasconi, Fabio Marco Miotti, and Diego Rovetta, "Joint inversion of rock properties from sonic, resistivity and density well-log measurements", *Geophysical Prospecting*, Vol. 59, No. 6, pp. 1144 - 1154, 2011. DOI: 10.1111/j.1365-2478.2011.00996.x.
- [2] Wenting Wu and Dario Grana, "Integrated petrophysics and rock physics

modeling for well log interpretation of elastic, electrical, and petrophysical properties", *Journal of Applied Geophysics*, Vol. 146, pp. 54 - 66, 2017. DOI: 10.1016/j.jappgeo.2017.09.007.

[3] Per Avseth, Ivan Lehocki, Øyvind Kjøsnes, and Odd Sandstad, "Data-driven rock physics analysis of North Sea tertiary reservoir sands", *Geophysical Prospecting*, Vol. 69, No. 3, pp. 608 - 621, 2021. DOI: 10.1111/1365-2478.12986.

[4] Ha Quang Man, Doan Huy Hien, Kieu Duy Thong, Bui Viet Dung, Nguyen Minh Hoa, Truong Khac Hoa, Nguyen Van Kieu, and Pham Quy Ngoc, "Hydraulic flow unit classification and prediction using machine learning techniques: A case study from the Nam Con Son basin, offshore Vietnam", *Energies*, Vol. 14, No. 22, 2021. DOI: 10.3390/en14227714.

[5] S. J. Cuddy and Paul Glover, "The application of fuzzy logic and genetic algorithms to reservoir characterization and modeling", in *Soft Computing for Reservoir Characterization and Modeling*. Springer-Verlag Berlin Heidelberg, 2022. DOI: 10.1007/978-3-7908-1807-9_10.

[6] Mohammad-Ali Ahmadi, Mohammad Reza Ahmadi, Seyed Moein Hosseini, and Mohammad Ebadi, "Connectionist model predicts the porosity and permeability of petroleum reservoirs by means of petrophysical logs: application of artificial intelligence", *Journal of Petroleum Science and Engineering*, Vol. 123, pp. 183 - 200, 2014. DOI: 10.1016/j.petrol.2014.08.026.

[7] Janmenjoy Nayak, Bighnaraj Naik, and H. S. Behera. "Fuzzy C-means (FCM) clustering algorithm:

a decade review from 2000 to 2014", *Computational Intelligence in Data Mining*, Vol. 2, pp. 133 - 149, 2014. DOI: 10.1007/978-81-322-2208-8_14.

[8] Kristofer Hellman, Thomas Günther, and Torleif Dahlin, "Application of joint inversion and fuzzy c-means cluster analysis for road pre-investigations", *EAGE Near Surface Geoscience 2012 - 18th European Meeting of Environmental and Engineering Geophysics, Paris, France*, 3 - 5 September 2012. DOI: 10.3997/2214-4609.20143417.

[9] James C. Bezdek, Robert Ehrlich, and William Full, "FCM: The fuzzy C-means clustering algorithm", *Computers & Geosciences*, Vol. 10, No. 2 - 3, pp. 191 - 203. 1984. DOI: 10.1016/0098-3004(84)90020-7.

[10] Kieu Duy Thong and Anton Kepic, "Seismic-impedance inversion with fuzzy clustering constraints: An example from the Carlin Gold district, Nevada, USA", *Geophysical Prospecting*, Vol. 68, No. 1, pp. 103 - 128, 2019. DOI: 10.1111/1365-2478.12891.

[11] Kieu Duy Thong, Anton Kepic, and Cornelia Kitzig, "Classification of geochemical and petrophysical data by using fuzzy clustering", *24th International Geophysical Conference and Exhibition, Perth, Australia, 15 - 18 February 2015*. DOI: 10.1071/ASEG2015ab215.

[12] Pham Huy Giao, Pham Hong Trang, Doan Huy Hien, Pham Quy Ngoc, "Construction and application of an adapted rock physics template (ARPT) for characterizing a deep and strongly cemented gas sand in the Nam Con Son basin, Vietnam", *Journal of Natural Gas Science and Engineering*, Vol. 94, 2021. DOI: 10.1016/j.jngse.2021.104117.

IMPACT OF DEPOSITION AND DIAGENESIS ON QUALITY OF SANDSTONE RESERVOIRS: A CASE STUDY IN CUU LONG BASIN, OFFSHORE VIETNAM

Nguyen Trung Son

Vietnam Petroleum Institute

Email: sonnt@vpi.pvn.vn

<https://doi.org/10.47800/PVJ.2022.06-02>

Summary

Sandstone reservoirs are major reservoirs in siliciclastic rocks worldwide. A good understanding of the development of internal rock properties is, therefore, extremely important, especially in terms of porosity and permeability (which indicate reservoir storage and flow capacity), which are controlled by mineral compositions, rock textures, and diagenetic processes. This paper studied formations E and F in three wells in the Cuu Long basin to better define the impacts of not only depositional characters but also diagenetic overprints on porosity and permeability (poroperm). Core samples were analysed via thin section observations, scanning electron microscopy (SEM), X-ray diffraction (XRD) observations, capillary pressure (P_c) and helium porosity - permeability measurements together with petrophysical evaluation.

Formation E was deposited in a fluvial - lacustrine environment that is characterised by claystone/shale interbedded with sandstone, with reduced depositional permeability in finer-grained intervals. XRD and SEM analyses indicate rock quality in the sandstone reservoirs was influenced by a variety of authigenic minerals, such as carbonate cements, quartz overgrowths, zeolites, and laumontite clays, which all tend to reduce poroperm. Whereas, formation F was deposited in a higher energy setting. This was mostly a braided channel environment indicated by a blocky shape in the wireline across the sandy interval and typically good primary porosity and permeability. In formation F, the reservoir quality is strongly controlled by diagenetic evolution. Pore throats in the E and F sandstones are reduced in size by intense compaction and a combination of pore-filling minerals including calcite cements, authigenic clays, and quartz overgrowths, leading to a negative relationship with poroperm. However, this negative relationship is not as clear in the formation E.

Key words: Formations E and F, depositional environment, diagenetic process, petrography, porosity and permeability.

1. Introduction

This study discusses deposition, diagenesis and quality of sandstone reservoirs using a case study in the Cuu Long basin, offshore Vietnam (Figure 1). By creating a better understanding of the controls in the development of poroperm and the diagenetic evolution of formations E and F, the study aims to establish key factors that influence reservoir quality. The work is based on the integration of rock properties with petrographic analysis (thin section petrography, XRD, SEM analyses, capillary pressure (P_c), and petrophysical evaluation. Results will help to

better constrain the depositional environment and diagenetic processes in the study area.

2. Geological setting

The Cuu Long basin is a rift basin that experienced two main deformational events: (i) trans-tensional rifting from the Eocene to Middle - Early Oligocene (40 - 31 Ma), followed by (ii) a transpression from the Middle - Early Oligocene to the Middle - Late Oligocene (31 - 25 Ma). This created three major tectonic styles, namely: (i) rifting-related normal faulting from the Early Eocene to Middle - Early Oligocene, (ii) compression-related reverse faults and folds generated from the Middle - Early Oligocene to Middle - Late Oligocene, and (iii) thermal sagging from the Middle - Late Oligocene to the present, when the ba-



Date of receipt: 25/2/2022. Date of review and editing: 25/2 - 28/4/2022.

Date of approval: 27/6/2022.

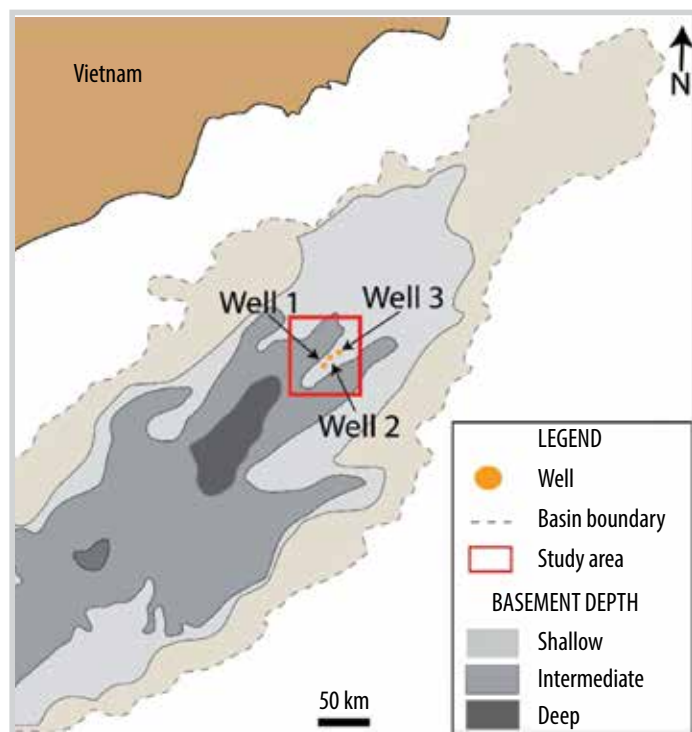


Figure 1. Overview of the study area (modified from Morley et al. [1]).

Period	Formation	Lithology	Seismic sequence	Description	Depositional environment	Tectonic regime	
Pliocene-Quaternary	Bien Dong	[Lithology: Coarse grained sand, shale, interbedded with carbonate and coal layers]	A	Coarse grained, unconsolidated sand, shale, interbedded with carbonate and coal layers	Marine	Thermal Sag	
	Miocene	Dong Nai	[Lithology: Coarse to fine grained sand, coal, minor carbonate layers]	B3	Coarse to fine grained sand, coal, minor carbonate layers		Coastal plain, shallow marine
Con Son		[Lithology: Sand, shale, coal, minor carbonate layers]	B2	Sand, shale, coal, minor carbonate layers	Fluvial, marginal marine		
Bach Ho		[Lithology: Shale dominant with interbedded sand]	B1.2	Shale dominant with interbedded sand	Swamp, alluvial-lacustrine		
Oligocene	Tran Tan	[Lithology: Interbedded sand, silt, and shale; basalt and tuff basalt in places]	B1.1	Interbedded sand, silt, and shale; basalt and tuff basalt in places	Swamp-lacustrine		Compression
	Tran Tan	[Lithology: Dominantly shale; andesite and andesite-basalt in places]	C, D	Dominantly shale; andesite and andesite-basalt in places	Swamp-lacustrine		
Eocene	Tran Cu	[Lithology: Shale, silt and sand, with thin coal and marl layers]	E	Shale, silt and sand, with thin coal and marl layers	Alluvial to swamp-lacustrine	Rifting	
	Ca Coi	[Lithology: Conglomerate and sandstone with thin shale layers]	F	Conglomerate and sandstone with thin shale layers	Proluvial-alluvial		
Pre-Tertiary		[Lithology: Weathered and fractured granitoids and metamorphic rocks]		Weathered and fractured granitoids and metamorphic rocks			

Figure 2. The stratigraphic column of the study area, focusing on formations E and F marked by a blue rectangle (modified from Morley et al [1] and W.J. Schmitt [4]).

sin is fully filled by sediment without major faulting [1] which were affected by two main fault systems, NE-SW and NW-SE, of the Cuu Long basin [2]. Accommodation space in the Cuu Long basin is completely filled with Tertiary sediments, of which the Eocene F sequence is the oldest in the basin, followed by the Eocene - Oligocene E sequence, which includes sequences E, C and D. The Eocene succession is characterised by the Tra Cu and Ca Coi formations, which embrace sequences E and F [3]. Sandstones E and F, which are the focus of this study, were deposited in the Early - Middle Eocene (F) and the Late Eocene to Early Oligocene (E) (Figure 2).

3. Methodology

For the first time, the results of several sets of analysis across the three wells are integrated and combined in a multi-well synthesis. The aim is to better define controls on porosity and permeability in terms of not only depositional characters but also diagenetic overprints. Diagenetic intensity is estimated vertically and horizontally (among the wells) based on integration of reservoir properties. Core photos, core analyses and the results of the petrographic study are integrated with helium-based porosity-permeability measured by routine core analysis (RCA) and capillary pressure. Thin sections, SEM log shape and core data from all wells are proved useful in defining various depositional environments in the study area. Depositional environments are cross-plotted against each other to better identify lithological variability and its tie to poroperm quality.

4. Results

4.1. Core interpretation

Lacustrine shoreface/deltaic sandflat: Fine-grained sandstone is typical of this facies grouping. The primary structure is low-angle bedding and indeterminate lamination (Figure 3).

Channel/channel abandonment: These fining-upward sandy reservoir-quality units include mud rip-up clasts and some coarse grains at their bases that then pass up into cross-bedded units with muddy tops (Figure 4).

Overbank: These are very fine-grained sediments formed from mudstones and very fine siltstones that

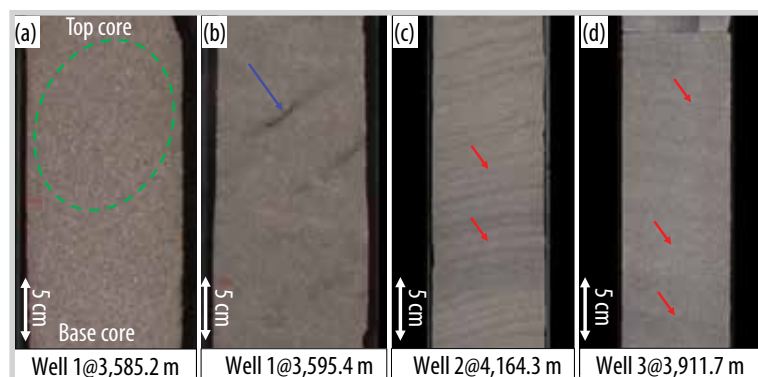


Figure 3. (a) Massive medium sandstone with a mottled texture (green oval) indicating extensive bioturbation, (b) Fine sandstone including plant fragments (blue arrow), (c) Low-angle lamination (red arrow) with fine-grained sand interlaminated with thin shales, and (d) Indeterminate lamination (red arrow) with fine grain size.

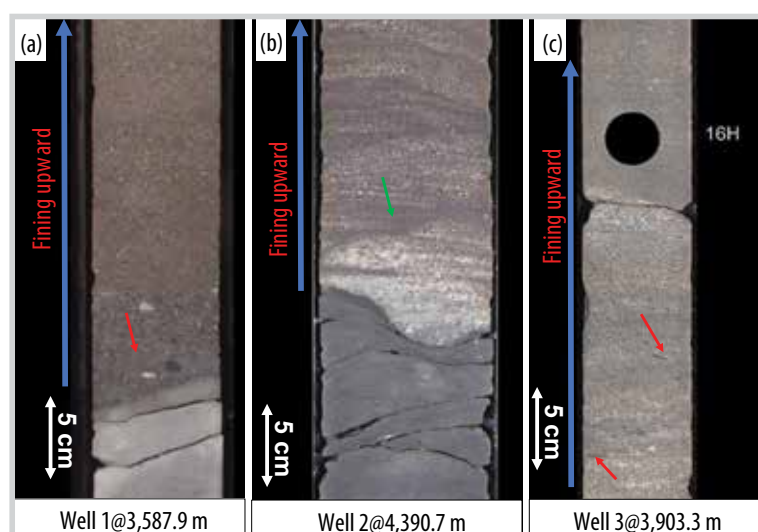


Figure 4. (a) Fining-upward sandstones include very coarse grains and granules; mudstone clasts occur within some beds (red arrow), (b) Primary sedimentary structures are dominated by planar cross-bedding (green arrow) with fining-upward trends and erosional bases, exaggerated by compactional loading, (c) The fining-upward trend with the only fossil material is observed within these facies being small plant fragments (red arrow).

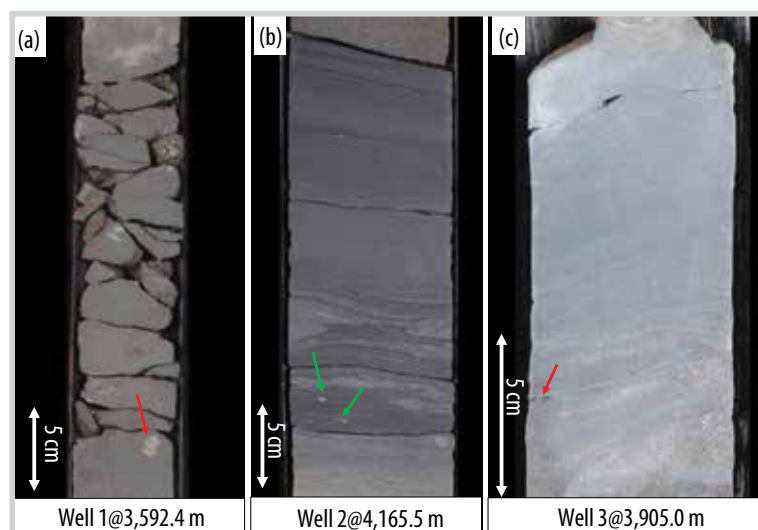


Figure 5. (a) Mudstones and very fine siltstones include occasional nodular pyrite (arrow) and sand-filled burrows (at the top) in well 1, (b) Mudstones and some nodular pyrite (arrow) in well 2, (c) Very fine siltstone includes a calcite-cement mud clast (arrow).

include some sandstone-filled burrows. There are some pyrite nodules and calcite-cemented mud clasts in several intervals (Figure 5).

Braided fluvial: These sandstones range in grain size from very fine (lower) to coarse (middle). The thickness of individual beds varies from about 10 cm to 1.65 m. The sandstones are usually composed of mud rip-up clasts, very coarse grains, granules and pebbles which are most common within bed bases (Figure 6).

Depositional environment interpretation: In general, the textural features and framework-grain compositions (lithic-arkoses and arkoses, Figure 9) of the E sandstone indicate that the sediments were transported over a distance not too far from the source, and that during deposition the sands were frequently affected by periods of at least moderate current activity (sand deposition) alternating with periods of quiescence (clay deposition). In combination with the palynology, it suggests that the sediments were deposited in a mostly lacustrine and fluvial environment [5].

Textural features and framework-grain compositions of the F sandstone indicate that the sediments were transported not too far from the source and that this sandstone was frequently subjected by high energy flows in a braided fluvial setting.

4.2. Petrophysical analysis

Helium analytical results on core plugs from formations E and F show a wide range of porosity and permeability. In formation E, porosity varies from 2 to 16% ($\Phi_{avg.} = 9.7\%$) and permeability from 0.001 to 1,000 mD ($K_{avg.} = 30.8$ mD). The F formation generally shows higher values than the E formation, with porosity ranging from 2 to 18% ($\Phi_{avg.} = 10.6\%$) and permeability from 0.0001 to more than 1,000 mD ($K_{avg.} = 66.7$ mD). Cross-plots of porosity and permeability show a good correlation in both formations, with linear relationships.

The curvature of capillary pressure curves indicates the rock quality. The examples of formations E and F show more gentle curvatures related to reduced permeability due to the

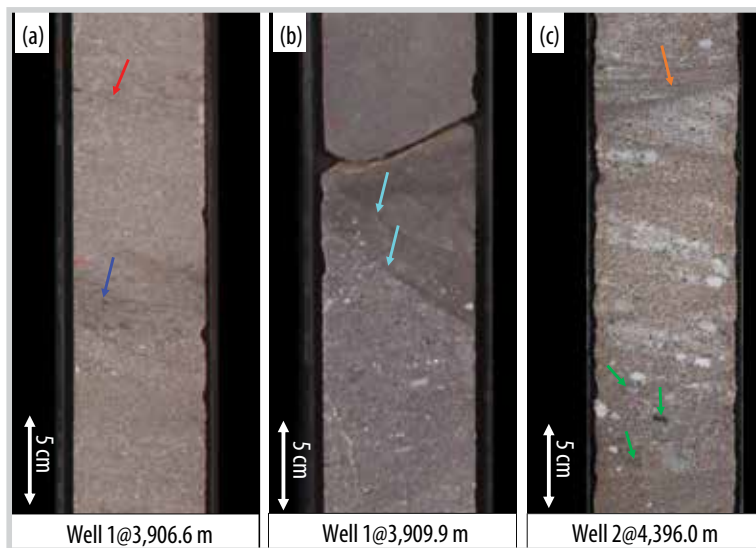


Figure 6. (a) The sandstones commonly include mud clasts, very coarse grains, granules and pebbles (blue arrow). Fossil material includes some small plant fragments (red arrow) (b) A sequence of low-angle normal fractures at the contact between coarse and very fine sandstones. Fractures are clay smeared (aqua arrow) (c) The dominant primary sedimentary structure is planar cross-bedding which ranges in dip from horizontal to 45° (orange arrow). Some of the pebbles comprise green basement clasts, which are possibly basalt (green arrow).

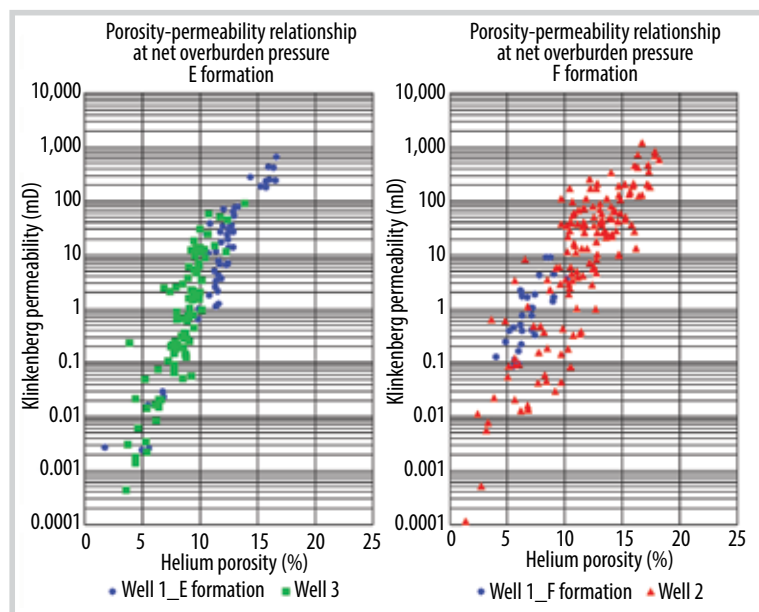


Figure 7. Cross-plots illustrating the relationship between porosity and permeability in formations E and F.

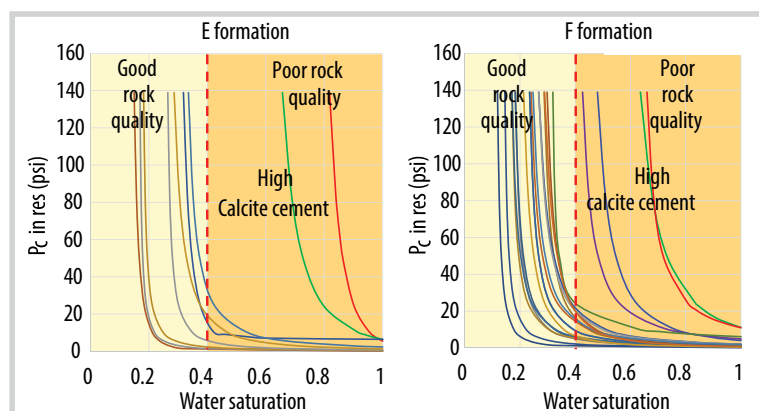


Figure 8. The curvature of the capillary pressure curve indicates the rock quality.

impact of calcite cements in the sands. Poorer quality samples show high residual water saturation related to poorer sorting, and finer grain sizes or poorer quality outputs can be related to calcite cements that have a negative impact on poroperm characteristics. The analysis implies that there are relatively high porosity and permeability intervals within the overall lower porosity-permeability of the dominant reservoirs.

4.3. Petrographic analysis

4.3.1. Sandstone detrital composition

Petrographic study shows the cored intervals in well 1, well 2 and well 3. The R.L. Folk classification [6] is used to classify sandstones with less than 15% detrital matrix. The Q, F, and R components are: Q = all quartz, except chert; F = feldspar + granitic fragments; and R is all other rock fragments. Most of the samples are arkosic sandstones and lithic arkose sandstones (Figure 9).

4.3.2. Visible porosity

Porosity in the E and F sandstones includes primary intergranular porosity (i.e. the space between grains) and secondary porosity which is mainly related to the dissolution of unstable detrital grains, such as volcanic fragments and feldspars (K-feldspar and plagioclase). The mechanical compaction of this cored interval is moderate, characterised by grain contacts that are mostly point-to-point (blue arrow); some long-axis (green arrow) passing to occasional concavo-convex contacts (yellow arrow).

4.3.3. Mineral framework grains

Whole-rock analysis of samples in the cored intervals shows quartz dominance. Feldspars are the second most abundant component in the sandstones and consist of two types, potassium feldspar (K-F) and plagioclase. Petrography shows that feldspar dissolution has generated secondary porosity, thus enhancing the total porosity.

Well 1_E sandstone is mainly composed of quartz (average 40%), K-feldspar and plagioclase.

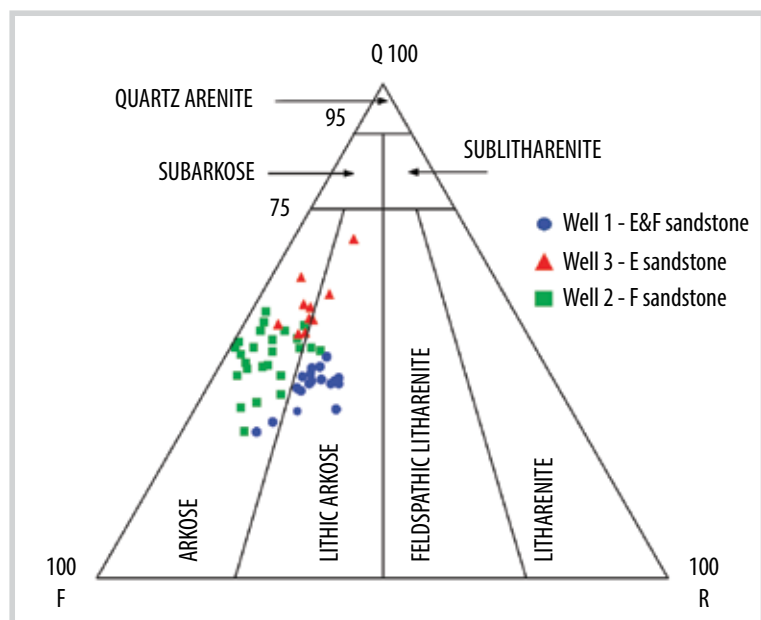


Figure 9. The detrital composition of samples with less than 15% detritals using R.L. Folk's classification [6].

gioclase (average 40%), clay minerals such as mica, laumontite, kaolinite (average 18%); carbonate minerals, calcite, dolomite, and siderite are scarcely present (average 2%) (Figure 11b). In comparison, XRD analysis of samples from well 3 (Figure 11d) has quartz averaging 29% and 38% in their K-F and plagioclase, respectively. This is lower than in well 1, perhaps because the sedimentary source is different. The clay mineral contents in well 3 are higher than in well 1, perhaps because well 3 was further from the sediment source than well 1, or it was deposited under lower overall energy conditions. Carbonate cement content in well 3 (3%) is slightly higher than in well 1 (2%).

Samples of well 1 in the F sandstone mainly consist of quartz (average 54%), K-feldspar and

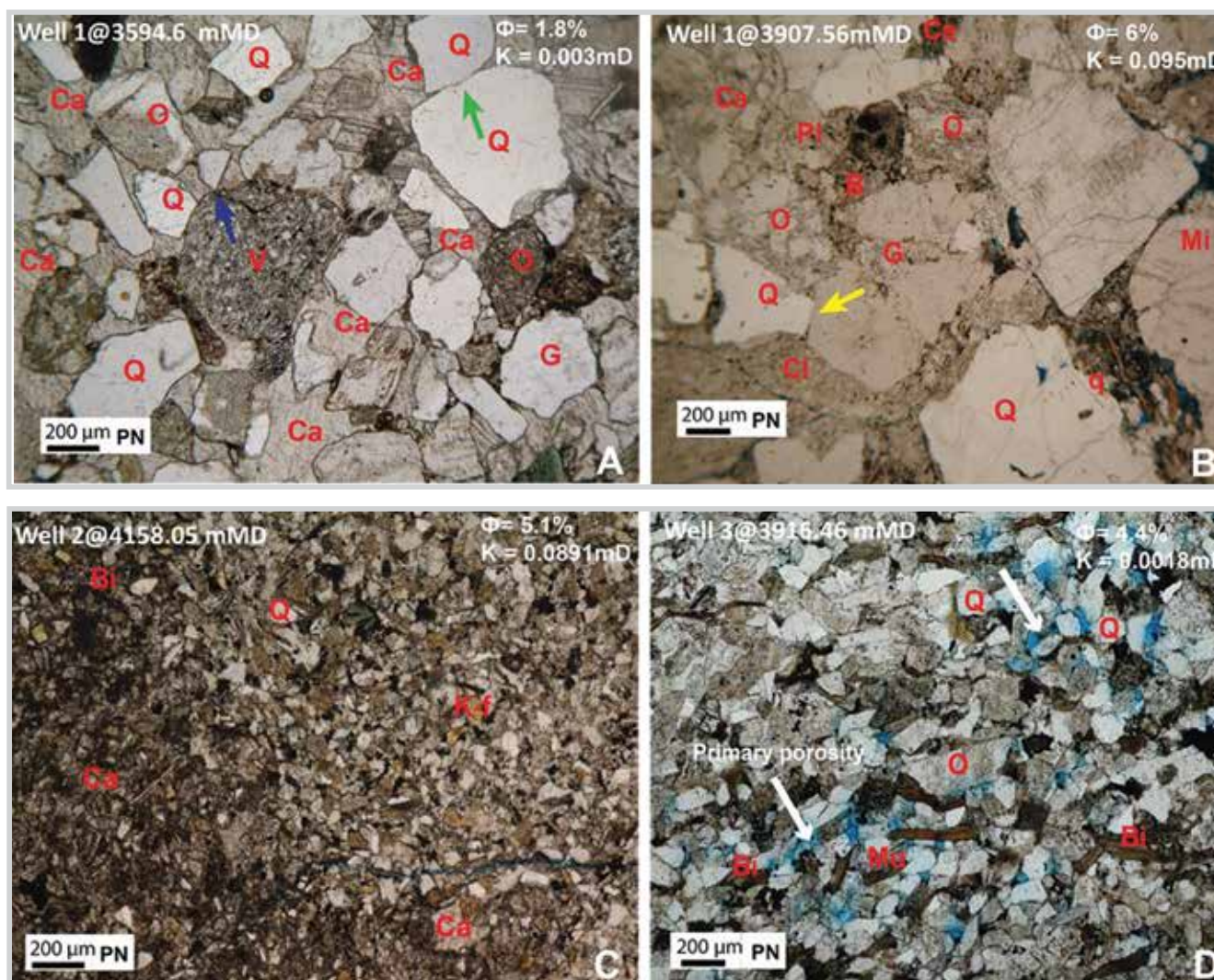


Figure 10. Thin section images of sandstones (pore space is shown in blue; calcite cements (Ca) fill or partly fill intergranular pore spaces. (Q = quartz, q = quartz overgrowths, O = orthoclase, Pl = plagioclase, G = granitic, Bi = volcanic fragments biotite, and Mu = muscovite).

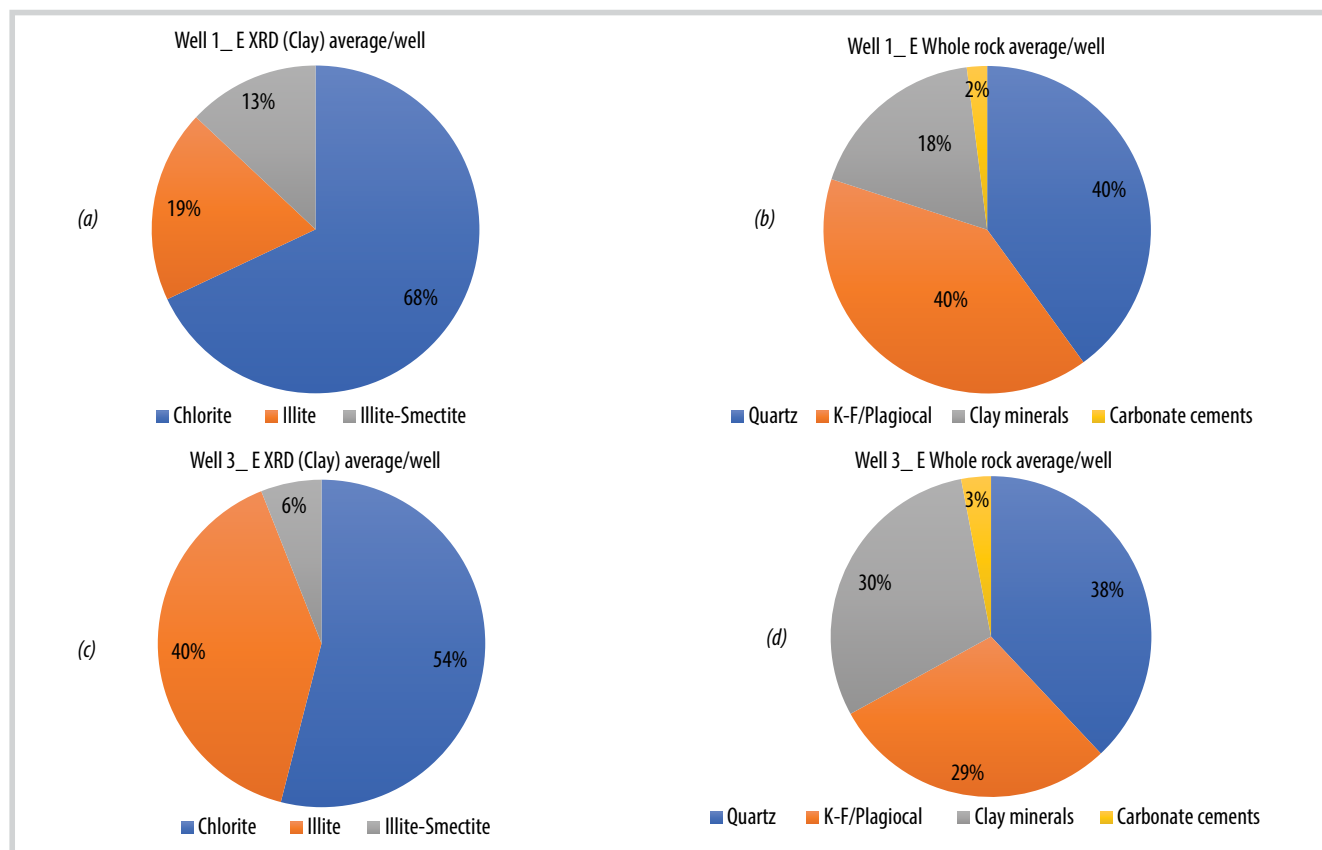


Figure 11. Illustrating the whole rock and XRD results in the E sandstone.

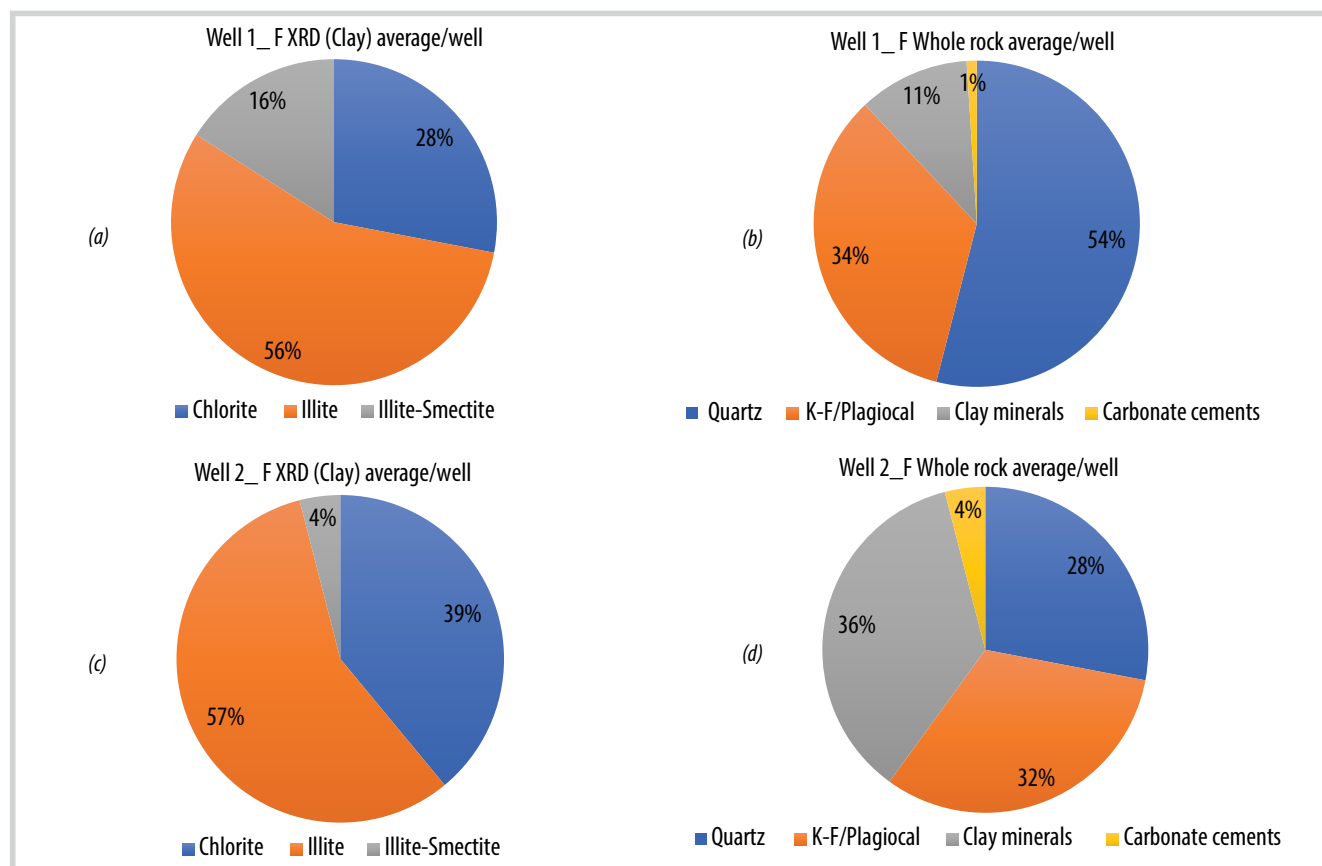


Figure 12. Illustrating the whole rock and XRD results in the F sandstone.

plagioclase (average 34%), other clays such as mica, laumontite, kaolinite (average 18%) and the carbonate minerals, calcite, dolomite and siderite (average 1%) (Figure 12a). In comparison, the F sandstone in well 2 has a quartz average of about 28% and 36% of K-feldspar/plagioclase

(Figure 12d). This is lower than in well 1 and reflected in the petrographic typing of well 1, which is mostly lithic arkose with less feldspar than the arkoses that dominate in well 2 (Figure 9).

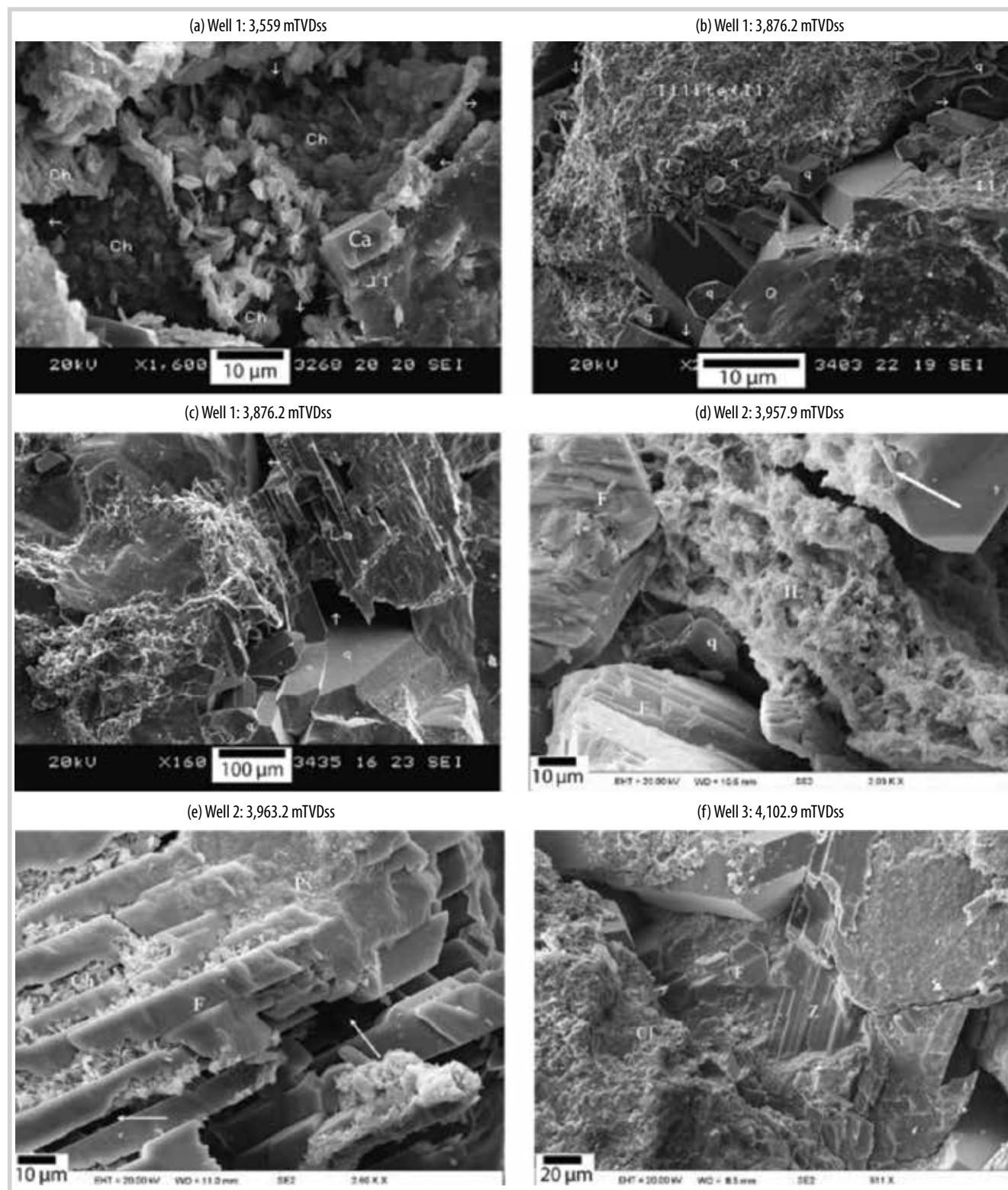
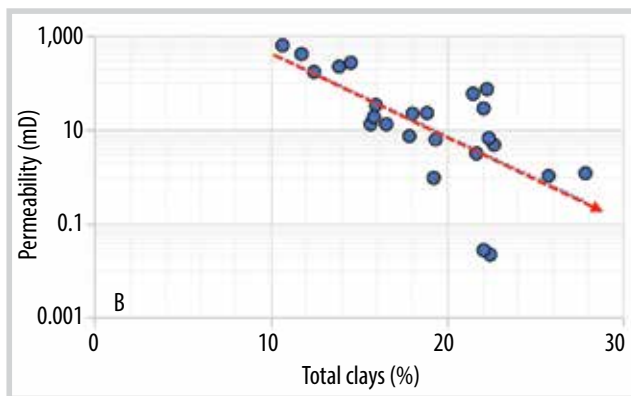
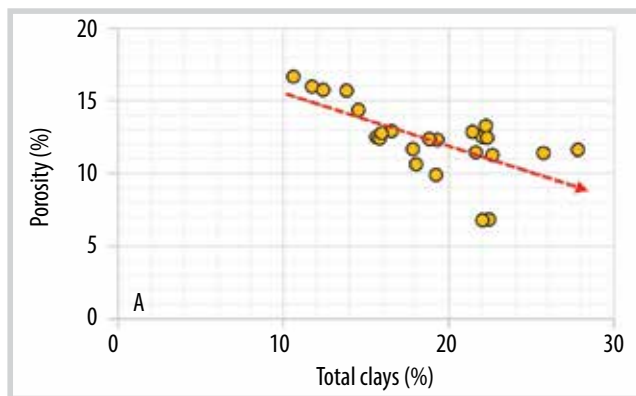


Figure 13. SEM images of samples from all wells in the study area.

Well 1_E formation



Well 3_E formation

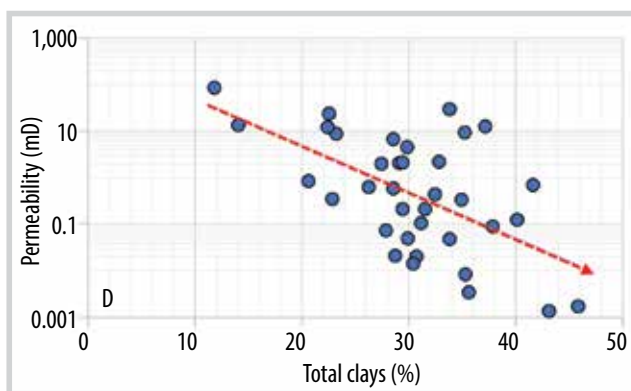
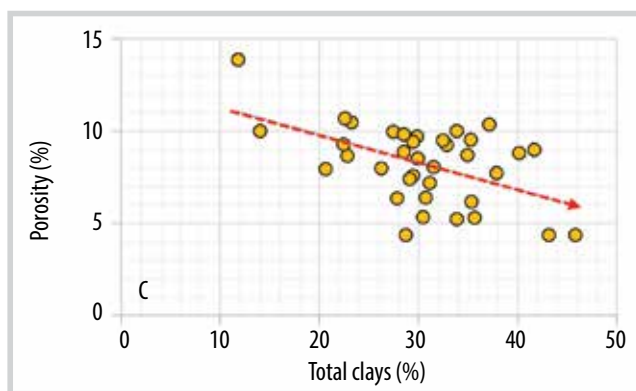
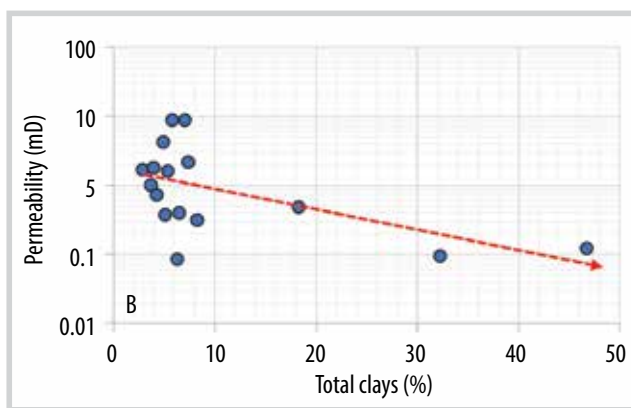
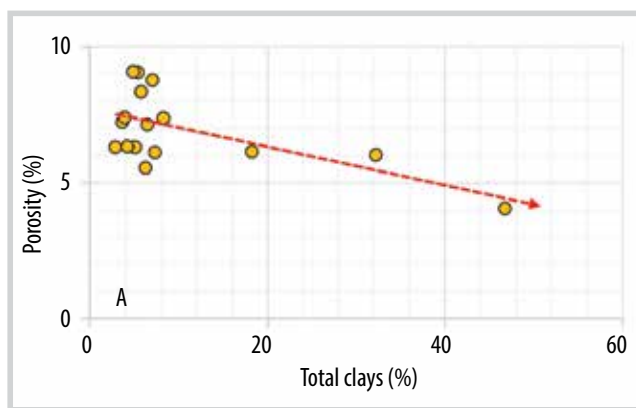


Figure 14. The relationship between permeability and total clays shows a negative trend in formation E.

Well 1_F formation



Well 2_F formation

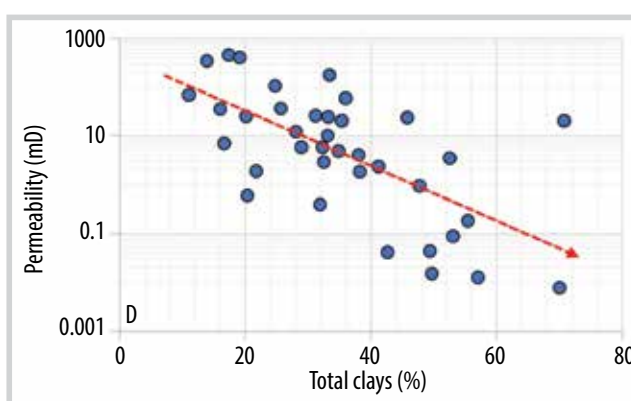
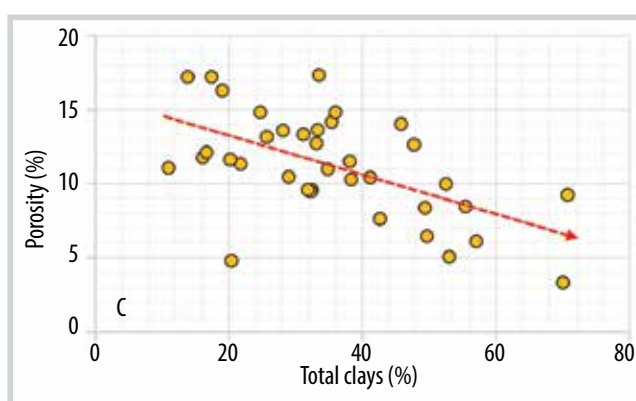


Figure 15. The relationship between permeability and total clay shows a negative trend in formation F.

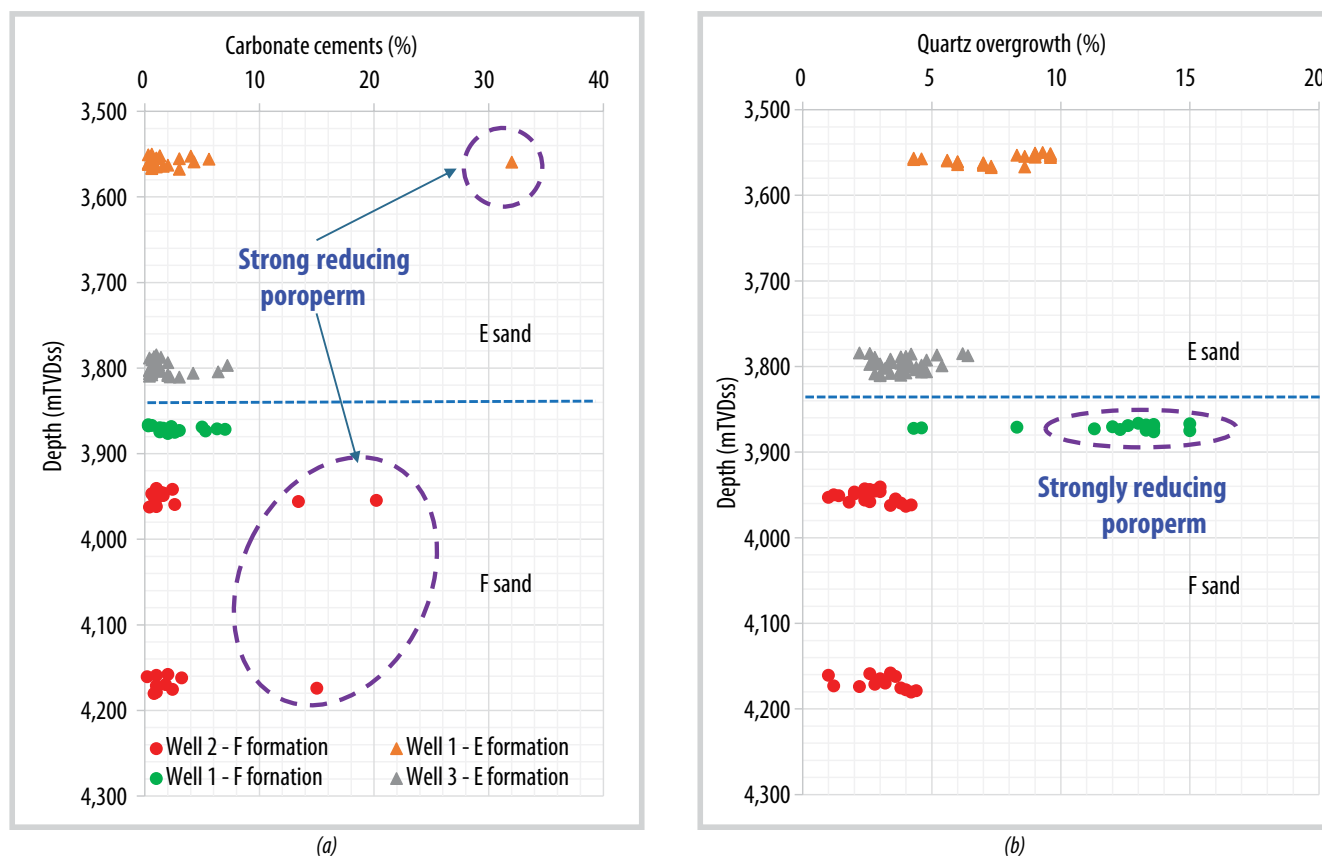


Figure 16. The proportion of carbonate cements and quartz overgrowth distribution.

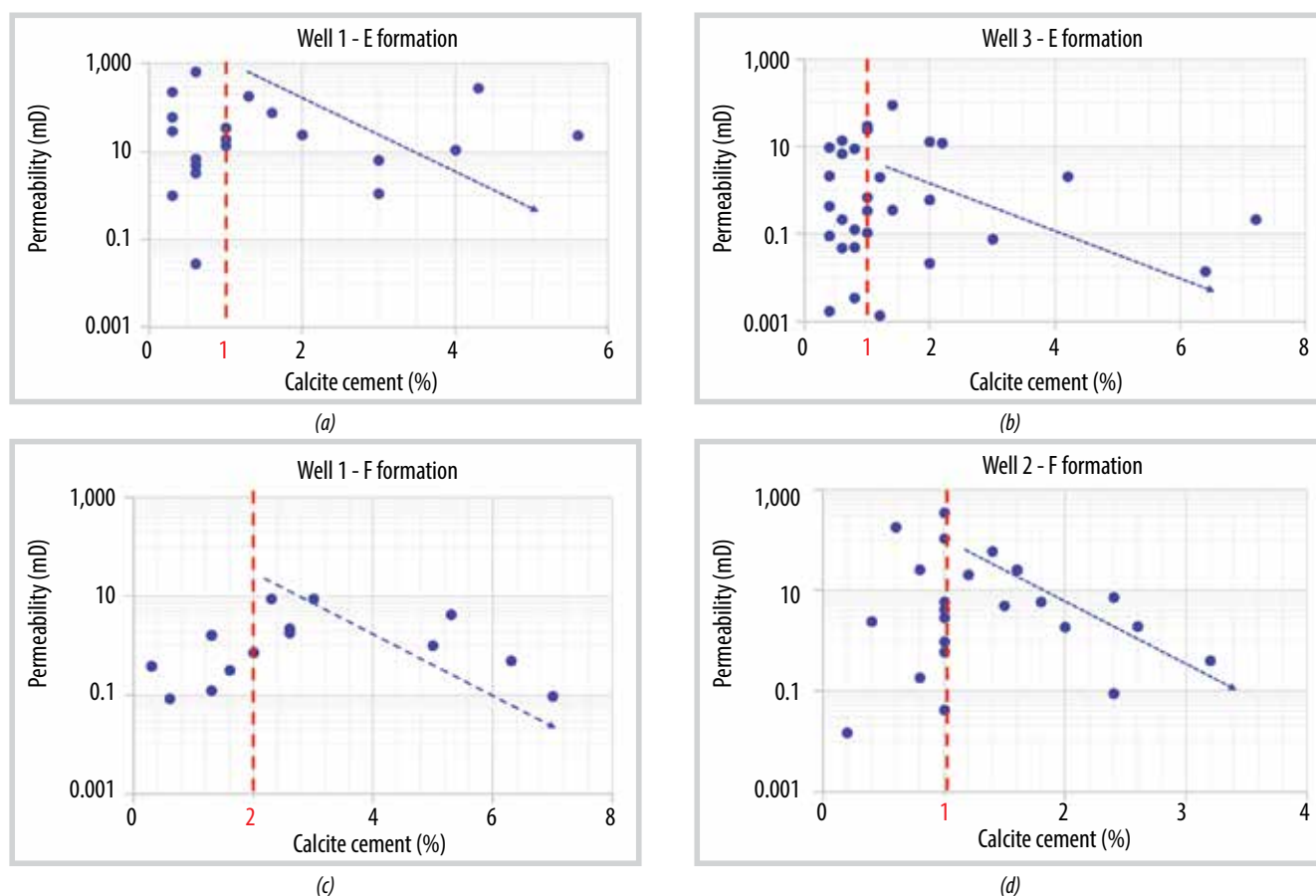


Figure 17. The relationship between permeability and calcite cements shows a negative trend.

4.3.4. Authigenic clays

The presence of clays in a sandstone across all wells tends to degrade reservoir quality.

Figure 13a illustrates authigenic chlorite aggregates (Ch) occurring mostly as subhedral, thin plates that can fill pore spaces, together with illite (Il) and calcite. The macro/micropore sizes of $< 20 \mu\text{m}$ encompass the remaining volumes of an occluded primary pore. A pore throat that is completely blocked by many large crystals of mosaic quartz overgrowth (q) leads to the initial pore throat not only reduced in volume but also divided into very small pore channels (arrow) and becomes very tortuous (Figure 13b).

Figure 13c suggests the remaining intergranular pores (arrows) have now become isolated or retain very poor connectivity. In addition, authigenic illite aggregates (Il) fill in the intergranular pores and pore throats, illustrating how a small amount of authigenic illite can degrade the permeability.

Authigenic chlorite clay minerals occur as thin mats of crystals that coat detrital grains. Wispy and webby illite intermixed with platy chlorite can completely coat detrital grains and fill intergranular pores, resulting in a strongly reduced permeability (Figure 13d).

Detrital feldspar grains (F) can be dissolved, forming secondary pores. The orientation of the feldspar remnants suggests that dissolution is crystallographically controlled. Locally, feldspar remnants are partly albitised and have been replaced with chlorite. This suggests that the dissolution of unstable detrital grains likely pre-dated chloritisation in the paradiagenetic sequence (Figure 13e).

Figure 13f shows a blocky authigenic zeolite crystal (Z) that occupies intergranular pore space, thus damaging the reservoir quality. A feldspar grain (F) has also been dissolved and albitised. Locally, authigenic clay minerals (Cl) occur as chlorite and illite/illite-smectite that fill in the secondary pores and can partly coat detrital grains. The strong development of quartz overgrowths (upper left) has also occluded pore throats.

Laumontite (a zeolite mineral) can replace feldspar as double-edge crystal grains or cleavage crack fills. Some pore-filling laumontites, as well as quartz overgrowths, can slow or inhibit further compaction (Figure 13c).

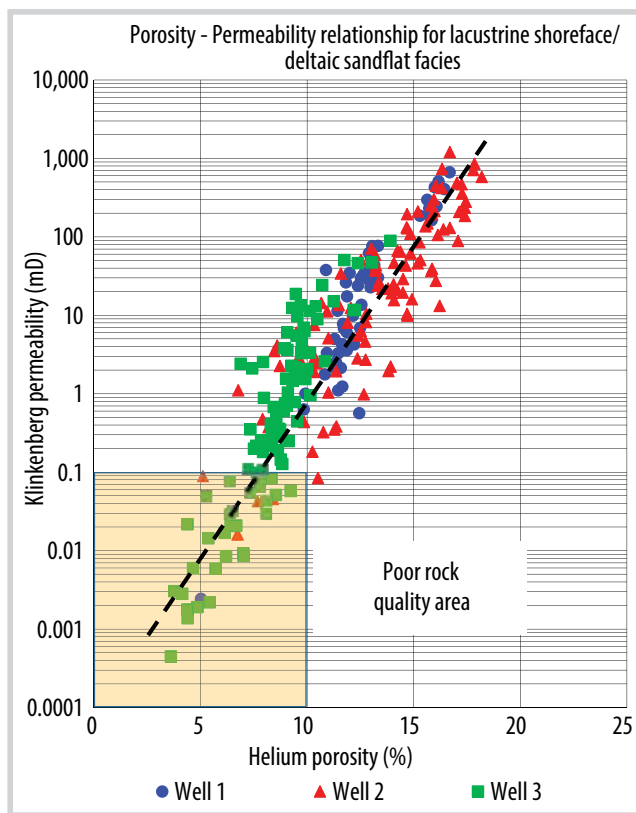
A negative relationship between total clay minerals and poroperm suggests the clay minerals are strongly de-

grading the porosity and permeability (Figures 14 and 15). Pore-lining chlorite is directly precipitated on the surfaces of grains, extending into pore space, leading to a significant decrease in permeability (Figure 13a). Illite occurs as pore-linings and is partly pore filling and partly grain coating. It forms irregular flakes with lath-like projections that can bridge intergranular spaces, thus decreasing permeability and pore throat diameters (Figures 13b and 13d). Smectite/illite transforms into illite at higher temperatures and rarely occurs in the temperature ranges of most petroleum fields unless the reservoir is flushed by hydrothermal waters.

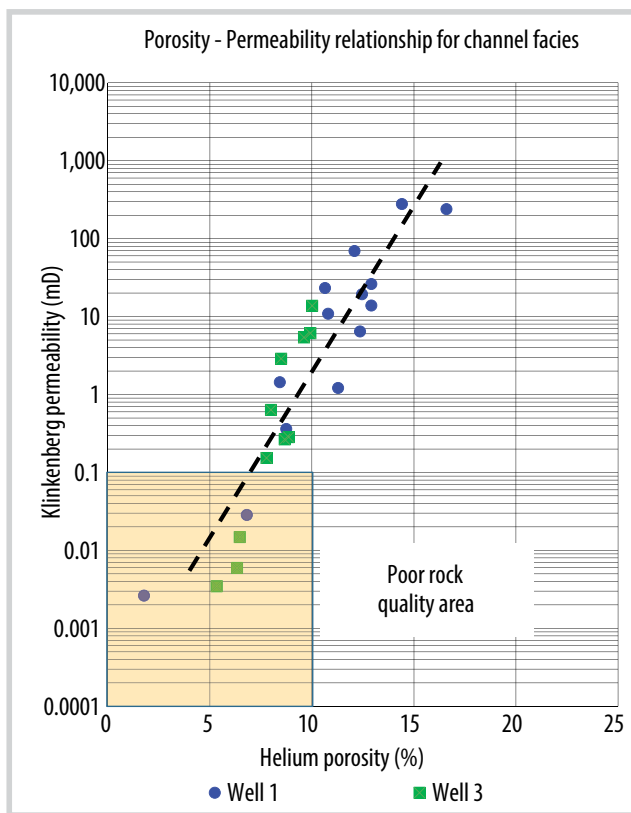
4.3.5. Quartz, carbonate cements

Carbonate cements in the study area are composed of calcite with minor dolomite and siderite. Carbonate cements are observed in all wells and it is a significant factor influencing the poroperm quality of the studied sandstones. Figure 16a shows the abundance of carbonate cements is less than a certain threshold (about 10%) and illustrates the different amounts between the wells. The proportion of carbonate cements increases up to 32% in the formation E of well 1 (well_E) and 20% in well 2 (Figure 16a) with an average of 3% of rock volume in both wells. Carbonate cements in well 3 and well 1_F are less, with an average of 1.3% and 2.6%, respectively. Figure 17 is a cross-plot with a carbonate cement value threshold of 1% or 2%; values less than this show an unclear relationship between carbonate cement and poroperm. However, when the proportion of calcite cements is higher than 1% (well 1_E, well 2, and well 3) or 2% (well 1_F), there is a decrease in porosity and permeability with increasing carbonate cement content (Figure 17).

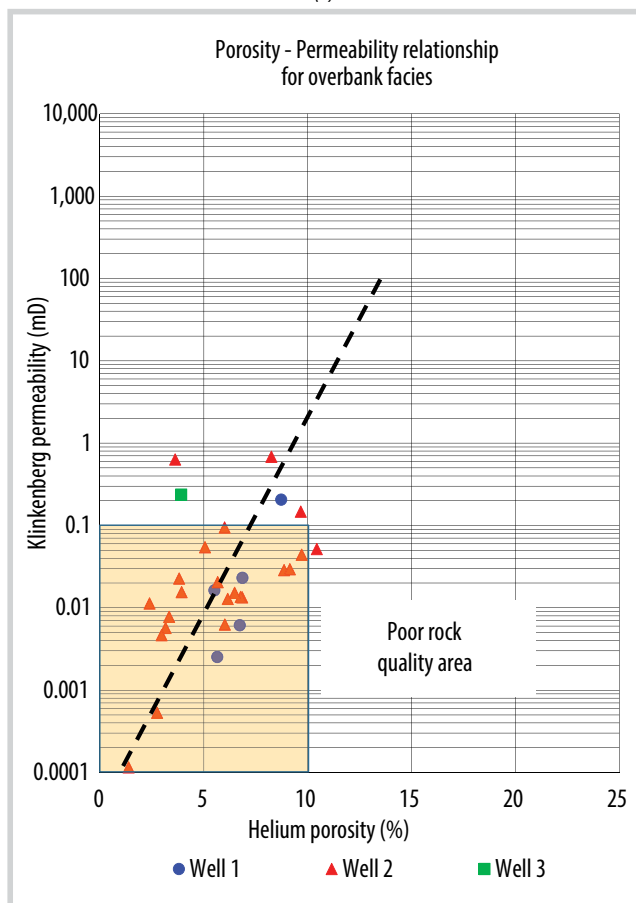
Quartz overgrowth cements, which are more abundant than carbonate cements, range from 4 % to 10%, average 7.4% in formation E of well 1, and mostly 3 - 6% (average 3.9%) in well 3, and 2.7% in well 2, which also contains the highest levels of overgrowths from 4 - 15% (average 11.8%). The formation of quartz (overgrowth) cement is an ongoing diagenetic process. It begins as one of the earlier burial phases when it can be covered by chlorite rims and can proceed until it fully fills primary pores (Figure 16b). Later quartz overgrowth cement generations develop over authigenic illite and are present as pyramidal quartz and euhedral quartz crystals that partly fill primary porosity (Figures 13b, c, d).



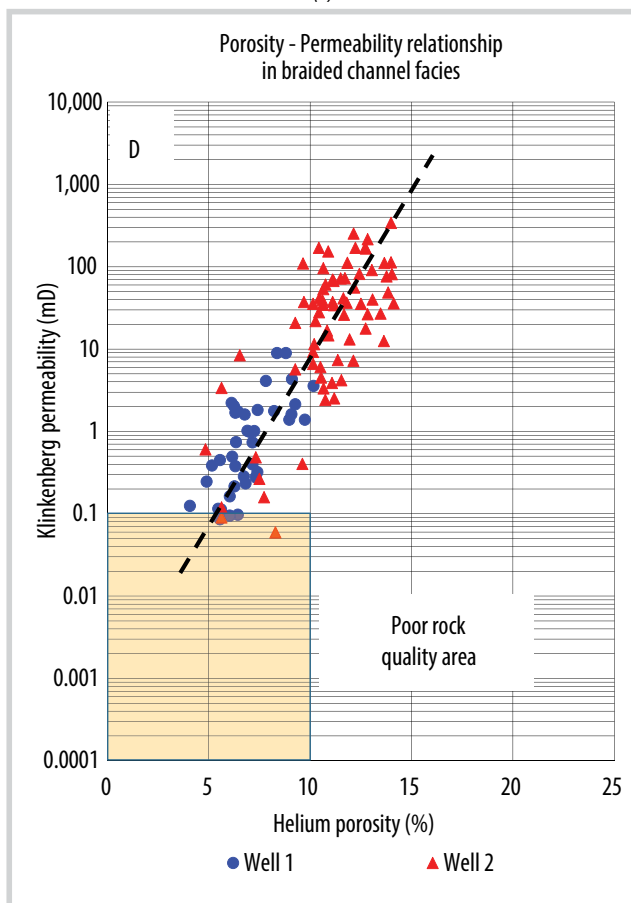
(a)



(b)



(c)



(d)

Figure 18. The poroperm relationship illustrates significant trends between facies.

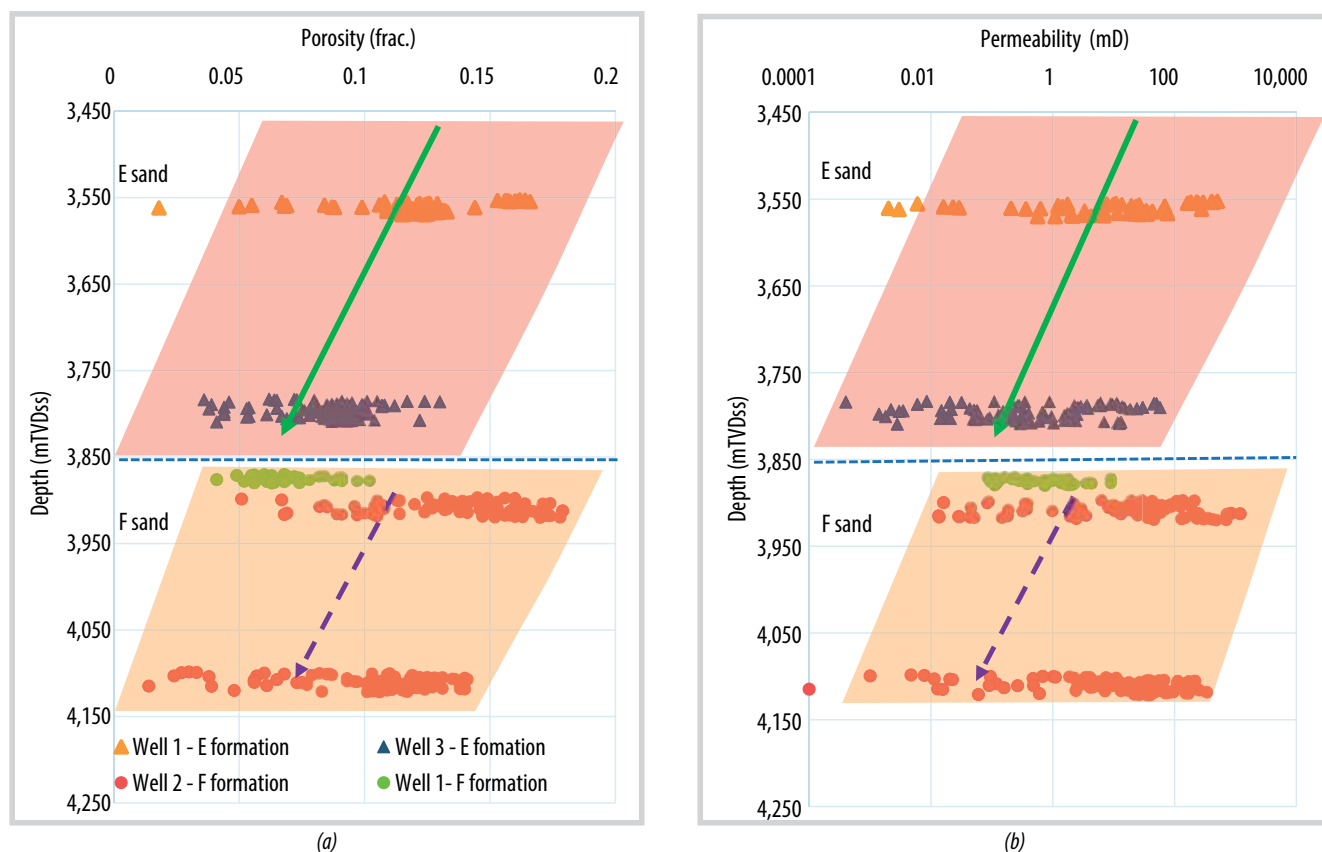


Figure 19. Core porosity (a) and core permeability, (b) vs. true vertical depth subsea cross plots.

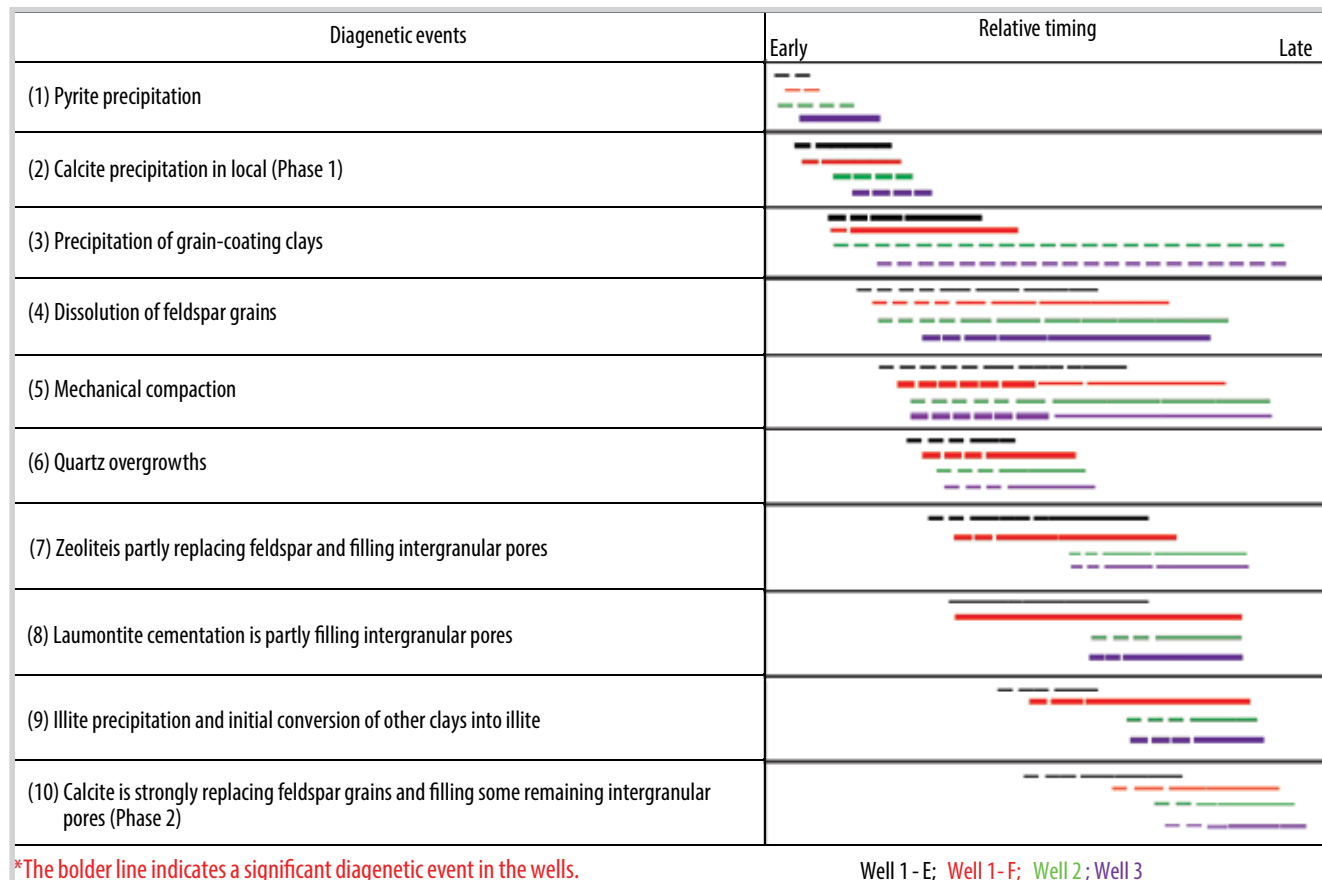


Figure 20. Paragenetic sequences across all wells.

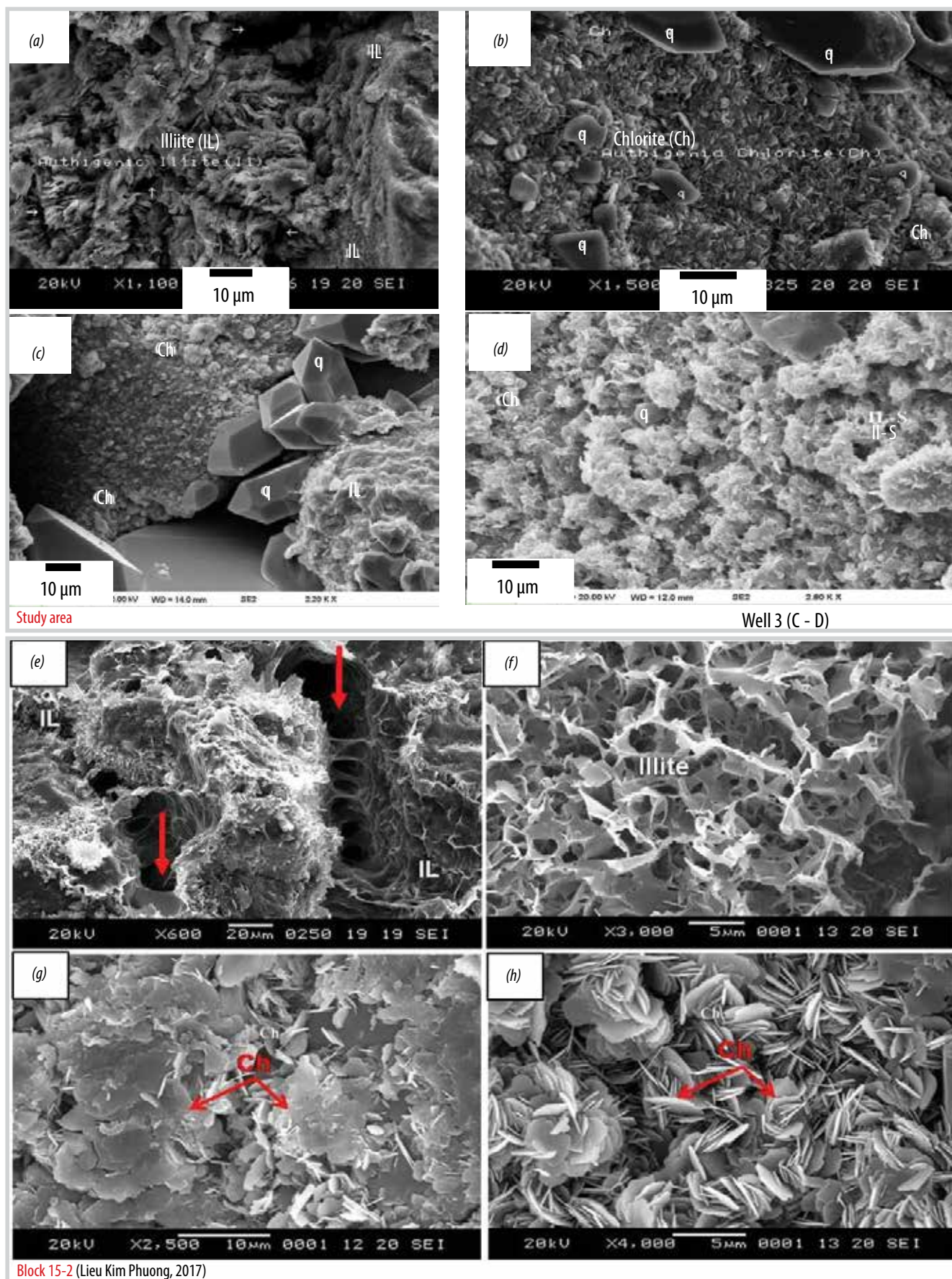


Figure 21. Morphologies of clay minerals in formation E in the study area compared to sediments in Block 15-2, Cuu Long basin [7].

5. Discussion

5.1. Key geological factors impacting porosity and permeability in sandstone reservoir

5.1.1. Depositional environment

Based on the preceding observations, the lacustrine/deltaic-sandflat, channel, braided channel, and overbank deposits show significant differences in porosity and permeability. The overbank succession shows the lowest values (approximately $\Phi_{\text{avg.}} = 5.9\%$, $K_{\text{avg.}} = 0.1$ mD); moderately higher values are observed in the channel and braided channel facies (about $\Phi_{\text{avg.}} = 9.7\%$, $K_{\text{avg.}} = 28.8$ mD and $\Phi_{\text{avg.}} = 9.5\%$, $K_{\text{avg.}} = 34.9\%$, respectively); and the highest measured values occur in lacustrine shoreface/deltaic-sandflat facies. There is a good correlation of porosity and permeability in cross-plots of these facies (Figure 18). Well 3 and well 2 show lower porosity and low permeability ($\Phi = 10\%$, $K = 0.1$ mD) observed in several samples (marked by orange box) from the otherwise good quality lacustrine/deltaic sandflat facies (Figure 18a). In addition, the average porosity of well 3 ($\Phi_{\text{avg.}} = 8.4\%$) is lower than well 1 and well 2 ($\Phi_{\text{avg.}}$ of 12.7% and 13.3%, respectively) in these facies. Similarly, a few samples from the channel facies in well 1 and well 2 illustrate low porosity and permeability (orange box) (Figure 18b). Most overbank samples show low porosity and permeability due to very fine to fine grain sizes (Figure 18c). The braided channel samples show significant differences between well 1 and well 2. The porosity of well 2 is higher than well 1 (approximately 10.9% and 7%, respectively) (Figure 18d). The differences in poroperm quality between the four facies reflect different grain-size ranges in the same depositional setting and the variable influence of diagenetic alteration.

5.1.2. Compaction process

Compaction can be illustrated through plots between porosity and permeability versus depth. All show an inverse relationship with porosity decreasing with depth in a particular formation (Figures 20a and 20b). However, well 1_F is less porous than sandstone F in the upper part of well 2 because the cementation is locally strong, especially the development of quartz (overgrowth) cement (from 11% up to 15%, Figure 16b). Petrography shows quartz is widespread as large, euhedral and syntaxial overgrowth crystals (up to 10s and 100s μm in length), which can completely fill the remaining intergranular pores and block pore throats in well 1_F.

5.1.3. Diagenetic process

Based on the above investigations and burial-history locations, the main diagenetic events observed in sandstones E and F are summarised in Figure 21.

Some parts of sandstones E and F show more advanced diagenetic textures such as moderate compaction, strong development of quartz and albite overgrowths, pore-filling zeolites and calcite cements. Furthermore, the dissolution of unstable detrital grains and their conversion to more stable phases are also quite common. For instance, feldspar grains are partly dissolved or replaced by laumontite, zeolite and/or calcite. This suggests that the sandstone has been transformed into hydrothermal cross-flows at moderate burial depths. Cements and authigenic minerals consist mainly of quartz overgrowths (commonly 7 - 9% in formation E and 11 - 15% in formation F), zeolites (5 - 8% and 5 - 10%, respectively) with small amounts of calcite and authigenic clays. Zeolite and calcite often form patches enclosing closely-packed detrital grains or filling in isolated intergranular pores. Remnant primary porosity was protected by the development of quartz and albite overgrowths. Grain contacts are mainly long and concavo-convex types, tending to minimise the dimensions of pore throats.

5.2. Comparison of diagenesis between the study area and a nearby area

The study area is located near Block 15-2 where a study was conducted on formation E [7, 8]. Their work concluded that the main factors influencing rock quality were compaction, cementation, and dissolution of unstable grains. My work concludes that the porosity and permeability in the studied wells are controlled by depositional setting variably overprinted by cementation and mechanical compaction. Authigenic clay minerals as pore-linings or in grain-surrounding coats have destructive effects on porosity and permeability. The destructive effects of increasing clay content are similar in both areas (Figures 21 a-d vs. e-f).

6. Conclusions

The quality of reservoir sands in the study area is evaluated by integrating all petrography, X-ray diffraction, Routine core analysis, and special core analysis data sets. The results quantify variations in the internal properties of the sandstone reservoirs. Based on the results, the conclusions of this study are:

- There are four core-defined depositional facies, namely: (i) lacustrine shoreface/deltaic sandflat (channel abandonment) sands which entrain numerous mud layers; (ii) channel sands which are generally indicated by fining-upward, bell shapes in GR and mostly found in formation E; (iii) braided channel sands which are characterised by poorer sorting with mostly blocky shapes in GR, and mostly abundant in the formation F; (iv) the overbank succession which shows the lowest poroperm values. Moderately higher poroperm values are observed in the channel and braided channel facies and the highest values tend to occur in lacustrine shoreface/deltaic-sandflat (channel abandonment) facies.

- Rock property measures across the E and F formations show porosity and permeability values ranging from low to high. Generally, there is a tie to the depositional setting. But in the intervals that are more affected by diagenesis and hydrothermal fluid crossflows, the enhanced formation of authigenic cements can degrade what were good quality sands at the time of deposition.

- The curvature of capillary pressure curves indicates the rock quality. Some samples show a gentle curvature that relates to reduced permeability, poorer sorting, finer grain sizes and the impact of calcite cements.

- Thin-section study shows that rock quality was significantly controlled by a combination of mechanical and chemical compaction, as shown by grain contacts ranging from point-to-point to long-axis rotation, and concavo-convex styles being present in all three wells.

- The negative relationship between total clay minerals and poroperm suggests that clay minerals reduce porosity and permeability. Pore-lining chlorite is directly precipitated onto detrital surfaces of grains and extends into pore space, leading to decreasing permeability. Authigenic illite also decreases permeability by blocking pore throats.

- Chlorite is more abundant in sandstone E than in the sandstone F. Chlorite tends to develop in the sandstones which are richer in volcanic fragments. By contrast, illite is present in the sandstone F at much higher levels than in the sandstone E, thus, illite is likely a weathering product, but diagenetic illite is also created by reactions of smectite with pore fluids during deep burial.

- Calcite cements can fill pores, reducing permeability and porosity in all wells. It can show a patchy

or uneven distribution and was mostly generated in early diagenesis.

- Compaction is illustrated in plots of porosity and permeability with depth. These plots show an inverse relationship with poroperm decreasing with depth.

- Sandstones E and F have experienced a complex diagenetic evolution as follows: (1) (2) pyrite and calcite precipitation, (3) precipitation of grain-coating clays, (4) dissolution of feldspar grains, (5) mechanical compaction, (6) quartz overgrowths, (7) zeolites partly replacing feldspars, (8) laumontite cementation, (9) illite precipitation, (10) calcite strongly replacing feldspar grains.

- A comparison with a result from a nearby area shows the depositional rock quality of formation E in that area was similarly influenced by diagenetic processes, such as compaction, cementation, and dissolution. The study in the adjacent area concludes that porosity and permeability were greatly impacted by the formation of authigenic clays, such as chlorite or illite, as well as mechanical compaction.

Acknowledgements

I am very grateful to my supervisor, Prof. John Keith Warren, who continually and convincingly conveyed a spirit of challenge throughout my research.

I would also like to thank the Exploration and Production Centre of the Vietnam Petroleum Institute and the Vietnam National Oil and Gas Group for providing the dataset for this research.

References

[1] Robert J. Morley, Bui Viet Dung, Nguyen Thanh Tung, A.J. Kullman, Robert T. Bird, Nguyen Van Kieu, and Nguyen Hoai Chung, "High-resolution Palaeogene sequence stratigraphic framework for the Cuu Long basin, offshore Vietnam, driven by climate change and tectonics, established from sequence biostratigraphy", *Palaeogeography, Palaeoclimatology, Palaeoecology*, Vol. 530, pp. 113-135, 2019. DOI: 10.1016/j.palaeo.2019.05.010.

[2] Nguyen Xuan Huy, Bae Wisup, Ngo Thuong San, V.T. Xuan, J. Sung Min, and Kim D.Y., "Fractured basement reservoir and oil displacement mechanism in White Tiger field, offshore Vietnam", *AAPG Search and Discovery Article, Singapore*, 16 - 19 September 2012.

[3] Tran Le Dong and Phung Dac Hai, "Cuu Long

sedimentary basin and petroleum resources”, *The petroleum geology and resources of Vietnam*, Science and Technics Publishing House, 2007.

[4] William Jay Schmidt, Bui Huy Hoang, James W. Handschy, Vu Trong Hai, Trinh Xuan Cuong, and Nguyen Thanh Tung, “Tectonic evolution and regional setting of the Cuu Long Basin, Vietnam”, *Tectonophysics*, Vol. 757, pp. 36 - 57, 2019. DOI:10.1016/j.tecto.2019.03.001.

[5] “High resolution biostratigraphy report well 1, Block X, Cuu Long basin”. 1974.

[6] Robert L. Folk, *Petrology of sedimentary rocks*. Hemphill Diesel Eng Schools, 1974.

[7] Lieu Kim Phuong, Le Thi Thu Hang, Nguyen Van Hieu, and Nguyen Minh Nhut, “Characterization

of petrography and diagenetic processes influence on porosity and permeability of Oligocene sandstone reservoir rocks, Block 15-2 in Cuu Long basin”, *International Journal of Engineering Research and Applications*, Vol. 7, No. 6, pp. 62 - 73, 2017. DOI:10.9790/9622-0706076273.

[8] Ho Minh Toan, Lieu Kim Phuong, Doan Thi Thuy, and Bui Thi Ngoc Phuong, “Generation of authigenic clay minerals during diagenesis and their influences on porosity and permeability of Oligocene sandstones reservoir rocks, from a well in the west of Cuu Long basin”, *Science & Technology Development Journal*, Vol. 17, No. 3, pp. 21 - 26, 2014. DOI: 10.32508/stdj.v17i3.1456.

SUPERVISED MACHINE LEARNING APPLICATION OF LITHOFACIES CLASSIFICATION FOR A HYDRODYNAMICALLY COMPLEX GAS - CONDENSATE RESERVOIR IN NAM CON SON BASIN

Nguyen Ngoc Tan, Tran Ngoc The Hung, Hoang Ky Son, Tran Vu Tung

Bien Dong Petroleum Operating Company (BIENDONG POC)

Email: sonhk@biendongpoc.vn

<https://doi.org/10.47800/PVJ.2022.06-03>

Summary

Conventional integration of rock physics and seismic inversion can quantitatively evaluate and contrast reservoir properties. However, the available output attributes are occasionally not a perfect indicator for specific information such as lithology or fluid saturation due to technology constraints. Each attribute commonly exhibits a combination of geological characteristics that could lead to subjective interpretations and provides only qualitative results. Meanwhile, machine learning (ML) is emerging as an independent interpreter to synthesise all parameters simultaneously, mitigate the uncertainty of biased cut-off, and objectively classify lithofacies on the accuracy scale.

In this paper, multiple classification algorithms including support vector machine (SVM), random forest (RF), decision tree (DT), K-nearest neighbours (KNN), logistic regression, Gaussian, Bernoulli, multinomial Naïve Bayes, and linear discriminant analysis were executed on the seismic attributes for lithofacies prediction. Initially, all data points of five seismic attributes of acoustic impedance, Lambda-Rho, Mu-Rho, density (ρ), and compressional wave to shear wave velocity (VpVs) within 25-metre radius and 25-metre interval offset top and base of reservoir were orbitally extracted on 4 wells to create the datasets. Cross-validation and grid search were also implemented on the best four algorithms to optimise the hyper-parameters for each algorithm and avoid overfitting during training. Finally, confusion matrix and accuracy scores were exploited to determine the ultimate model for discrete lithofacies prediction. The machine learning models were applied to predict lithofacies for a complex reservoir in an area of 163 km².

From the perspective of classification, the random forest method achieved the highest accuracy score of 0.907 compared to support vector machine (0.896), K-nearest neighbours (0.895), and decision tree (0.892). At well locations, the correlation factor was excellent with 0.88 for random forest results versus sand thickness. In terms of sand and shale distribution, the machine learning outputs demonstrated geologically reasonable results, even in undrilled regions and reservoir boundary areas.

Key words: Lithofacies classification, reservoir characterisation, seismic attributes, supervised machine learning, Nam Con Son basin.

1. Introduction

Sand30 is a major gas - condensate reservoir in Hai Thach field. This reservoir has one exploration well and three production wells with very different production performance [1]. Many studies have been conducted to better understand, characterise and model Sand30 [1 - 4]. Reservoir extent and lithofacies distribution are the main focus of the current study.

Machine learning has been shown to be capable of complementing and elevating human analysis by objectively examining input data and automatically repeating the calculation until the best output is determined. Because of this benefit, machine learning has been widely used in recent years in the oil and gas business, such as for lithofacies classification [5 - 7], depositional facies prediction [8, 9], well log correlation [10, 11], seismic facies classification [12, 13], and seismic facies analysis [14].

In this study, supervised machine learning was used to predict lithofacies using classification techniques in-



Date of receipt: 15/5/2022. Date of review and editing: 15/5 - 23/6/2022.

Date of approval: 27/6/2022.

cluding decision tree, support vector machine, and random forest, etc. There are five steps in the overall workflow for this investigation, as shown in Figure 1. First, all seismic data from 5 inversion cubes, including acoustic impedance (AI), Lambda-Rho (LR), Mu-Rho (MR), density, and compressional wave to shear wave velocity ratio (VpVs), were recovered from within 25 m of 4 drilled holes. They were also classified into two groups based on well log data: reservoir and non-reservoir. To ensure that data

was labelled correctly, seismic well ties were meticulously conducted. Second, those seismic data were thoroughly examined in order to determine whether or not they were related to facies data. Only seismic data with a good correlation with facies was employed as a training dataset for machine learning. Third, the supervised machine learning was used to determine the best models from the data. Fourth, those models were applied to predict lithofacies for the whole reservoir. Finally, the anticipated facies were retrieved from the map or raw data and compared to the well or present inversion seismic data to assess their quality and reliability.

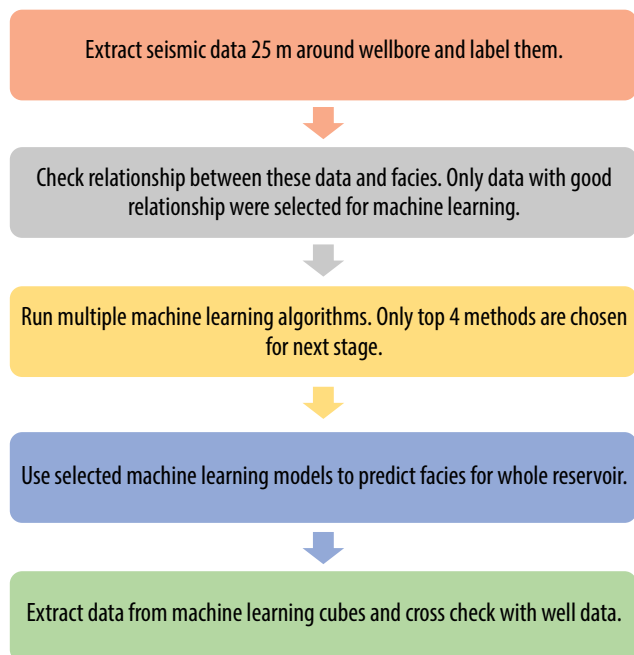


Figure 1. Overall workflow.

2. Data generation and visualisation

The input data included available well logs from four drilled holes and five seismic inversion cubes. Well logs included gamma ray, interpreted facies logs used for zonation and facies classification, density and sonic used for seismic well tie. All well data were carefully checked before making the seismic well tie. The purpose of this step was to ensure that all the seismic data and well logs were consistent, as shown in Figure 2.

Five seismic inversion cubes were then exported using orbital extraction (Figure 3) with radius of 25 m, which corresponds to the minimum seismic bin size and therefore the best input for obtaining the most reasonable correlation between well log data and seismic data. Because

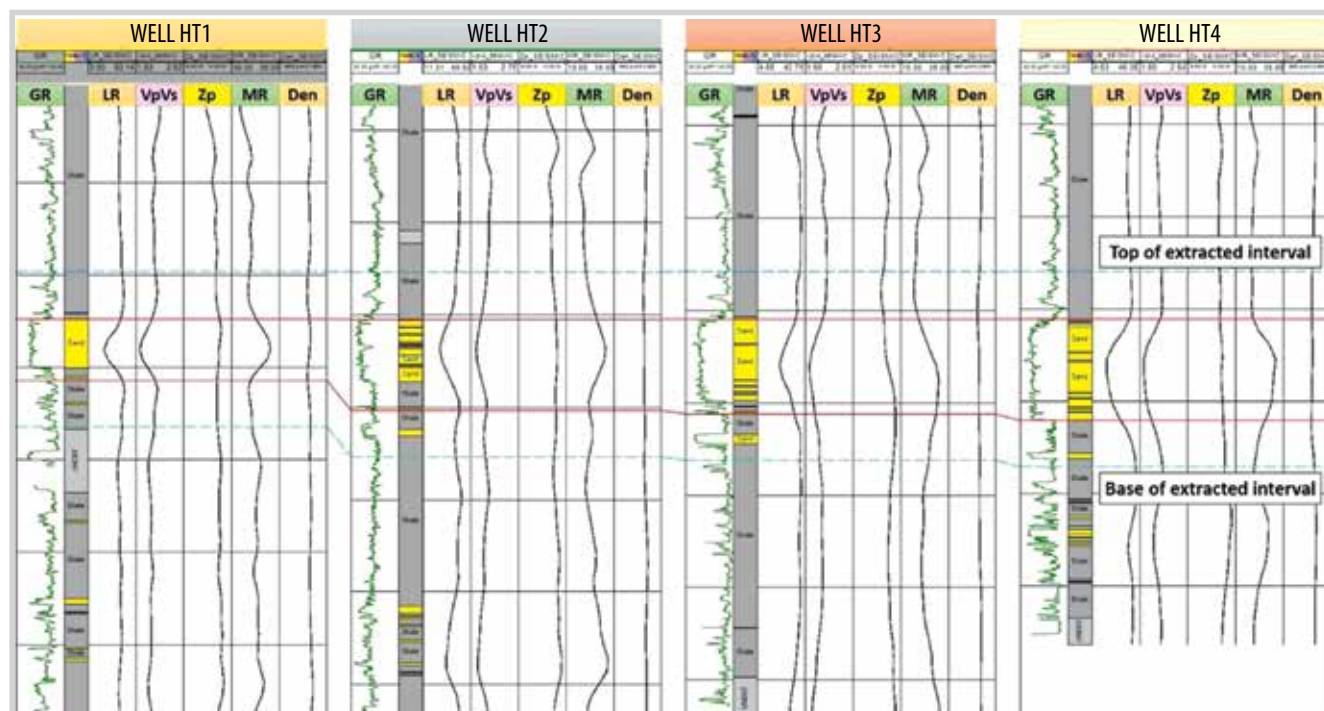


Figure 2. Results of seismic well tie.

the extraction takes the average of nearby grid values, the extraction radius should not be less than the minimum bin size in order to avoid skipping the surrounding wellbore information. On the other hand, the depth of investigation of well logging tools is very close to the wellbore wall, only a few centimetres to metres beyond the wall;

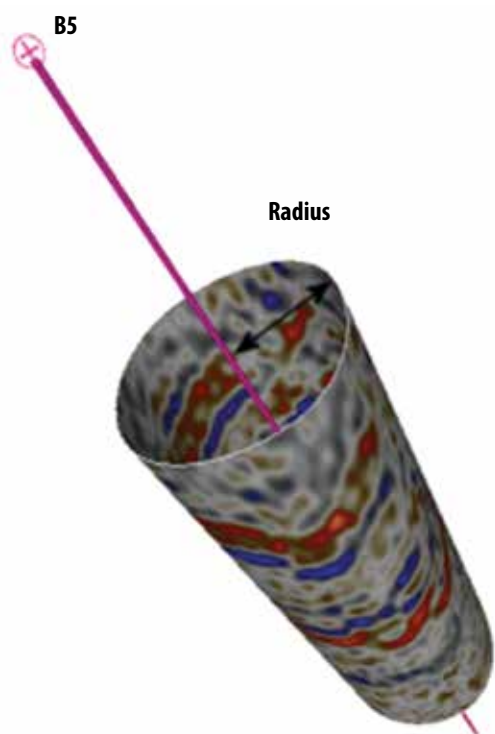


Figure 3. Orbital extraction.

thus, the smaller the extraction radius, the better the correlation. Some trials with extraction radius larger than 25 m were also carried out; however, the achieved correlation was degraded. The studied interval included reservoir interval and 25 m above the top and below the base of reservoir (half of average reservoir thickness of 50 m) which is considered the best representative for facies ratio of reservoir/non-reservoir samples. Before being used for machine learning, these data were conditioned and tagged with facies (reservoir and non-reservoir) using the seismic well tie results (Figure 2). The extracted dataset comprised of a total of 5,515 valid samples, and reservoir to non-reservoir facies ratio was approximately 3:4.

Density curve histograms and heat map were used to determine which qualities were the most related to facies. The best markers for facies indication in this study were Lambda-Rho, VpVs, and Mu-Rho. There was relatively clear separation between reservoir and non-reservoir facies in those curves but not for acoustic impedance (Zp) and density (Den) (Figure 4). Similarly, the heat map results which showed correlation between seismic properties and facies also revealed the same conclusion by correlation factor (0.7 for Lambda-Rho and VpVs, and 0.47 for Mu-Rho) (Figure 5). For those reasons, only 3 properties Lambda-Rho, VpVs and Mu-Rho were used as inputs for machine learning in the next step.

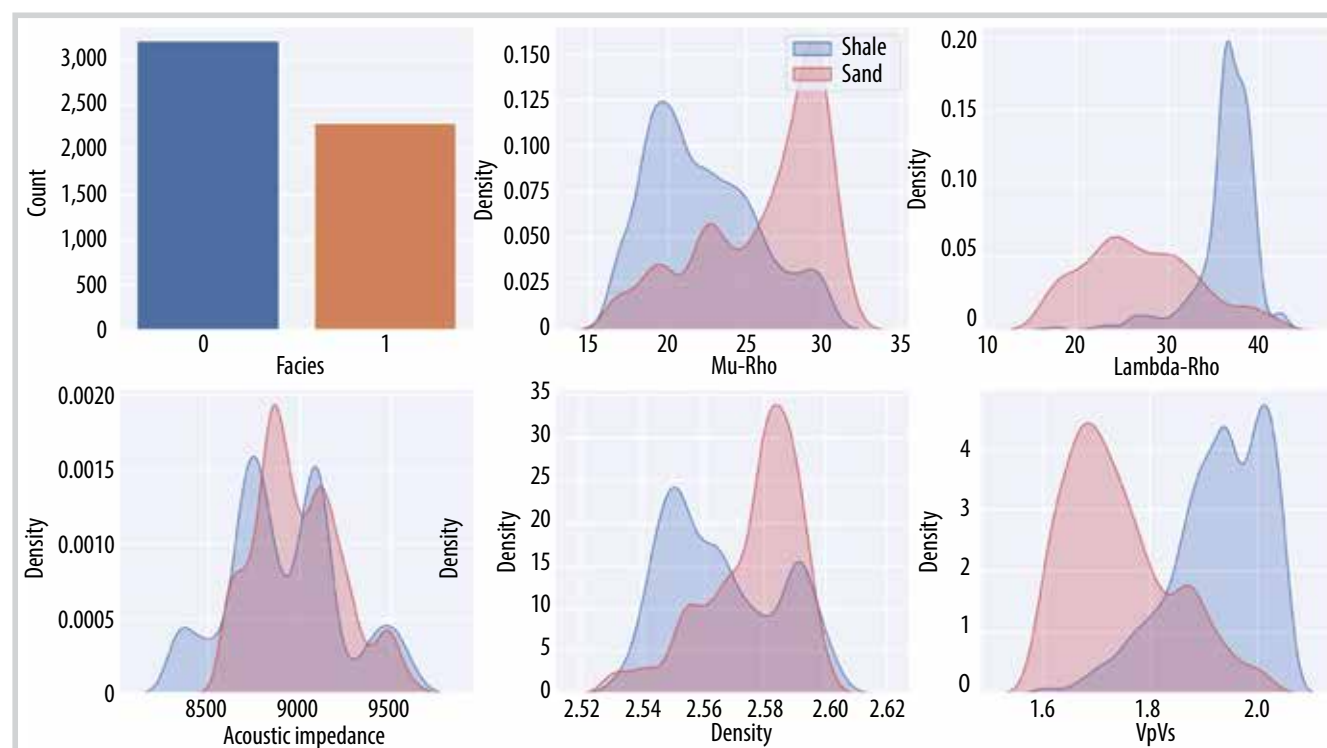


Figure 4. Density curve histogram for seismic attributes.

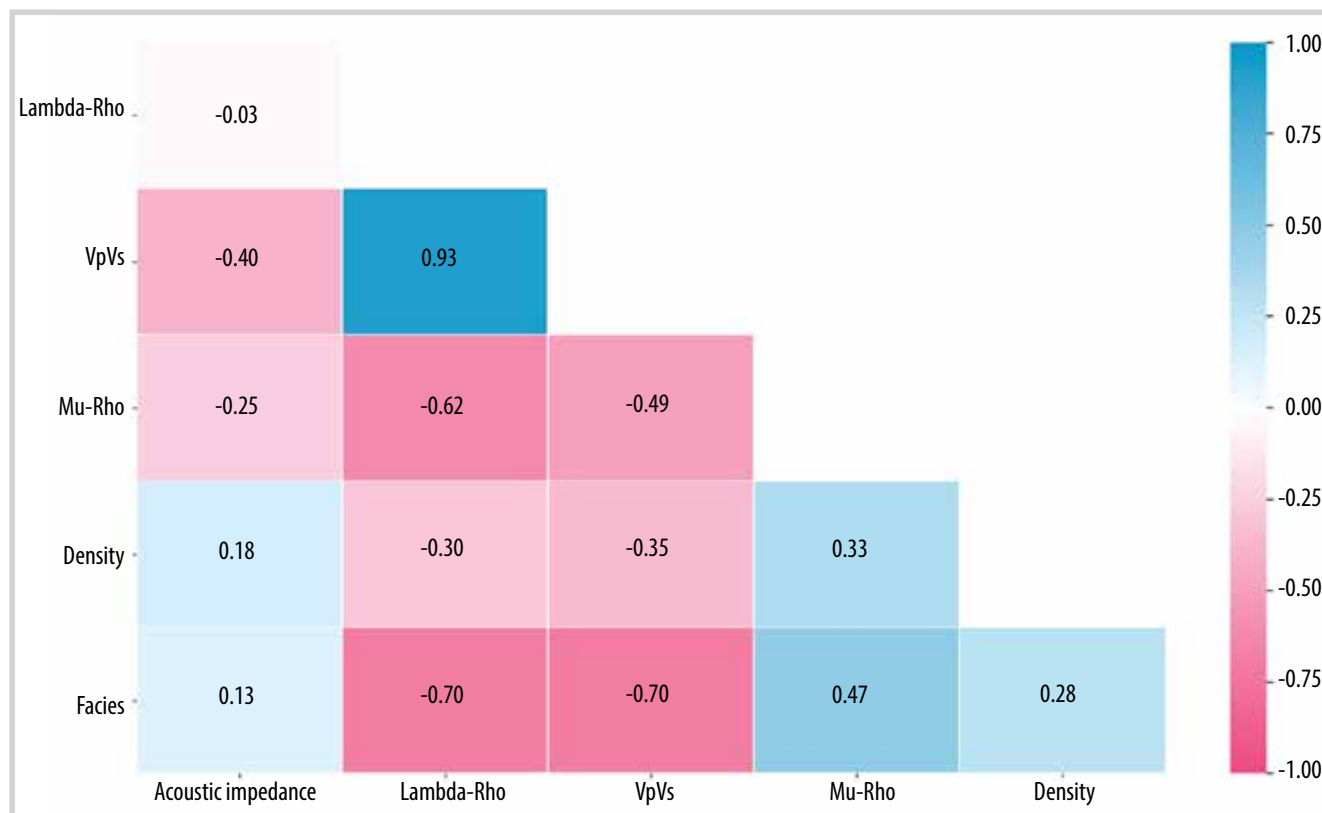


Figure 5. Heat map for 5 seismic properties versus facies.

Table 1. Accuracy score of facies prediction

Method	Accuracy on training set	Accuracy on test set
K-nearest neighbours	0.94	0.92
Decision tree classifier	1.00	0.90
Support vector machine	0.90	0.90
Random forest	0.88	0.87
Logistic regression classifier	0.87	0.86
Bernoulli classifier	0.87	0.86
Linear discriminant analysis	0.87	0.86
Gaussian Naïve Bayes	0.86	0.86

3. Machine learning approach

True positive (TP), true negative (TN), false positive (FP), and false negative (FN) are the four categories of prediction outcomes used in this study. True negative denotes that models correctly predict non-reservoir facies, while true positive says that reservoir facies are accurately predicted. On the other hand, there are two kinds of errors that could be encountered: false positive and false negative. False positive means facies that are predicted to be reservoirs but are actually non-reservoirs, whereas false negative represents facies that are predicted to be non-reservoirs but are actually reservoirs. Both error types reduce model accuracy, but in terms of HIIP calculation, the false positive type error is more severe than the false negative type because it can result in an overestimation

of reservoir facies, which is the main contributor to HIIP. As a result, low false positive error is one of the most important factors for model selection. The following formula was used to compute the accuracy score:

$$Accuracy\ score = (True\ positive + True\ negative) / Total$$

At the beginning of the study, many supervised classification algorithms were investigated, including logistic regression, Gaussian Naïve Bayes, Bernoulli Naïve Bayes, multinomial Naïve Bayes, linear discriminant analysis, support vector machine, K-nearest neighbours, decision tree, and random forest, as shown in Table 1, to find the best four algorithms based on the accuracy score for latter stage.

At the second stage, only the top four algorithms were selected to build the model. At this stage, cross

validation and GridSearchCv technique were used to optimise hyper-parameters and avoid overfitting.

For cross validation, the test data would be kept separate and reserved for the final evaluation step to check the "reaction" of the model when encountering completely unseen data. The training data would be randomly divided into K parts (K is an integer, usually either 5 or 10). The model would be trained K times, each time one part would be chosen as validation data and K-1 parts as training data. The final model evaluation results would be the average of the evaluation results of K training times. With cross validation, the evaluation is more objective and precise.

In addition, one of the important things about machine learning is optimising parameters, called hyper parameters, which cannot be learned directly. Each model can have many hyper parameters and finding the best combination of parameters can be considered a search problem. In this study, GridSearchCv was used to find the optimal combination.

4. Machine learning results and validation

The average accuracy score of K training times is listed in Table 2. Random forest achieved the highest score, fol-

lowed by support vector machine, K-nearest neighbours, and decision tree.

Similarly, the confusion matrix report system was also used in this study to evaluate the performance of each model. The confusion matrix is as follows:

$$\begin{bmatrix} \text{True negative} & \text{False positive} \\ \text{False negative} & \text{True positive} \end{bmatrix}$$

According to the confusion matrix, random forest had

Table 2. Average accuracy score

Machine learning algorithm	Average accuracy score
Random forest	0.907
Support vector machine	0.896
K-nearest neighbours	0.895
Decision tree	0.892

Table 3. Confusion matrix

Method	Confusion matrix for test set
Random forest	$\begin{bmatrix} 593 & 43 \\ 53 & 414 \end{bmatrix}$
K-nearest neighbours	$\begin{bmatrix} 588 & 48 \\ 60 & 407 \end{bmatrix}$
Support vector machine	$\begin{bmatrix} 593 & 43 \\ 76 & 391 \end{bmatrix}$
Decision tree	$\begin{bmatrix} 585 & 51 \\ 73 & 394 \end{bmatrix}$

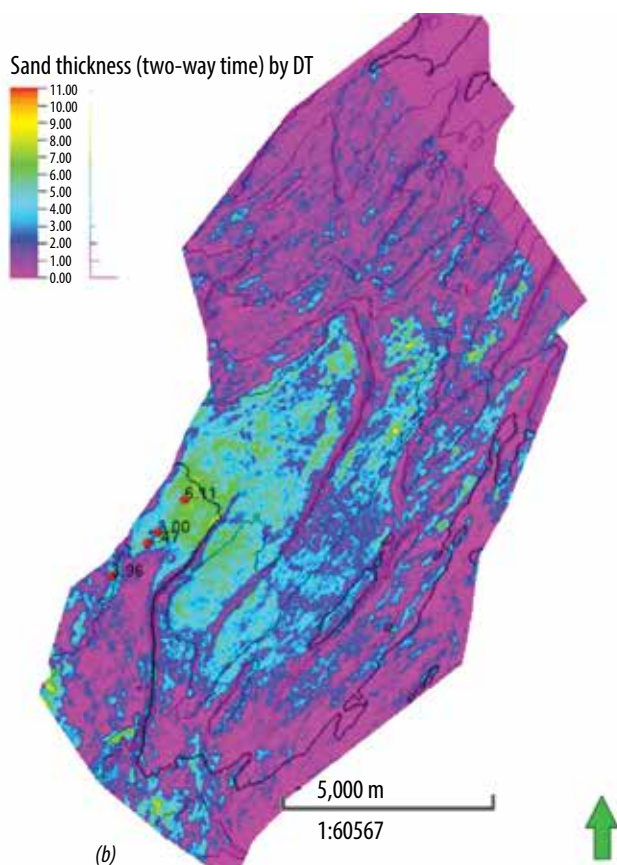
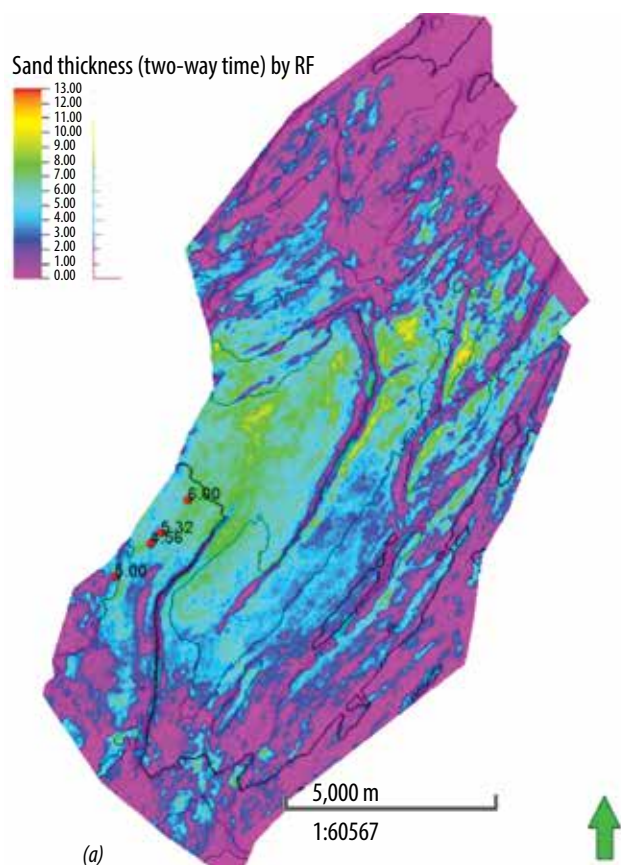


Figure 6. Sand thickness (two-way time) map by random forest (a) and decision tree (b).

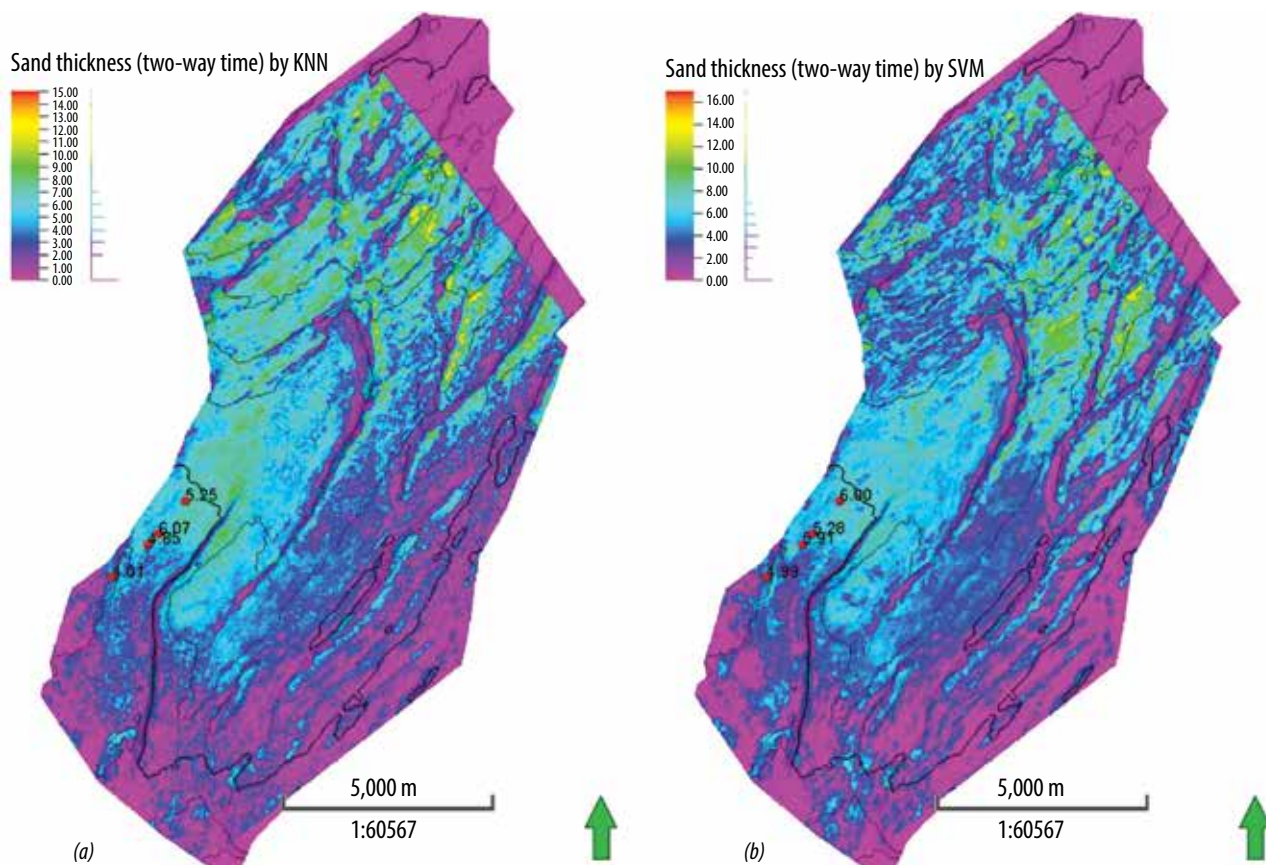


Figure 7. Sand thickness (two-way time) map by K-nearest neighbours (a) and support vector machine (b).

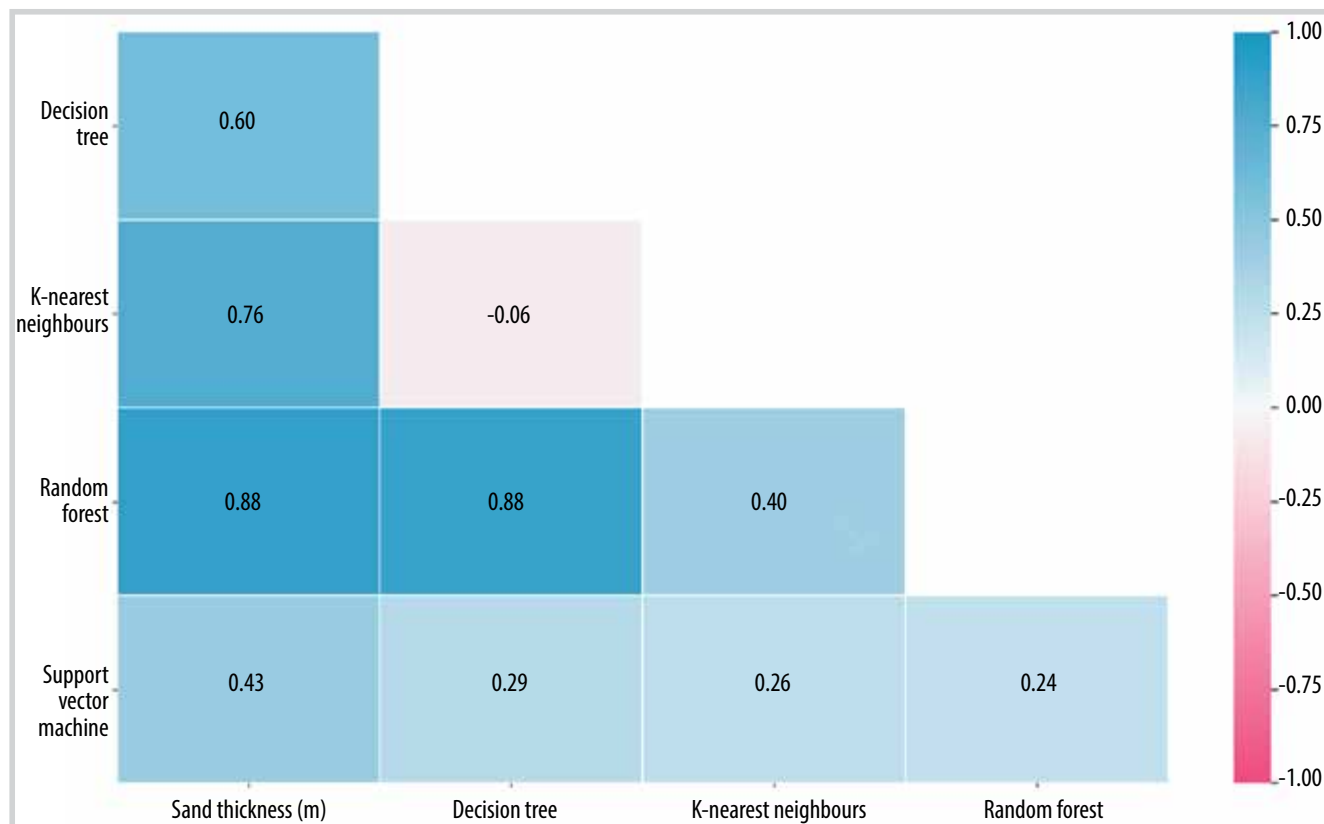


Figure 8. Correlation between machine learning cubes versus sand thickness at well location.

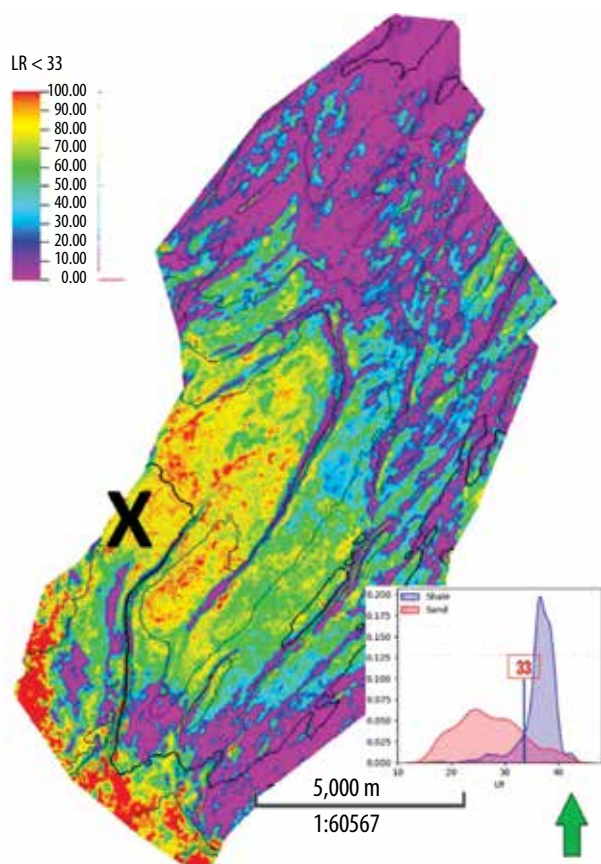


Figure 9. Lambda-Rho attribute with threshold below 33 (as defined by seismic histogram).

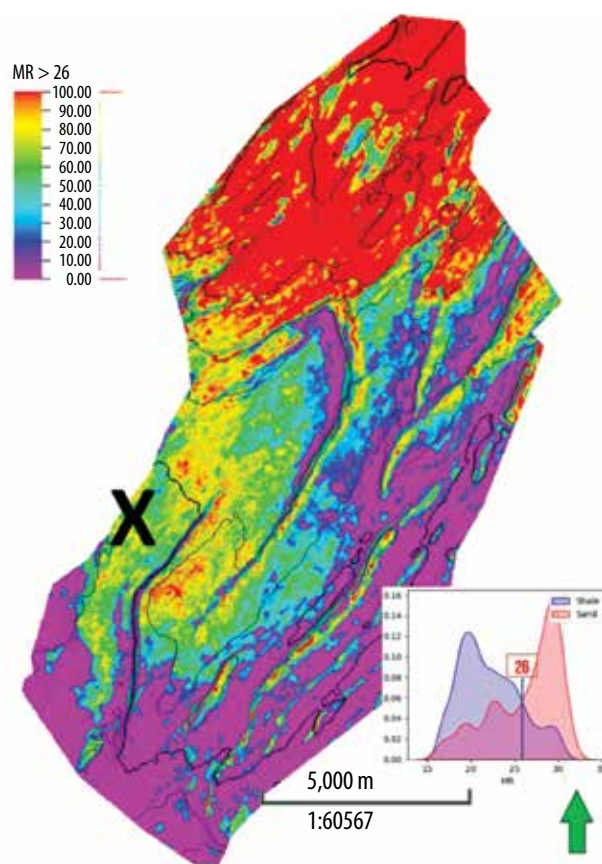


Figure 11. Mu-Rho attribute with threshold above 26 (as defined by seismic histogram).

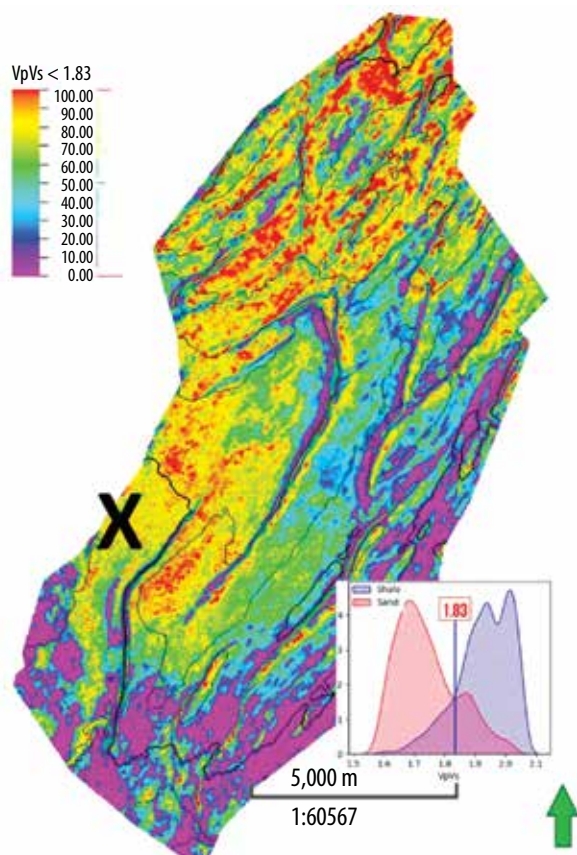


Figure 10. VpVs attribute with threshold below 1.83 (as defined by seismic histogram).

the lowest total false prediction (false positive + false negative) results (96 errors), followed by K-nearest neighbours (108 errors), support vector machine (119 errors), and decision tree (124 errors). Regarding, false positive, the most serious errors, random forest had the fewest number of errors (43 errors) and decision tree had the highest (51 errors).

Properties and maps from four machine learning cubes (Figures 6 and 7) were also extracted at well locations to determine the relationship between actual well sand thickness and reservoir thickness from machine learning using a heat map based on Pandas correlation function (Figure 8). The correlation between well data and random forest cube was the highest (0.88) on the heat map, followed by K-nearest neighbours (0.76), decision tree (0.60), and support vector machine (0.43). It is likely that the random forest algorithm is the most dependable approach for this investigation.

5. Discussions and application

Attribute maps, which may be utilised as guidelines for property populations in 3D model, are one of the most notable contributions of seismic data. Normally, single

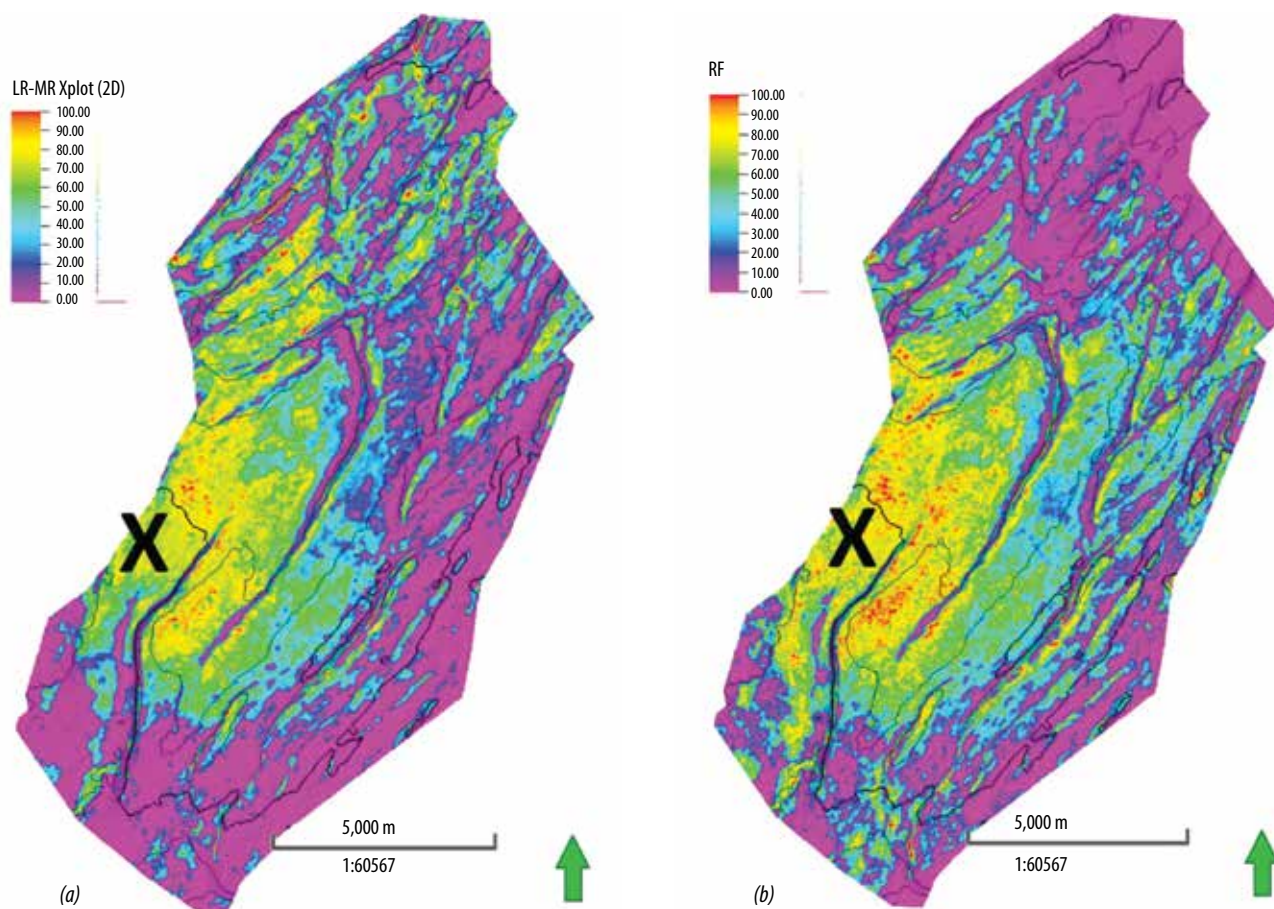


Figure 12. Lambda-Rho - Mu-Rho cross-plot attribute (a) and random forest results (b).

seismic attributes may give reasonable results around the drilled well areas but questionable for far away areas. For example, in our location, Lambda-Rho cut-off attributes (Figure 9) showed good results in the drilled area (X area), but lots of non-geological anomalies in far away areas, especially in the southern area. VpVs and Mu-Rho also had similar performance (Figures 10 and 11). Consequently, selecting the best attribute for further study in this case is very challenging and risky. Therefore, in our location, the combination between Lambda-Rho and Mu-Rho was used to minimise the potential risks (Figure 12a). However, this procedure itself requires high experience from the interpreters so the results seem to be very subjective. Furthermore, only Mu-Rho and Lambda-Rho were used in this combination while VpVs was not even though it could be very valuable in terms of geological meaning.

With machine learning workflow, the number of integrated attributes can be more flexible, as long as data are correlated with each other. There are no subjective parameters used such as threshold cut-offs which seem to be very sensitive. On top of that, results from machine learning is very promising and reliable, for example, most of

non-geological anomalies in the southern part (as shown on Lambda-Rho map), and northern part (as shown on Mu-Rho and VpVs maps) were not present in random forest map and the results in the drilled area (X) are still of high quality (Figure 12b).

6. Conclusions

The main conclusions of this study can be summarised as follows:

- The traditional approach of using single seismic attribute such as Lambda-Rho, VpVs, or Mu-Rho for facies prediction leads to potential risks especially for remote areas without wells. Moreover, it highly depends on the experience of interpreters in selecting cut-off parameters;

The more advanced approach of combining seismic attributes can improve prediction accuracy but highly depends on the experience of interpreters and sometimes cannot use all available data;

- Machine learning techniques such as random forest, decision tree, K-nearest neighbours, and support vector machine were used to overcome the disadvantages of

traditional approaches by analysing all input parameters objectively. The study successfully classified facies from each other;

- Random forest was found to be the most dependable method for the study area;
- The results from machine learning are of very high quality and can be used for HIIP calculation and 3D static modelling.

Acknowledgment

The research work described herein was part of Research Project 077.2021.CNKK.QG/HDKHCN, Order 196/QD-BCT of the Vietnam Ministry of Industry and Trade.

References

- [1] Phạm Hoàng Duy, Hoàng Kỳ Sơn, Trần Ngọc Thế Hùng, và Trần Vũ Tùng, "Kết quả đo độ thấm bằng nhiều phương pháp khác nhau cho vỉa turbidite mỏ Hải Thạch, bể Nam Côn Sơn", *Tạp chí Dầu khí*, Số 2, trang 35 - 44, 2019.
- [2] Pham Hoang Duy, Hoang Ky Son, Trinh Xuan Vinh, and Tran Vu Tung, "Condensate banking characterization and quantification of improvement from different mitigations using pressure transient analysis: A case study in Hai Thach field offshore Vietnam", *Offshore Technology Conference Asia, Kuala Lumpur, Malaysia, 2 - 6 November 2020*. DOI: 10.4043/30142-MS.
- [3] Hoang Ky Son, Tran Vu Tung, Nguyen Ngoc Tan, Truong Tu Anh, Pham Hoang Duy, Tran Ngoc Trung, Trinh Xuan Vinh, and Ngo Tuan Anh, "Successful application of machine learning to improve dynamic modeling and history matching for complex gas-condensate reservoirs in Hai Thach field, Nam Con Son basin, offshore Vietnam", *SPE Symposium: Artificial intelligence - Towards a Resilient and Efficient Energy Industry*, 18 - 19 October 2021. DOI: 10.2118/208657-MS.
- [4] Hoang Ky Son, Tran Vu Tung, Nguyen Ngoc Tan, Truong Anh Tu, Pham Hoang Duy, Tran Ngoc Trung, Trinh Xuan Vinh, and Ngo Tuan Anh, "Successful case study of machine learning application to streamline and improve history matching process for complex gas-condensate reservoirs in Hai Thach field, offshore Vietnam", *SPE Middle East Oil & Gas Show and Conference*, 29 November 2021. DOI: 10.2118/204835-MS.
- [5] Leila Aliouane, Sid-Ali Ouadfeul, Nouredine Djarfour, and Amar Boudella, "Lithofacies prediction from well logs data using different neural network models", *Proceedings of the 2nd International Conference on Pattern Recognition Applications and Methods (PRG-2013)*, 2013. DOI: 10.5220/0004380707020706.
- [6] Paolo Bestagini, Vincenzo Lipari, and Stefano Tubaro, "A machine learning approach to facies classification using well logs", *SEG Technical Program Expanded Abstracts 2017*. DOI: 10.1190/segam2017-17729805.1.
- [7] Jing Jing Liu and Jian Chao Liu, "Integrating deep learning and logging data analytics for lithofacies classification and 3D modeling of tight sandstone reservoirs", *Geoscience Frontiers*, Vol. 17, No. 1, 2022. DOI: 10.1016/j.gsf.2021.101311.
- [8] Randall S. Miller, Skip Rhodes, Deepak Khosla, and Fernando Nino, "Application of artificial intelligence for depositional facies recognition - Permian basin", *Unconventional Resources Technology Conference, Denver, Colorado, USA, 22 - 24 July 2019*. DOI: 10.15530/urtec-2019-193.
- [9] Tran Vu Tung, Ngo Huu Hai, Hoang Ky Son, Tran Ngoc The Hung, and Joseph J. Lambiase, "Depositional facies prediction using artificial intelligence to improve reservoir characterization in a mature field of Nam Con Son basin, offshore Vietnam", *Offshore Technology Conference Asia, Kuala Lumpur, Malaysia, 2 - 6 November 2020*. DOI: 10.4043/30086-MS.
- [10] Hiren Maniar, Srikanth Ryali, Mandar S. Kulkarni, and Aria Abubakar, "Machine learning methods in geoscience", *SEG Technical Program Expanded Abstracts 2018*. DOI: 10.1190/segam2018-2997218.1.
- [11] Seth Brazell, Alex Bayeh, Michael Ashby, and Darrin Burton, "A machine-learning-based approach to assistive well-log correlation", *Petrophysics*, Vol. 60, No. 4, pp. 469 - 479, 2019. DOI: 10.30632/PJV60N4-2019a1.
- [12] Satinder Chopra and Kurt J. Marfurt, "Seismic facies characterization using some unsupervised machine learning methods", *SEG Technical Program Expanded Abstracts 2018*. DOI: 10.1190/segam2018-2997356.1.
- [13] Vladimir Puzrev and Chris Elders, "Unsupervised seismic facies classification using deep convolutional autoencoder", *Geophysics*, Vol. 87, No. 4, 2022. DOI: 10.1190/geo2021-0016.1.
- [14] Thilo Wrona, Indranil Pan, Robert L. Gawthorpe, and Haakon Fossen, "Seismic facies analysis using machine learning", *Geophysics*, Vol. 83, No. 5, 2018. DOI: 10.1190/geo2017-0595.1.

ACTIVATION OF A NON-ERUPTIVE WELL BY USING AN ELECTRICAL PUMP TO OPTIMISE PRODUCTION

Victorine Belomo¹, Madeleine Nitchou², Eric Donald Dongmo³, Kasi Njeudjang⁴, Gabriel Kuitse¹, Sifeu Takougang Kingni⁴

¹African Higher Institute of Management and Technological Education

²School of Geology and Mining Engineering, University of Ngaoundéré

³College of Technology, University of Buéa

⁴National Advanced School of Mines and Petroleum Industries, University of Maroua

Email: kasinj2006@yahoo.fr

<https://doi.org/10.47800/PVJ.2022.06-04>

Summary

The purpose of the study is to activate a well named X (for confidential reasons) in order to improve its production by proposing an electrical submersible pump. The nodal analysis is performed to understand the well's condition and an economic evaluation is done to determine the applicability of the project. The initial completion data, the pump placement data and the economic data are considered and used as input in PIPESIM 2017 software for operations and simulations. The results obtained from nodal analysis show that the well is in a total depletion situation. Upon analysis, the electrical submersible pump type REDA S6000N with operational diameter of 5.38 inches is appropriately chosen and installed, resulting in a flowrate of 4,891.36 stock-tank barrels per day (stb/d) with a bottom pressure of 2,735 pounds per square inch (psi). A flowrate of 5,000 stock-tank barrels per day at a pressure of 2,707 psi is obtained after optimisation of the pump through sensitivity curves. The economic balance sheet presents a net present value of USD 110,718,250, showing the profitability of the project over a period of one year.

Key words: Non-eruptive well, electrical submersible pump, nodal analysis, optimisation, sensitivity curves, economic balance sheet.

1. Introduction

The world's demand for energy keeps growing especially for hydrocarbons as they are of high and of primary importance in the industry domain, not to mention the society's needs [1 - 3]. This increasing demand is not favoured by the reducing number of discoveries done as years go on, it is then necessary to increase production in an efficient and profitable manner. Nowadays, many wells cannot rely solely on its natural energy to pull up the hydrocarbons to the surface; this is simply due to the pressure drop in the reservoirs and increase in the volume of basic sediments and water [4 - 7]. Thus, using activation methods, whose objective is to decrease the downhole pressure and enable production of hydrocarbons, is necessary. Artificial lift refers to the use of artificial means to increase the flow of liquid, such as crude oil

or water, from a production well through downhole pressure reduction. There are several different types, which are electrical submersible pumps (ESP), gas lift, progressive cavity pump, rod lift systems and hydraulic pump [8 - 11]. It is, therefore, always important to optimise oil production from existing wells by using the appropriate artificial lift [12 - 14]. Activation using an electrical submersible pump is one of the most effective and efficient methods to increase production of a depleted well [15 - 17]. For confidential reasons, the well and the field used in this paper are called well X and field X, respectively. The question which arises is in what way the differential pressure can be increased to maximise the production. This work aims at activating well X to improve production by proposing an electrical submersible pump case of an abundant water production.

The paper focuses on the configuration design of the electrical submersible pump (ESP), a nodal analysis to confirm the actual rate of the well to optimise the activated well X, and an economic evaluation. The content is, there-



Date of receipt: 23/1/2022. Date of review and editing: 23/1 - 9/2/2022.

Date of approval: 27/6/2022.

Table 1. Initial completion data

Reservoir pressure	4,000 psi
Reservoir temperature	200 °F
Productivity index	2.5 stb/d.psi
Water cut	60%
Gas - Oil ratio (GOR)	250 SCF/stb (>)
Production specific gravity	0.865
Oil formation volume factor	1.25
Maximum flow rate (MFR)	10,000 stb/d
Model	Vogel
Production tubing	9,000 ft; ID = 3.5"; OD = 5"
Packer	8,850 ft
Perforation depth	9,500 ft
Wellhead pressure	250 psi

Table 2. Data for the pump design

Operational oil rate	5,000 stb/d
Wellhead pressure	250 psi
Water cut	60%
Activation objectives by the submersible pump	Choose the appropriate pump Place the pump at the required depth Produce with the pump at an optimal rate

Table 3. CAPEX, OPEX and profits

CAPEX	OPEX	Profits
Surface and downhole equipment USD 500,000	/	Oil price: USD 75
Maintenance done on a well three times a year USD 50,000	Cost of producing one barrel of oil USD 10	Daily oil price
Running equipment cost USD 350,000	/	/
A tax of 5% on revenues	/	/

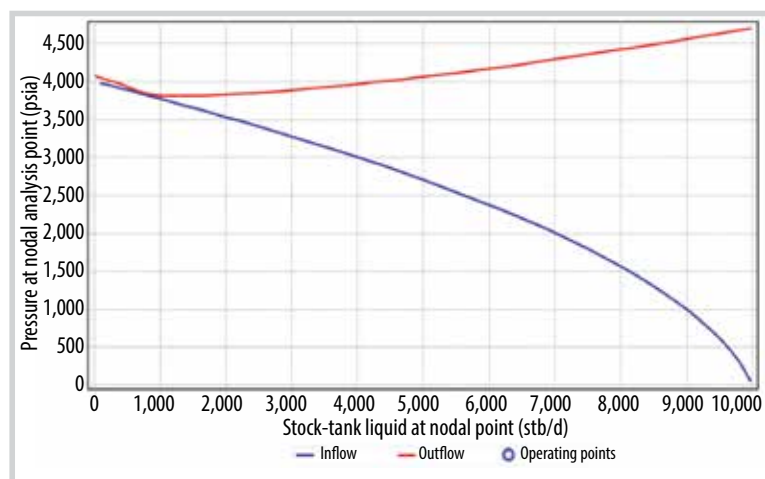


Figure 1. Nodal curve of well X: IPR/VLP.

fore, sliced into three sections: the first one presents the introduction; the second devotes to the data and highlights these obtained results followed by a discussion and the last is for conclusion.

2. Material and methods

Well X is a vertical one whose profile starts with a conductor pipe at 1,000 ft having an outer diameter (OD) = 26 inches and inner diameter (ID) = 20 inches of grade H40; a surface casing of OD = 17.5 inches and ID = 13.25 inches of grade J55; an intermediate casing of OD = 12.25 inches and ID = 9.625 inches of grade K55; and a production casing of OD = 8.5 inches and ID = 7 inches of grade C75. The well head is connected to a choke (ID = 2 inches) by a connector and the choke itself is connected to the sink by the flowline (ID = 3 inches) having a horizontal distance of 2,000 ft. The initial completion data, the pump placement and the economic data supporting the results of this paper are presented in Tables 1 to 3.

The data of Tables 1 to 3 help to achieve the initial completion of well X, develop a good design of the pump, install the pump at a required depth and conduct the nodal analysis in order to obtain an optimised flow rate of the activated well X. The PIPESIM 2017 software, nodal analysis and economic evaluation are used.

3. Results and discussions

According to the nodal analysis results shown in Figure 1, the non-eruptivity of the well is confirmed as no operating point is present on the graph: the inflow and the outflow curves do not meet, which means the well is not producing.

To make well X become productive again, it is necessary to use activation methods. An electrical submersible pump is applied in this case because of the high-water level, the desire to produce at a flow rate of 5,000 stock-tank barrels per day (initially at 4891.36 stock-tank barrels per day), the absence of gas, and an average reservoir temperature. The pump is installed after the introduction of certain elements such as the desirable flow rate, the inside tubing, the wellhead pressure and certain reservoir data.

Table 4. Pump results presentation

Results of the pump after simulations	Parameters values
Pump depth	9,000 ft
Tubing total depth	3,294.4 ft
Suction pressure of the pump	2,506.905 psi
Discharge pressure	3,795.141 psi
Differential pressure	1,288.235 psi
Number of stages	63
Frequency of the pump	60 Hz
Power of the pump	163.93 hp
Diameter of the pump	5.38"
Pump model	REDA S6000N
Downhole pressure	2,735.315 psi

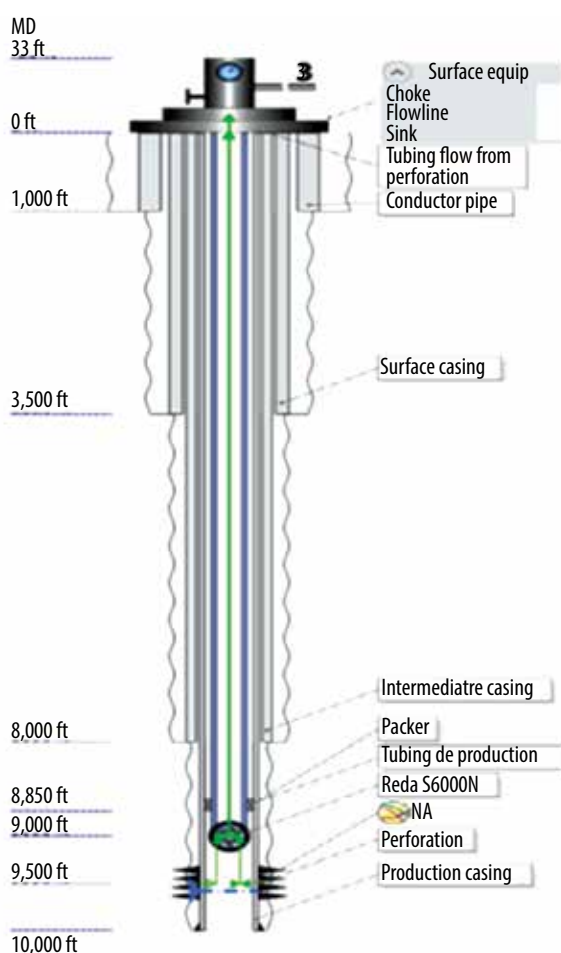


Figure 2. Installation of the pump.

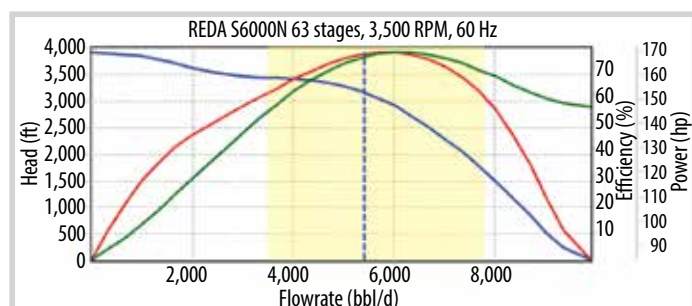


Figure 3. Appropriate performance of the pump.

Electrical submersible pump characteristics

- The standard 60 Hz producing range is from 100 barrel per day up to 90,000 barrel per day;
- Electrical submersible pump characteristics are based on a constant rotation speed, which depends on the frequency of the AC supply: 3,500 RPM with 60 Hz and 2,915 RPM with 50 Hz;
- Currently operating in wells with BHT up to 350°F;
- Efficiently lifting fluids in wells deeper than 12,000 ft;
- System efficiency ranging from 18% to 68%;
- Having a narrow production rate range;
- Not handling free gas.

The simulations performed on PIPESIM to determine the placement depth of the pump, the number of required stages, the suction pressure and discharge, the pump frequency, the pump height in the tubing, the model of the pump, and the efficiency installed are presented in Table 4 and Figure 2.

One can notice from Figure 2 that the installation of the pump at a depth of 9,000 ft is correct as it is close to the perforations. This is to reduce the bottom pressure as much as possible but also for the good cooling of the pump motor. Figure 3 shows the performance curve of the pump.

In Figure 3, the pump curves are customised for each pump in order to plot the ability to move fluids; the delivery capacity (blue curve), the pump efficiency (red curve), and power (green curve) are plotted against flow. The most important part of this performance graph is the load capacity curve, which plots the relationship between the total wellhead dynamics and the flow capacity of a specific pump. A pump can only develop a certain drop height for a given flow, and vice versa. The yellow area on the pump curve indicates the most efficient operating range of that specific pump. In this case, the dotted blue line shows that at 60 Hz, this 63-stage pump is operating in the optimum range. The flow produced by the well after installation of the pump is shown in Figure 4.

The point at which the inflow performance relationship - IPR (blue curve) and vertical lift performance - VLP (red curve) meet is marked as the op-

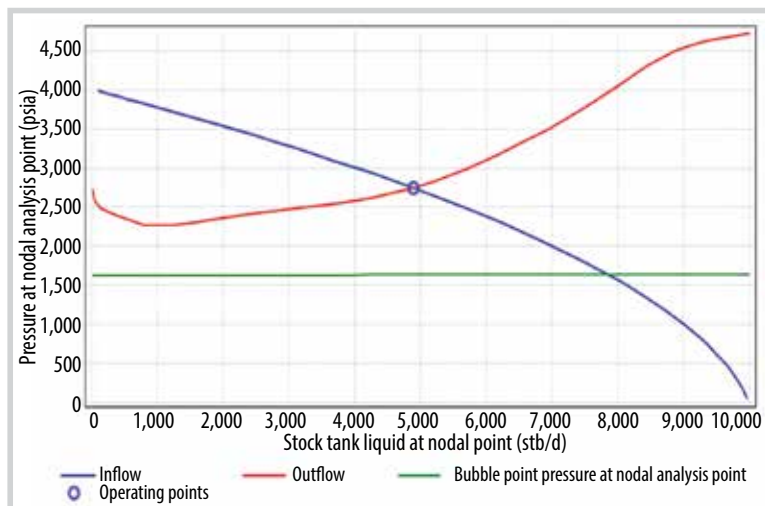


Figure 4. IPR/VLP after the installation of the pump.

Table 5. Results of the activation of the well using ESP

Operating rate	4,891,368 stb/d
Operating pressure	2,735.31 psi
Water cut	60 %
Bubble pressure	1,600 psi
GOR = 250 SCF/stb (>)	Presence of a separator at the bottom (100%)
Effectiveness of the pump	72%

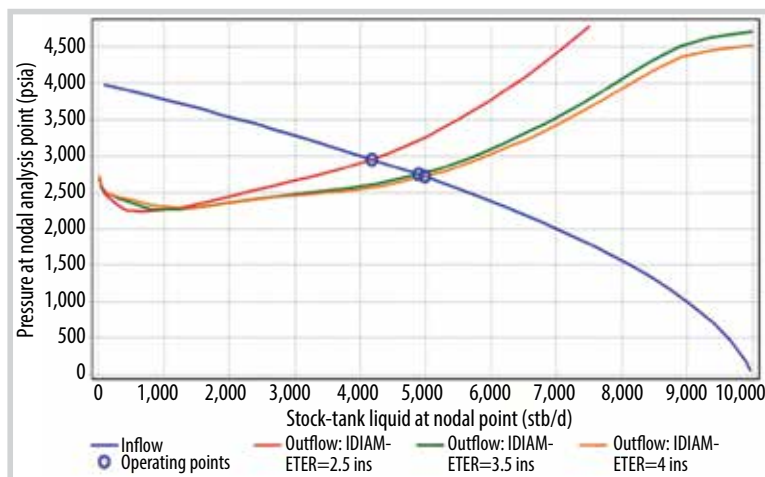


Figure 5. Tubing diameter influence on the well.

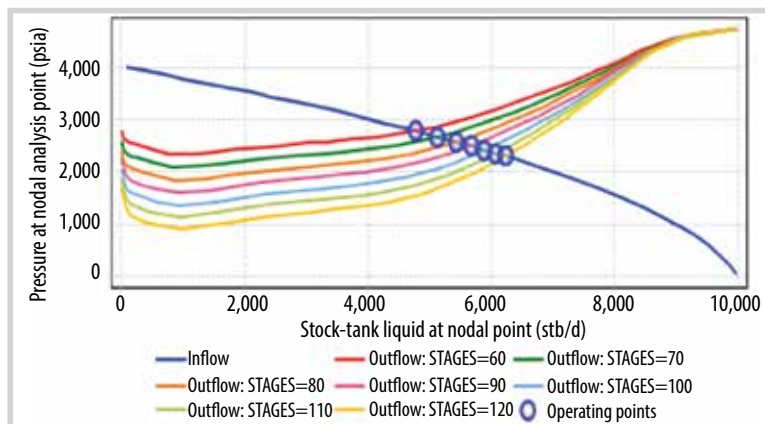


Figure 6. Influence of the number of stages on the flowrate.

erating point, which specifies the flow rate of well X and the pressure at the bottom of well X to Figure 4 and Table 5.

Even though well X becomes eruptive, it does not produce at an optimal rate. Thus, it is necessary to optimise the well by using nodal analysis from the PIPESIM software considering the sensitivity curve. In order to know the influence of the tubing diameter on production using the electrical submersible pump system and justify the casing choice, a sensitivity test is done as shown in Figure 5.

Figure 6 shows the variation of the vertical lift performance (outflow performance relationship) at different stages and their influence on the flow rate. This decreases the pressure at the bottom but increases the load on the pump which can lead to early weariness of the engine. The nodal analysis was then used to verify the impact of the variation at the wellhead and its performance on the well, the pump and the nodal point as presented in Figure 7.

From Figure 5, the variation of the tubing diameter does not significantly influence the operating point of the well. Moreover, by keeping the pump system unchanged, the same results are obtained. The sensitivity of the number of pump stages is depicted in Figure 6.

Figure 7 is a graph of pressure at nodal point against flow rate. It is easily seen that increasing the wellhead pressure decreases the flow rate and simultaneously increases the bottom hole pressure. So, it is wise to reduce the pressure at the wellhead because it renders the pump more efficient. For the safety of the well and the pump, the pressure will be reduced to 50 psi because a high production can lead to the production of sand from the formation, which can corrode the pump and the tubing. Figure 8 shows the nodal analysis curves for well X showing the optimal flow rate.

After optimisation of the well, the desired flow rate of 5,000 stock-tank barrels per day is

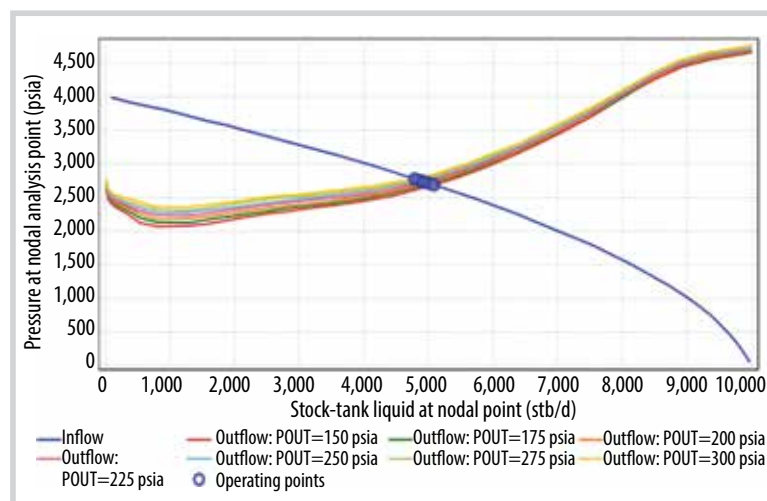


Figure 7. Pressure influence at the wellhead.

Table 6. Wellhead pressure sensitivity results

	Operating point	Stock-tank liquid at nodal analysis stb/d	Pressure at nodal analysis psi
1	P _{OUT} = 150 psi	5,091.4	2,672.885
2	P _{OUT} = 175 psi	5,045.852	2,687.208
3	P _{OUT} = 200 psi	49,988.474	2,702.039
4	P _{OUT} = 225 psi	4,945.792	2,718.449
5	P _{OUT} = 250 psi	4,893.312	2,734.714
6	P _{OUT} = 275 psi	4,835.977	2,752.391
7	P _{OUT} = 300 psi	4,778.374	2,770.054

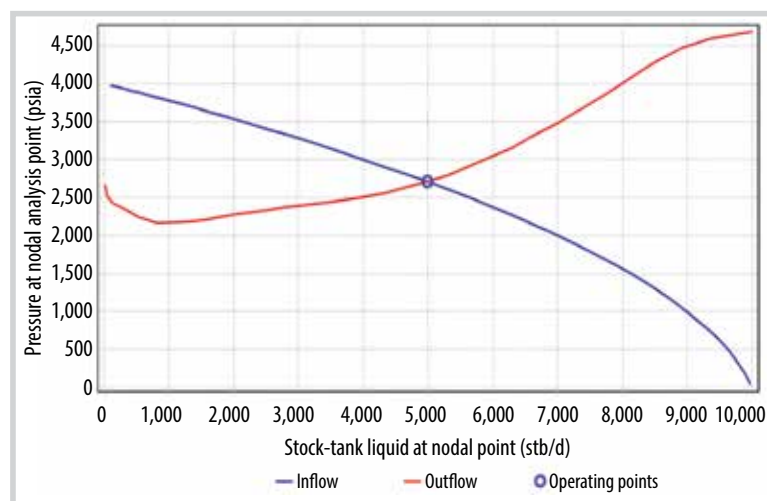


Figure 8. IPR/VLP of the well after optimisation.

Table 7. Production profit

Activation method	Stb/d	Stb/y	Per year (USD)
Electric submersible pump	5,000	1,825,000	1,365,000

Table 8. NPV of the company over a year

CAPEX + OPEX (USD)	Oil benefits for a year	NPV
26,093,750	136,875,000	110,781,250

attained at a pressure of 2,702.5 psi and the effectiveness of the chosen pump is found to be 69%. The pump has a life span of three years, so the well will produce at a constant flow rate of 5,000 stock-tank barrels per day based on the sensitivity curves analysis done for the well.

3.1. Economic evaluation

The production profile of the well activated by electrical submersible pump was obtained by carrying out simulations on the PIPESIM 2017 software, which is the first part, and the second part consists of carrying out an economic evaluation to know the profits the company will get. Capital expenditure (CAPEX) and operation expenditure (OPEX) must be taken into consideration; the income is based only on the oil production; the company pays a 5% income tax per year, and the oil price is USD 75 per barrel. Table 7 shows the profit of production without withdrawal of taxes.

After pulling out the expense and income tables, the business gain during this operation must be known. The net present value (NPV) represents the net money recovered by the company, it is estimated using the formula: NPV = REVENUES - EXPENDITURES. The results are shown in Table 8.

In view of the economic analysis which shows a good NPV value, activating the well is a good choice as it makes it possible to recover a higher rate of hydrocarbons at an average or low cost. In an alternative where oil price increases, the method will still be applicable and remain the best.

3.2. Discussion

When simulating the production of well X, it was noticed that the well no longer produced with a water level of 60%. This led to the installation of a pump at 9,000 ft above the perforations, which allowed the well to produce at a flow rate of 4,891.36 stock-tank barrels per day with a bottom hole pressure of 2,735 psi. The production did not reach

the required flow rate of 5,000 stock-tank barrels per day, this led to the optimisation of the pump using sensitivity curves. After simulating these different sensitivity parameters, the first option was to change the diameter of the tubing, but it is not recommended as it has no great impact on the production rate and also because of the high cost related to the tubing changes. The second option was to increase the number of stages but it put more loads on the engine. Then the next possible option was to reduce the pressure at the wellhead to 200 psi to increase the flow rate to 5,000 stock-tank barrels per day and decrease the pressure drop in the tubing. The economic evaluation carried out after optimisation showed that it was a profitable project. Palen and Goodwin indicated that the optimisation of daily production will increase the production rate by 1 to 4% [18]. Alias had studied optimisation of the production of a well named B in field X in southern Malaysia [19]. This well had a production of 600 stock-tank barrels per day; by reducing the pressure at the wellhead and injecting 2 million standard ft³ per day, it had a production flow rate of 1,040 stock-tank barrels per day, which is a production gain of 73%. The authors of [17] worked on a well which was optimised by using the nodal analysis. They obtained a flow rate of 1,800 barrels per day (previously 800 barrels per day) by decreasing the wellhead pressure from 350 psi to 100 psi and increasing the tubing diameter from 2.5 inches to 2.99 inches. The wellhead pressure is, therefore, an important parameter to consider when optimising a well.

4. Conclusion

This work aims to activate well X in order to improve production by using an electric submersible pump. For this, two approaches were implemented: (i) a technical study allowing the nodal analysis of the well to be carried out using the PIPESIM 2017 software, and (ii) an economic approach to assessing the profitability of the project. The nodal analysis carried out shows that the natural energy of the reservoir is not enough to push up the hydrocarbons from the reservoir to the surface. Thus, the REDA S6000N model pump with a power of 163.93 hp was installed at a depth of 9,000 ft with the aim of reducing the bottom-hole pressure as much as possible but also cooling the latter's engine. The nodal analysis was done again to evaluate the production flow rate after the pump installation (4,891.36 stock-tank barrels per day). Though it is eruptive, the bottom-hole pressure remains high which could end up creating a problem with the operation of the engine in

the long run. So, it will be advantageous to optimise the pump and the well to reduce the pressure at the bottom and produce at an optimal flow rate. This part was done using the nodal analysis based on the sensitivity curves. The study of the sensitivity on the tubing diameter, number of stages of the pump and the pressure at the wellhead reveals that varying the tubing diameter influences less on production, whereas increasing the number of stages increases the production but creates an overload on the engine. Reducing the pressure at the wellhead can help to overcome this problem and make the pump's operation more efficient. These sensitivity tests improved the activated well and gave an optimal production flow rate of 5,000 stock-tank barrels per day and a net present value of USD 110,781,250.

References

- [1] Michael J. Economides and Curtis Boney, "Reservoir stimulation in petroleum production", *Reservoir Stimulation (3rd edition)*. John Wiley & Sons, 2000.
- [2] B. Guo, W.C. Lyons and A. Ghalambor, *Petroleum production engineering: A computer-assisted approach*. Gulf Professional Publishing, 2007. DOI: 10.1016/B978-0-7506-8270-1.X5000-2.
- [3] S. John, *Forecasting oil and gas producing for unconventional wells*, 2nd edition., Petro. Denver, 2018.
- [4] R.S. Seright, "Gel propagation through fractures," *SPE Production & Operations*, Vol. 16, No. 4, pp. 225 - 231, 2001. DOI: 10.2118/74602-PA.
- [5] Lei Zhang, Nasir Khan, and Chunsheng Pu, "A new method of plugging the fracture to enhance oil production for fractured oil reservoir using gel particles and the HPAM/Cr³⁺ system", *Polymers*, Vol. 11, No. 3, 2019. DOI: 10.3390/polym11030446.
- [6] Xiangming Jiang, Guosheng Zheng, Wanghua Sui, Jiaying Chen, and Jinchuan Zhang, "Anisotropic propagation of chemical grouting in fracture network with flowing water", *ACS Omega*, Vol. 6, No. 7, pp. 4672 - 4679, 2021. DOI: 10.1021/acsomega.0c05393.
- [7] Frak Jahn, Mark Cook, and Mark Graham. *Hydrocarbon exploration and production*, 2nd edition. Elsevier Science, 2008.
- [8] Guy Valchon and Terry R. Bussear, "Production optimization in ESP completions with intelligent well technology", *SPE Asia Pacific Oil and Gas Conference*

and Exhibition, Jakarta, Indonesia, 5 - 7 April 2005. DOI: 10.2118/93617-MS.

[9] Abdullah Al Qahtani, Mubarak Al Qahtani, and Balder Al Qahtani, "Development of a novel solution for multiphase flow metering in ESP-lifted wells", *Abu Dhabi International Petroleum Exhibition & Conference, Abu Dhabi, UAE, November 2020*. DOI: 10.2118/203480-MS.

[10] Matthew Amao. "Electrical Submersible Pumping (ESP) Systems", *Artificial Lift Methods and Surface Operations PGE 482, 09 March, 2014*.

[11] Jonathan Bellarby, *Well completion design*, 1st edition. Elsevier, 2009.

[12] G. Takacs, "Evaluation of ten methods used for prediction of pressure drop in oil wells", *Erdöl erdgas kohle*, Vol. 94., No. 4, pp. 146 - 149, 1978.

[13] E. Khamsehchi and M.R. Mahdiani, *Gas allocation optimization methods in artificial gas lift*. Springer, 2017. DOI: 10.1007/978-3-319-51451-2.

[14] A. Davarpanah and B. Mirshekari, "Experimental study and field application of appropriate selective calculation methods in gas lift design", *Petroleum Research*, Vol. 3, No. 3, pp. 239 - 247, 2018. DOI: 10.1016/j.ptlrs.2018.03.005.

[15] M. Amao, "Electrical submersible pumping systems", King Saoud University, 2014.

[16] Schlumberger, "ESP design and technology", 2002.

[17] Total, "Le puits activé par pompage centrifuge immergé", 2007.

[18] W. Palen and A. Goodwin, "Increasing production in a Mature basin: The choke model", *European Petroleum Conference, Milan, Italy, SPE - 36848 - MS, 22 - 24 October 1996*. DOI: 10.2118/36848-MS.

[19] N.B. Alias, "A study of production optimization using prosper", Final year project, Universiti Teknologi Petronas, 2012.

DESIGN OF CONTINUOUS GAS-LIFT FOR A DEAD WELL AND STEP-UP OF ITS PRODUCTIVITY

Josephine Fleur Matateyou^{1,4}, Kasi Njeudjang², Eric Donald Dongmo³, Cherif Ibrahim Rengou Mbouombouo⁴
Hugues Vannela Kamnang Konchipe⁵, Gabriel Kuitse⁵

¹Laboratory of Ore and Mineral Processing, Institute for Geology and Mining Research

²National Advanced School of Mines and Petroleum Industries, University of Maroua

³College of Technology, University of Buea

⁴School of Geology and Mining Engineering, University of Ngaoundéré

⁵African Higher Institute of Managerial and Technological Education

Email: josephine.matateyou@gmail.com

<https://doi.org/10.47800/PVJ.2022.06-05>

Summary

The present paper aims to design a continuous gas-lift system in order to activate the dead well X and optimise the recovery of hydrocarbons by gas injection. The data taken into account are those of the reservoir and the well. All the simulation operations and the well diagram are carried out with the PIPESIM 2017 2.0 software. Moreover, the nodal analysis of the dead well X is carried out by finding the injection pressure of the gas in the well. The number of valves to be installed, the optimal injection heights and the flow rates received by each valve are also included in the gas-lift device. Then the evaluation of the system performance as well as the sensitivity analysis are carried out to make it possible to fix the optimal flow rate of production. The results obtained show that for a continuous gas injection of 3 million standard ft³ per day (MMscf/d) per valve into the well with a wellhead pressure of 2,500 psi and an optimal flow rate of 2,718 standard barrels per day (STB/d), a profitability of USD 182,887,219 is obtained. In this field, this design can be applied to all wells having a production tube of 2.5 inches inside diameter. On the other hand, wells with different diameters will require a new evaluation.

Key words: Non-eruptive well, gas-lift, nodal analysis, PIPESIM software, production optimisation, economic evaluation.

1. Introduction

Crude oil is the most important natural energy source in the world because the modern civilisation and its remarkable achievements would not exist without oil. What makes it so important in our daily lives is its wide variety of uses. Apart from refuelling cars and planes, etc., its components can be used to make many kinds of chemicals such as plastics, drugs, detergents, and many more things [1 - 3].

The exploitation of crude oil contained in the subsoil goes through several stages, namely: prospecting, exploration, development and production [4, 5]. The main factor governing the gas-lift is the availability to reinforce

the pressure if the quantity of gas is high enough. Gas-lift is the most common well activation method, especially in offshore, with the principle of reducing hydrostatic pressure by injecting gas into the well [6, 7]. The gas-lift promotes the optimisation of production when the effluent no longer has enough energy to reach the surface under the conditions set by the process [8 - 10].

The reasons for using gas-lift are multiple, such as cleaning a well (crossover), restarting the well, and lightening the production string [11 - 13]. Two methods are mainly used for the activation of a well: The pumping method and the gas-lift method [14 - 17]. The dead well studied in this article is designated as well X for confidentiality reasons. The field designated as well X has been developed by using 5 wells and reached its peak production in 1997. Since then, production from the oil well has rapidly declined due to an increase in water



Date of receipt: 10/5/2022. Date of review and editing: 10/5 - 16/5/2022.

Date of approval: 27/6/2022.

content. An economic limit of 1,500 barrels of oil has been set. Producing at lower rates is not economical. With regard to the static pressure of the reservoir, the gas-lift method is the most appropriate for well X [6, 18]. Continuous gas-lift is an artificial-lift method that consists of injecting gas through the producing well to lower gravity pressure losses in order to reduce the pressure at the bottom of the well [19]. This gas-lift application is based on several injection and production parameters as well as process modelling to facilitate decision-making. What mainly concerns this article is to optimise the production of the dead well X by the continuous gas-lift activation method. Therefore, finding the optimal gas flow rate to be injected downhole to lighten the hydrostatic column is at the forefront. The aim here is to improve the productivity of the dead well X by determining both the operating parameters of the gas-lift and the production prediction. The paper is sliced into four sections: the first one presents the introduction; the second devotes to the presentation of data; the third highlights the obtained results and the last is for conclusion.

2. Materials and methods

The data used for this study are divided into different categories: pressure-volume-temperature data, well data, reservoir data, gas-lift data, and well test data. Table 1 presents the data of the reservoir, the pressure-volume-temperature (PVT), and the well.

Under current reservoir conditions, it is single-phase as the reservoir pressure is above the bubble point. The main equipment installed is presented in Table 2.

In the study, the nodal and sensitivity analyses are performed by using PIPESIM 2017 2.0 software.

3. Results

This section presents the results of the nodal analysis, the sensitivity analysis and the economic evaluation obtained from the data of the reservoir, the pressure-volume-temperature and the well.

Table 1. Reservoir, pressure-volume-temperature, and well data

Reservoir data		
Parameters	Values	Unit
Pressure	4,200	psi
Temperature	220	°F
Productivity index	1.82	STB/day/psi
Pressure - volume-temperature data		
Temperature	109	°F
Bubble pressure	4,080	psi
Bubble temperature	197	°F
Formation volume factor (FVF)	1.87	Rb/STB
Well data		
API density	42.30	°API
Gas specific gravity	0.84	-
Gas oil ratio (GOR)	1,577	SCF/STB
Water cut	89.50	%
Specific gravity of water	1.20	-

Table 2. Well equipment data

Equipment	Depth (ft)	
Christmas tree	0	
Casing	Conductor pipe	1,000
	Surface casing	5,000
	Intermediate casing	9,000
	Production casing	11,306
Tubing	11,000	
Packer	10,597	
Perforation	11,165	

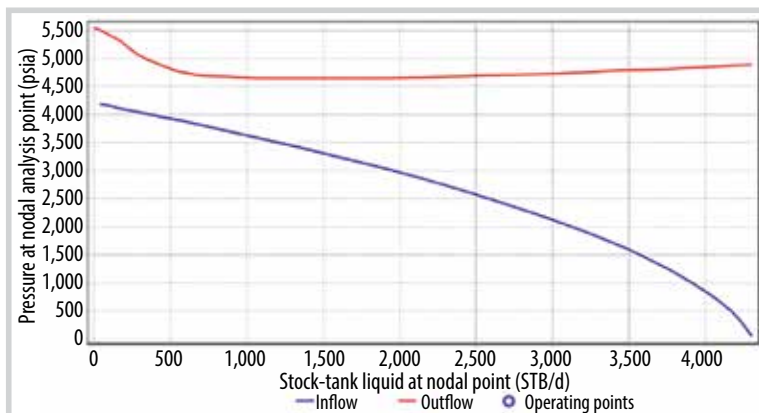


Figure 1. Nodal analysis of the non-eruptive well X.

Table 3. Optimal flow with different gas injection rates per day

Case	Casing head pressure (psi)	Qgi (MMscf/d)	QI (STB/d)	DIP (ft)
1	2,500	1	2,107.69	10,589.82
2	2,500	2	2,441.22	10,589.82
3	2,500	3	2,550.61	10,589.82
4	2,500	4	2,604.14	10,589.82
5	2,500	5	2,634.80	10,589.82
6	2,500	6	2,650.82	10,589.82
7	2,500	7	2,656.61	10,589.82
8	2,500	8	2,654.54	10,589.82

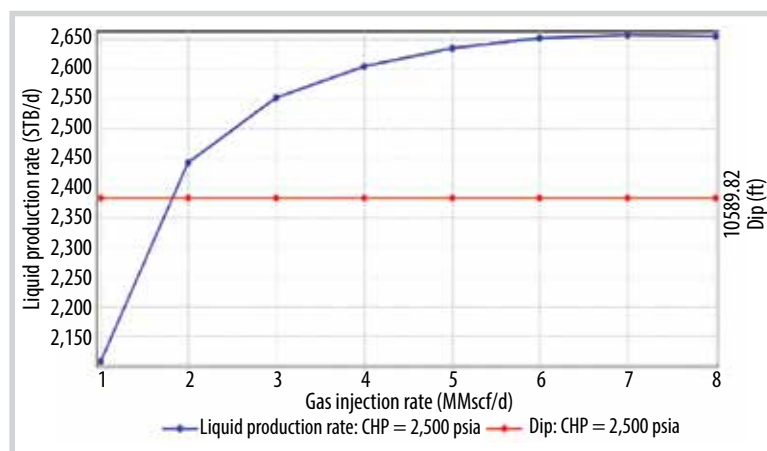


Figure 2. Gas-lift performance curve.

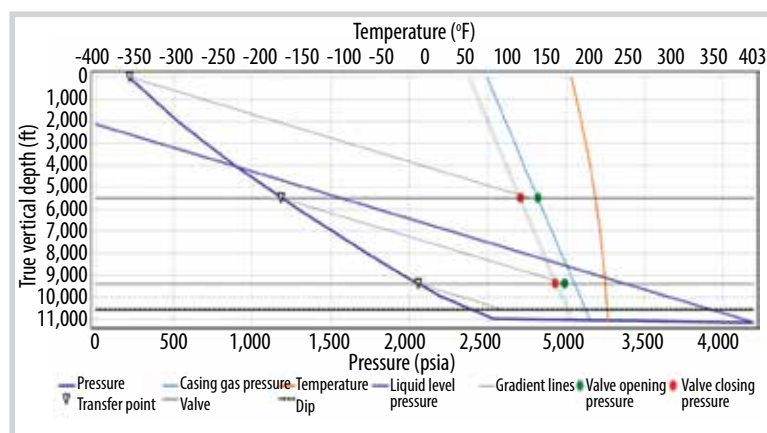


Figure 3. Shaft gas lift design.

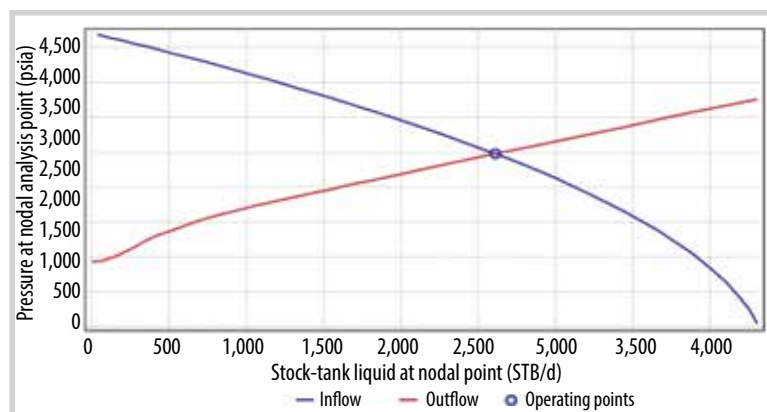


Figure 4. Diagnosis of gas-lift.

Table 4. Comparison of oil flow rates before and after completion

Before completion		After completion	
Oil flow	P _{wf}	Oil flow	P _{wf}
0 STB/d	4,200 psi	1,400 STB/d	3,163 psi

Table 5. Results of the pressure variation at the wellhead

Wellhead pressure (psi)	Downhole pressure (psi)	Q (STB/d)
50	2,329	2,776
150	2,687	2,687
350	2,474	2,474

3.1. Nodal and sensitivity analyses

Figure 1 shows the evolution of the inflow performance relationship (IPR) and vertical lift performance relationship (VPR) curves of the studied well X.

Figure 1 shows that the operating point does not exist. The well has lost all its natural energy with regard to the distancing of the curves. This reflects the non-eruptive nature of well X and, hence, the need to activate this well by the gas-lift method to make it a producer again. The development of a gas-lift passes through the stages established in [20]. The gas-lift response generates the maximum depth of gas injection into the production tube, and the maximum gas flow necessary to produce maximum oil at the surface. The variation in flow rates and the gas-lift performance curve are shown in Table 3 and Figure 2, respectively.

In Figure 2, the result of the simulations of the response of the well to a gas injection calculates the maximum gas injection pressure casinghead pressure (CHP) = 2,500 psi, and gives the maximum injection depth of 10,590 ft and an optimal injection rate of 3 million standard ft³ per day (MMscf/d). Table 3 gives a summary of the scenarios carried out for up to eight cases. The optimum gas injection point in the well is calculated according to the height, the pressure, the temperature, and the absolute open flow of the well at the moment when the pressure at the well bottom is higher than tank pressure as shown in Figure 3.

Figure 3, in addition to the first valve placed at 10,590 ft, two other valves will be placed above it to maximise production at the respective depths of 9,402 ft and 5,488 ft. With the installation of the new gas-lift equipment in well X, a depression in the well can therefore be created, until the pressure in the reservoir again becomes higher than the pressure recorded at the bottom of the well. From this moment, well X will be able to deliver a manageable oil flow to the surface. Gas-lift performance results are shown in Figure 4 and Table 4, respectively.

In Figure 4, the meeting point of the IPR/VLP curves gives, after installation of the gas-lift device, a production pressure at the bottom of the well of 2,500 psi for an approximate flow rate of 2,600 standard barrels per day (STB/d). This aspect follows a pattern similar to that of the study [21] on optimisation using smart pump gas-lifts. In Table 4, the production rate does not correspond to that desired by the company, which is 2,600 standard barrels per day, hence it is necessary to optimise this well using sensitivity analyses.

The fluid outlet pressure at the wellhead and the gas injection rate will be analysed. Reservoir pressure is the key to ensuring reservoir production [6]. When a well is put into production, the flow gradually drops with the pressure. The wellhead pressure sensitivity analysis yielded the results summarised in Table 5.

Oil production increases when wellhead pressure drops. Figure 6 presents the results of well performance as a function of wellhead pressure.

In Figure 5, the curves are obtained for the wellhead pressures of 50, 150 and 350 psi respectively for flow rates of 2,776, 2,687 and 2,474 standard barrels per day. Figure 6 and Table 6 show the results of the gas injection rate sensitivity analysis.

When the injection rate increases, so does the production rate. Thus, it is wise to increase the injection rate at the surface in order to optimise production. Table 7 and Figure 7 illustrate the optimum values and the optimum productivity curve, respectively.

3.2. Economic evaluation

The optimisation of well X activated by gas-lift (gas injection rate of 3 million standard ft³ per day) makes it possible to produce at a constant rate for 3 years with a continuous injection of gas, hence it is necessary to make an economic evaluation to know the profitability of this method. The parameters to be taken into consideration are the following: expenses, income and profit. Expenditures are

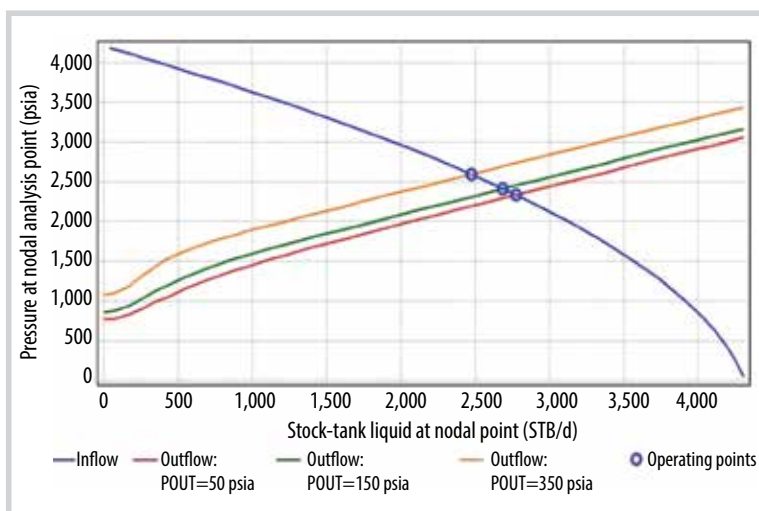


Figure 5. Operating point as a function of wellhead pressure.

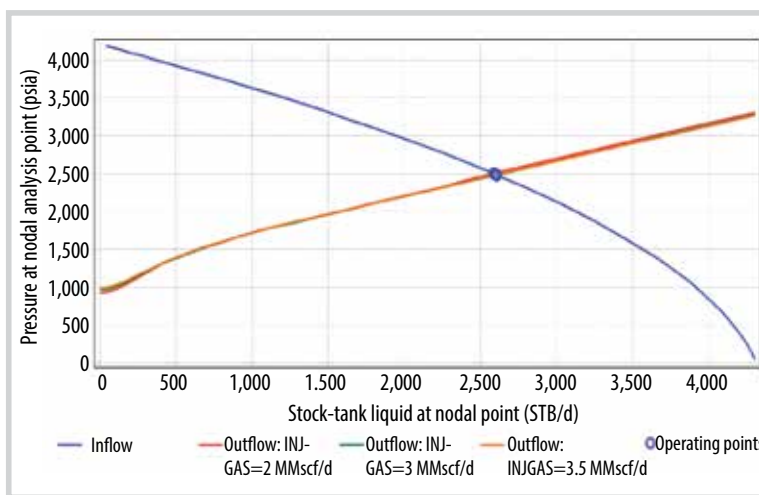


Figure 6. Gas injection rate sensitivity.

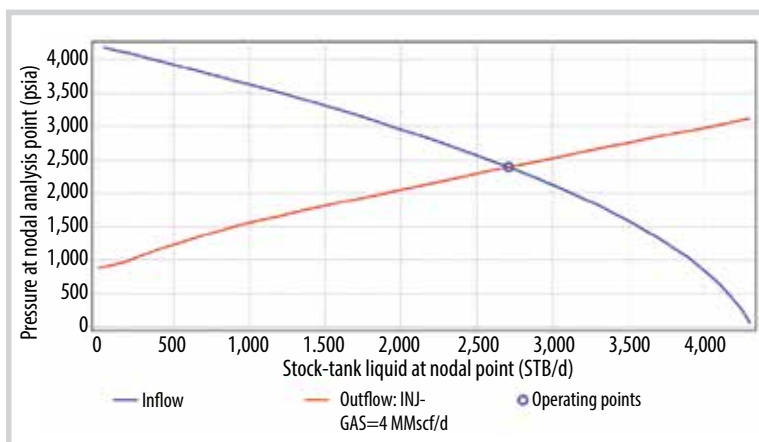


Figure 7. Optimal production curve.

Table 6. Gas injection rate sensitivity results

Gas injection rate (MMscf/d)	Oil flow (STB/d)
1	2,420
2	2,570
3	2,600

Table 7. Optimal parameters

Parameters	Values
Pressure (psi)	100
Injection rate (MMscf/d)	3
Optimal diameter (inch)	2.5
Optimal flow (STB/d)	2,718

Table 8. Capital expenditure (CAPEX) and operation expenditure (OPEX)

Parameters	Price in (USD)	Quantity	Total (USD)
Equipment	50,000	1	50,000
Installation	20,000	1	20,000
Taxes	0.15	2,976,210	446,431.5
Water treatment	350,000	3	1,050,000
Service	300,000	6	1,800,000
Price per barrel	10	2,976,210	29,762,100
Cunning cost/2	1,200,000	6	7,200,000
TOTAL			40,328,531.5

a function of capital expenditure (CAPEX) and operation expenditure (OPEX) shown in Table 8.

In Table 8, the revenues amount to USD 223,215,750, which is mainly based on oil production for a net present value (NPV) of USD 182,887,219. At the end of this economic assessment, it appears that the gas-lift activation method is appropriate, because in addition to the fact that it optimises production, it is still profitable. The gas-lift method is more economically advantageous because it is economically profitable by producing 2,718 barrels per day.

4. Conclusion

This paper proposed a design of a continuous gas-lift system, allowing activating and optimising the production of hydrocarbons from a non-eruptive well, while injecting as little gas as possible into the production column. The reservoir, pressure-volume-temperature and well data were used and their importance was clearly perceptible. Also, in order to achieve the defined objectives, an appropriate methodology was developed. The first step was to define and present the data used. The second step was to present a nodal analysis and sensitivity analysis of the non-productive well and the third step was to make an economic evaluation. The gas-lift design facilitated optimal surface oil recovery and a sensitivity analysis helped to optimise surface production. Finally, an economic analysis was developed to determine the profitability of the project. In view of these procedures, it appeared that the nodal analysis of the well before the installation of the gas-lift showed an absolute open flow of 46.7 standard barrel per day. The design of the gas-lift for injecting gas into the well allowed for an injection pressure of 2,500 psi for each valve and a maximum height of the first gas valve set at 10,159 ft. For better recovery of hydrocarbons on the surface, two relay valves must be placed at the respective depths of 9,402 ft and 5,488 ft and the daily injection rate

was 3 million standard cubic feet per day for an available gas quantity of 4 million standard ft³ per day. An outlet pressure of 100 psi suggested the optimum production flow rate recorded at 2,718 standard barrels per day. The economic analysis revealed a gross profit of USD 182,887,219 after 3 years.

References

[1] Chang Samuel Hsu and Paul R. Robinson, *Petroleum science and technology*, 1st edition. Springer, 2019. DOI: 10.1007/978-3-030-16275-7.

[2] Boyun Guo, William C. Lyons, and Ali Ghalambor, *Petroleum Production Engineering: A computer-assisted approach*. Gulf Professional Publishing, 2007. DOI: 10.1016/B978-0-7506-8270-1.X5000-2.

[3] S. John, *Forecasting oil and gas producing for unconventional wells*, 2nd edition, Petro. Denver, 2018.

[4] Michael J. Economides and Curtis Boney, "Reservoir stimulation in petroleum production", *Reservoir Stimulation*, 3rd edition. John Wiley & Sons, 2000.

[5] Frank Jahn, Mark Cook, and Mark Graham. *Hydrocarbon exploration and production*, Vol. 55, 2nd edition. Elsevier Science, 2008.

[6] Jonathan Bellarby, "Artificial lift", *Well completion design*, 1st edition. Elsevier Science, 2009.

[7] Saurabh Goswami and Tej Singh Chouhan, "Artificial lift to boost oil production", *International Journal of Engineering Trends and Technology*, Vol. 26, No. 1, 2015. DOI:10.14445/22315381/IJETT-V26P201.

[8] Alan Brodie, Joe Allan, and Atholl Campbell, "Gas-lift well design", Petroleum Technology Company, 2015.

[9] Shahab Ayatollahi, A. Bahadori, and A. Moshfeghian, "Method optimizes Aghajari oil field gas lift", *Oil and Gas Journal*, Vol. 99, No. 21, pp. 47 - 49, 2001.

[10] Ehsan Khomehchi and Mohammad

Reza Mahdiani, *Gas allocation optimization methods in artificial gas-lift, 1st edition*. Springer Briefs in Petroleum Geoscience & Engineering, 2017.

[11] Ali A. Garrouch, Mohammad Al-Dousari, and Zahra Al-Sarraf, "A pragmatic approach for optimizing gas lift operations", *Journal of Petroleum Exploration and Production Technology*, Vol. 10, pp. 197 - 216, 2019. DOI: 10.1007/s13202-019-0733-7.

[12] Asekhame U. Yadua, Kazeem A. Lawal, Stella I. Eytayo, Oluchikwu M. Okoh, Chinyere C. Obi, and Saka Matemilola, "Performance of a gas-lifted oil production well at steady state", *Journal of Petroleum Exploration and Production Technology*, Vol. 11, pp. 2805 - 2821, 2021.

[13] Mohamed A. H. Elgadban Abdalsadig, Amir Nourian, Ghasem Ghavami Nasr, and Meisam Babaie, "Gas lift optimization using smart gas lift valve", *International Journal of Mechanical and Mechatronics Engineering*, Vol. 10, No. 6, pp. 1162 - 1167, 2016. DOI: 10.5281/zenodo.1125185.

[14] Guy Vachon and Terry Bussear, "Production optimization in ESP completion with intelligent well technology", *SPE Asia Pacific Oil and Gas Conference and Exhibition, Jakarta, Indonesia, 5 - 7 April 2005*. DOI: 10.2118/93617-MS.

[15] Gabor Takacs, "A critical comparison of TDH

calculation models in manual ESP design procedures", *Journal of Petroleum Science and Engineering*, 2020, DOI:10.1016/j.petrol.2020.108210.

[16] Gabor Takacs, "Evaluation of ten methods used for prediction of pressure drop in oil wells", *Oil Gas European Magazine*, Vol. 2, pp. 44 - 51, 1983.

[17] Abdel BenAmara, "Gas lift - past & future", *SPE Middle East Artificial Lift Conference and Exhibition, Manama, Kingdom of Bahrain, 30 November - 1 December 2016*. DOI: 10.2118/184221-MS.

[18] Fathi Elldakli, "Gas lift system", *Petroleum & Petrochemical Engineering Journal*, Vol. 1, No. 4, pp. 1 - 11, 2017.

[19] Ali Hernandez, *Fundamentals of gas lift engineering: Well design and troubleshooting*, 1st edition. Gulf Professional Publishing, 2016.

[20] E.N. Magdi, "Artificial lift technology, Dubai: advancing performance excellence, 2017.

[21] Badr A. Mohamed, Naoko Ellis, Chang Soo Kim, Xiaotao Bi, and Ahmed El-raie Emam, "Engineered biochar from microwave-assisted catalytic pyrolysis of switchgrass for increasing water-holding capacity and fertility of sandy soil", *Science of the Total Environment*, Vol. 566 - 567, pp. 387 - 397, 2016. DOI: 10.1016/j.scitotenv.2016.04.169.

ASSESSING THE EFFECT OF GAS TEMPERATURE ON GAS WELL PERFORMANCE

Nguyen Thanh Phu^{1,2}, Nguyen Van Hoanh³, Ta Quoc Dung^{1,2}, Le The Ha⁴

¹Faculty of Geology and Petroleum, Ho Chi Minh City University of Technology (HCMUT)

²Vietnam National University

³Cuu Long JOC

⁴Petrovietnam

Email: tqdung@hcmut.edu.vn

<https://doi.org/10.47800/PVJ.2022.06-06>

Summary

Gas temperature is an essential parameter in estimating production rate and pressure model inside the production tubing. Three heat transfer mechanisms named as conduction, convection and radiation have been applied to identify the gas temperature declination. Gas wells with bottom hole temperature greater than 160°C and gas rates reaching 55 million standard ft³ per day (MMscf/d) indicate a higher heat loss due to convection than the other two mechanisms. Conduction is the main factor in explaining heat diffusion to the surrounding at the top of the well. The study presents a strong similarity in value compared to the field data by combining Gray correlation and heat transfer model to predict the bottom hole pressure with an error of approximately 3%. Additionally, the gas temperature affects gas rate prediction through gas viscosity and Z factor. With the gas composition mostly containing C1 (70.5%), gas viscosity and Z coefficient at the wellhead are not as high as 0.017 cp and 0.92 respectively. It is possible to have a two-phase flow, then a temperature model along the production tubing is necessary to ensure the gas production rate.

Key words: Heat transfer mechanism, Gray correlation, gas production rate.

1. Introduction

Measurement of wellhead fluid temperature in the surface is often unreliable as they can be influenced by errors in the measurement procedure and by daily and seasonal temperature variations [1]. In particular, tubing steel is a very good conductor of heat, and variations in temperature of the surface equipment can greatly impact the wellhead temperature [2]. That is why the wellhead temperature must be developed by temperature profile along the tubing.

Gas production inevitably involves significant heat exchange between the wellbore and its surroundings. The presence of seawater and air adds complexity to the heat transfer process in an offshore environment. During production, hot gas continues to lose heat due to cold ambient temperature when it flows inside the borehole [3]. Following the idea of calculating the temperature

profile, this paper presents the simple stepwise calculation procedure for gas temperature profile in wellbore. The temperature loss affects the flow rate prediction and pressure profile in the production tubing. The value of gas physical qualities that determine the result of tubing pressure is evident in temperature data. If the understanding of heat transfer is better, the accuracy in predicting the pressure or gas flow rate will be higher.

2. Methodology

2.1. Heat transfer in wellbore

Heat transfer occurs between the fluid in wellbore and the formation, however, there are some heat resistances of the tubing wall, tubing insulation, tubing-casing annulus, casing wall, and cement. From that view, the temperature distribution in wellbore is dependent on the well structure and geological conditions of the surrounding formation. Heat transfer in a wellbore is governed by three main mechanisms: conduction, convection, and radiation. Conduction and convection are the most reliable technique of exchanging heat from



Date of receipt: 27/9/2021. Date of review and editing: 27/9 - 22/11/2021.

Date of approval: 27/6/2022.

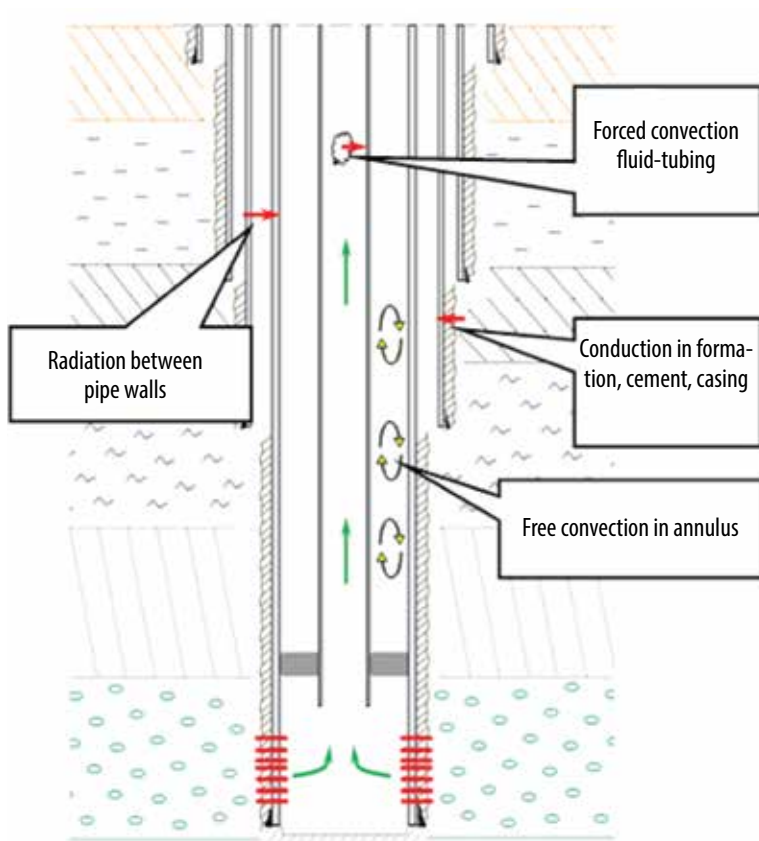


Figure 1. Three heat mechanisms occur along the production tubing [4].

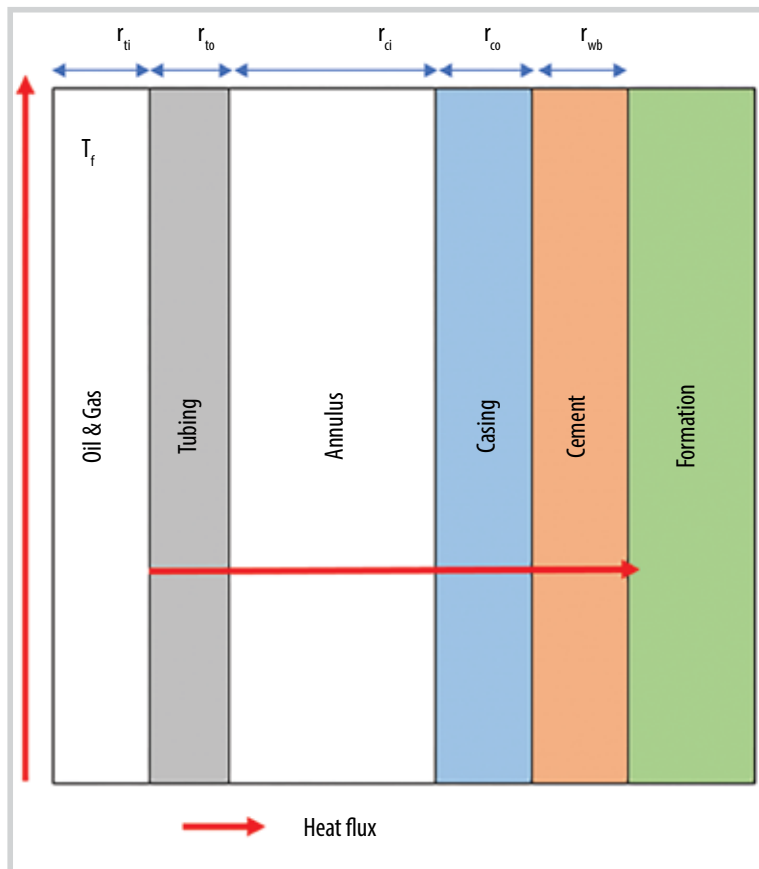


Figure 2. Structure of heat transfer model for wellbore without insulation [5].

a gas flow in a production tubing. Although radiation has little effect on heat loss, it must be included to ensure the model's validity.

In this research, a basic well model is assumed firstly to calculate the overall heat transfer in the absence of insulation. Six zones were considered from the centre of wellbore to formation as shown in Figure 2. The production fluid zone is located inside the tubing and the surrounding is the wellbore region.

T_f : Fluid temperature (°C or °F)

r_{ti} : Inner tubing radius (inch)

r_{to} : Outer tubing radius (inch)

r_{ci} : Inner casing radius (inch)

r_{co} : Outer casing radius (inch)

r_{wb} : Wellbore radius (inch)

2.2. Conduction

It illustrates the transfer of heat between neighbouring regions of production tubing by solid material. In principle, the hotter material will transfer the heat to the less ones. In this understanding, the heat is transferred in horizontal direction through tubing, casing to formation.

The rate at which conduction occurs, ΔQ_1 , is dependent on the geometry of the grain (formation), thermal conductivity of the material, and the temperature thermal gradient.

$$\Delta Q_1 = 2\pi \cdot k \cdot \Delta L \frac{T_{casing} - T_{formation}}{\ln\left(\frac{r_{wb}}{r_{co}}\right)} \quad (1)$$

$$k = k_{gas} \cdot (1 - H_L) + k_L \cdot H_L \quad (2)$$

where:

ΔQ_1 : Heat transfer by conduction (British thermal unit/hr - BTU/hr) 1 BTU/hr ~ 1 KJ/hr

k: Average conductivity

H_L : Holdup liquid (if there is no liquid phase let $H_L = 0$)

r_{wb} : Wellbore radius (inch)

r_{co} : Outer casing diameter (inch)

T_{casing} : Casing temperature (°F)

Table 1. Conductivity (*k*) and specific heat of fluid [4]

Fluid type	Specific heat of fluid (BTU/lb/°F)	Conductivity (BTU/hr/ft/°F)
Water (low salinity)	1	0.35
Water (high salinity)	1.02	0.345
Heavy oil	1.04	0.34
Medium oil	0.49	0.089
Light oil	0.5	0.0815
Gas	0.26	0.0215

$T_{formation}$: Tubing temperature (°F)

Table 1 summarises the typical values of conductivity and specific heat of fluid for different fluid types.

2.3. Convection

The transfer of heat of gas flow is named convection. Convection occurs through the combination of conduction and fluid motion. There are two typical convections: forced convection in tubing and free convection in annulus.

Natural or free convection exists when there is a change in temperature from the bottom to the wellhead. Forced convection appears by artificially forcing gas to flow over the surface subjected to any external operation units.

The rate of convection, ΔQ_2 , increases at an increasing rate in case the fluid-motion exists.

The rate of heat flux by free convection is:

$$\Delta Q_{2forced} = 2\pi \cdot r_2 \cdot h_f \cdot \Delta L \cdot (T_2 - T_1) \quad (3)$$

$$h_f = \frac{0.023 \cdot k \cdot R_{en}^{0.8} \cdot P_r^{1/3}}{r_{ti}} \quad (4)$$

where:

ΔQ_2 : Heat transfer by convection (BTU/hr)

T_1 : Temperature at upper segment in production tubing (°F)

T_2 : Temperature at lower segment in production tubing (°F)

μ : Gas viscosity (cp)

r_{ti} : Inner tubing radius (inch)

ΔL : Different in tubing length (ft)

R_{en} : Reynolds number

P_r : Prandtl number

$$P_r = \frac{C_p \mu}{k} \quad (5)$$

$$C_{pavg} = C_{pgas}(1 - H_L) + C_{pfluid}(H_L) \quad (6)$$

where:

C_{pavg} : Average specific heat of mixture (BTU/lb/°F)

C_{pg} : Average specific heat of gas (BTU/lb/°F)

C_{pfluid} : Average specific heat of liquid (BTU/lb/°F)

H_L : Holdup liquid

The specific heat of fluid value can be looked up from Table 1.

The rate of heat flux by free convection is:

$$\Delta Q_{2free} = 2\pi r_{ti} h_c \Delta L (T_2 - T_1) \quad (7)$$

$$h_c = \frac{0.049 (G_y P_r)^{1/3} P_r^{0.0074} k}{r_{to} \ln \left(\frac{r_{ci}}{r_{to}} \right)} \quad (8)$$

where:

r_{to} : Outer tubing radius (inch)

r_{ci} : Inner casing radius (inch)

G_y : Grashof number is:

$$G_y = \frac{\beta \cdot g \cdot (T_2 - T_1) \cdot r_2^3}{\mu^2} \quad (9)$$

where:

β : The coefficient of thermal expansion

The total heat by convection is:

$$\Delta Q_2 = \Delta Q_{2forced} + \Delta Q_{2free} \quad (10)$$

2.4. Radiation

The gas flow which has a high temperature emits heat to the production tubing and gas component significantly evaporates under high temperature. Each gas component has its own boiling temperature, if the temperature is higher than that boiling temperature, the component will evaporate leading to reduction in the heat of fluid. That mechanism is called radiation and it co-occurs with either conduction or convection. In most cases, radiation appears in pipe wall areas:

$$h_r = \frac{\sigma \cdot (T_2^2 - T_1^2) \cdot (T_2 + T_1)}{\frac{1}{\varepsilon + \frac{r_1}{r_2} \cdot \left(\frac{1}{\varepsilon} - 1 \right)}} \quad (11)$$

where:

ε : Tubing emissivity

σ : Stefan-Boltzmann constant, approximately $5.67 \times 10^{-8} (W \cdot m^{-2} \cdot K^4)$

Table 2. General tubing emissivity [4]

Mild steel tubing	ϵ
Plastic coated tubing	0.65
Stainless steel (13%)	0.65
Stainless steel (15%)	0.4
Line pipe	0.3

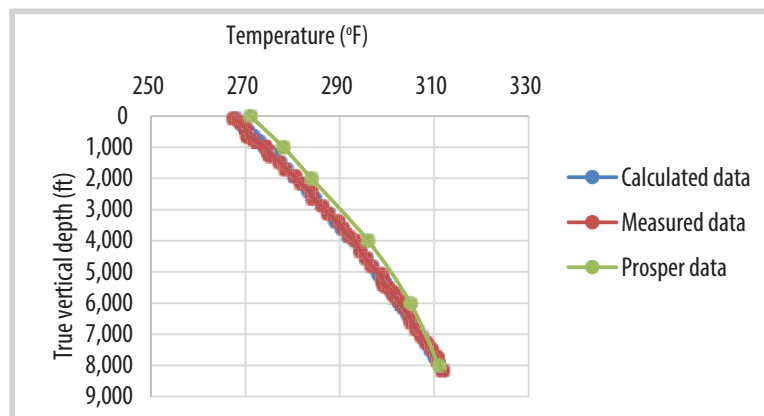


Figure 3. Temperature loss from 0 - 8,100 ft. Calculated data has been matched with measured data.

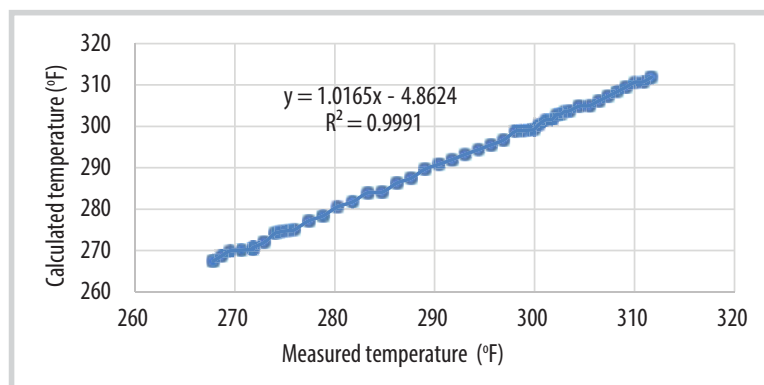


Figure 4. Temperature data comparison inside tubing with depth: 0 - 8,100 ft.

Table 2 provides values of the conduction heat transfer coefficient and the emissivity for different types of tubing material.

Total heat loss by depth:

$$\Delta T = \frac{\sum \Delta Q}{U \cdot \Delta D^2} = \frac{\Delta Q_1 + \Delta Q_3}{U \cdot \Delta D^2} \quad (12)$$

where:

ΔD : Difference in depth (ft)

ΔT : Temperature decrease when flowing up (°F)

U : Overall heat transfer coefficient

$$U = \frac{1}{h_f} + \frac{1}{h_c} + \frac{1}{h_r} \quad (13)$$

To check the value of U , by the experience U value should be in:

- Dry Gas: 1 - 3 BTU/(hr.ft².°F)

- Retrograde condensate fluid: 5 - 7 BTU/(hr.ft².°F)

- Oil: 8 - 9 BTU/(hr.ft².°F)

2.5. Gray correlation in calculating gas well performance

The investigation of the relation between gas production rate and bottom hole pressure is described as gas well performance. Gray correlation is applied to build the pressure profile along the production tubing. In Gray correlation, it can be applied for high-rate condensate gas ratio (more than 50 barrels per million standard ft³) and large tubing inside diameter (3.5 or 4.5 inches) [6].

The total pressure loss is demonstrated in Equation (14). There are three factors affecting the pressure change: friction force, potential and kinetic energy [7]. If the tubing is divided into small segments, then the pressure loss by kinetic energy is not considerable.

$$\frac{dP}{dZ} = \frac{f \cdot p_n \cdot v_m^2}{2 \cdot (r_1 + r_2)} + \frac{g_c}{g} \rho_s \cdot \sin \theta \quad (14)$$

where:

f : Friction factor number

v_m : Mixture velocity (ft/s)

ρ_n : Mixture average density of liquid and gas phase (lbm/ft³)

ρ_s : Slip mixture density of liquid and gas phase (lbm/ft³)

θ : Well deviation angle (degree)

3. Implementation

3.1. Well information

The gas well X1 is located in a reservoir with a high pressure of 7,500 psi and a massive temperature of 322°F (around 168°C).

The stainless steel was designed to evaluate the heat transfer in the production tubing for the gas well. The well produces single gas phase at sand layer where the geothermal gradient is 0.015°F. The surrounding temperature is measured which shows a slow effect on the fluid temperature due to the strong thermal insulation.

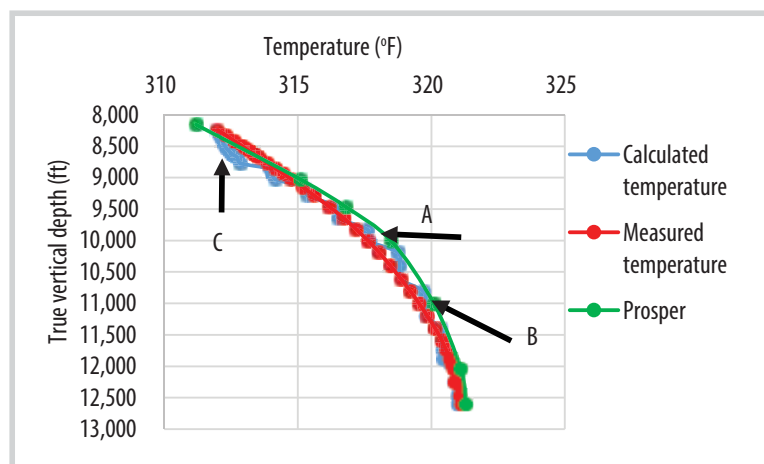


Figure 5. Temperature loss from 8,100 ft - bottom hole. Calculated data has been matched with measured data.

Table 3. The difference of three values

Temperature data	Measured data (°F)	Calculated data (°F)
Point A at 10,190 ft	318.038	318.751
Point B at 11,994 ft	320.81	320.82
Point C at 8,942 ft	314.474	314.058

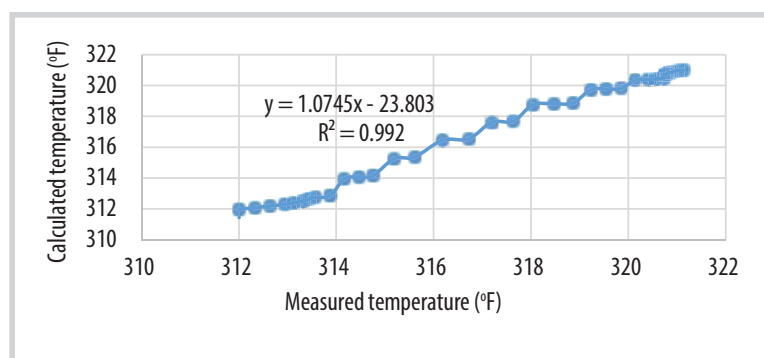


Figure 6. Temperature data comparison inside tubing with depth: 8,100 ft - bottom hole.

3.2. Heat transfer in well bore and surrounding temperature

The well depth is 13,419 ft long (measured depth - MD), and 12,731 ft long (true vertical depth - TVD). The well has been split into two parts: from surface, 0 - 8,100 ft. The other is from 8,100 ft to bottom hole.

It can be seen from Figure 3, along the tubing, the calculated temperature from three heat transfer mechanisms has been matched with the measured data. The Prosper data has given a slight equal to the calculated data. The $R^2 = 0.9991$ from Figure 4 shows the similarity of measured and calculated temperature data.

At the near surface region, different layers of wellbore component have been installed such as surface casing, cement and annulus. There is a lack of tubing equipment in the surface region, so that the heat loss is mainly by conduction. Tubing equipment plays as a heat insulation that prevents the production heat flux transfer to

the surrounding area. It can be seen that the conduction mechanism response for the high heat loss as a shortage of heat insulation in top section of the well. Heat transfers from inside tubing to casing and formation.

At the lower section, the calculated temperature data fluctuates with the measured data. At bottom hole, it records a high flow rate and a high temperature. High temperatures tend to transfer heat faster, the convection appears regularly. From the well structure, at bottom hole there are various equipment such as safety valve or gauge. It absorbs the heat release. There are reasons explaining why the heat transfer 's value cannot be incorrect. There are three points which are used to give some view about the value (Table 3).

The difference between data of three points is not considerable. With $R^2 = 0.992$, which is shown in Figure 6, it can be concluded that the model is correct when compared with the measured data.

To summarise, the temperature change near the surface has shown a perfect match with the measured data, and there is some variation in value when moving down to the bottom hole. A few remarks have been made about the temperature profile in production tubing:

- In production tubing, the heat from bottom hole condition is dispersed in two directions: moving up to low temperature area at the wellhead and transferring to the surrounding environment. Convection is the main mechanism which causes the high drop in flow 's temperature at bottom hole.

- The flow is not in steady state. The flow rate increases in value and becomes stable when reaching the surface. That can explain why at the near bottom hole region, the calculated temperature data has some differences.

- There is an equipment installed along the below tubing which is to control flow rate and pressure. By adding with elevation,

a decrease in temperature is a contributing factor to ensure the prediction accuracy.

- Temperature profile at surrounding environment.

The heat transfer in wellbore has been simplified in three types of temperature:

T_g : temperature of produced gas.

T_{ci} : Temperature inside casing: measured by heat transfer from the production tubing through the annulus to the inner casing region.

T_{co} : Temperature outside casing: the heat transfer from inside to outside casing by the conduction heat mechanism.

The test used 9 5/8" casing for analysing. This casing has been installed from the top to 10,000 ft of true vertical depth. It is the nearest region casing from the production tubing. Inside the casing is a free space – annulus, and the outside is cementing layer. The casing material is steel, which is a good heat conductor. This is a reason why the temperature difference between inside and outside casing is not considerable (Figure 7).

As a result, the temperature of fluid is the highest as it is calculated by the bottom hole temperature which is equal to the formation temperature. Next the heat transfers outside through the annulus and casing in horizontal direction and lowers the value.

3.3. Temperature effect on gas viscosity and Z factor

The equation for viscosity analysis is from Gray correlation, which takes account of the temperature change along the production tubing. In this section, the gas viscosity curve named general temperature model illustrates the value of gas viscosity when gas temperature reduces by three heat transfer mechanisms. Another method in calculating gas viscosity is the linear decrease of temperature profile in tubing.

At low temperature, the gas becomes cooler and reduces its viscosity. The viscosity

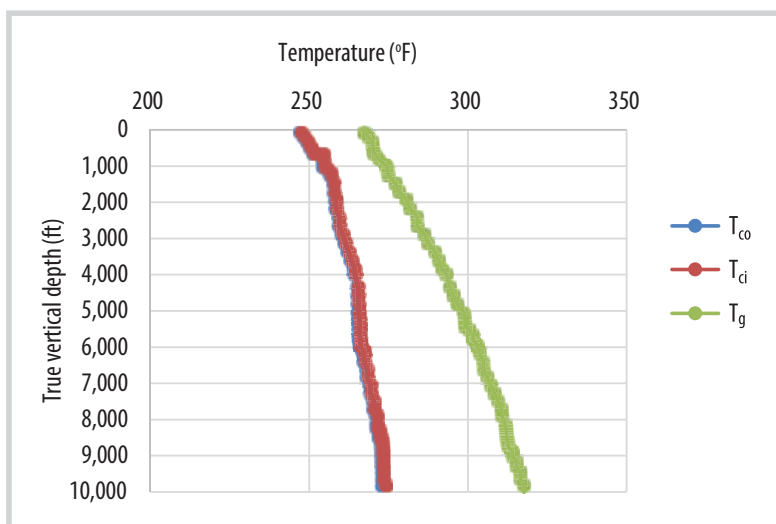


Figure 7. Heat transfer from tubing to casing.

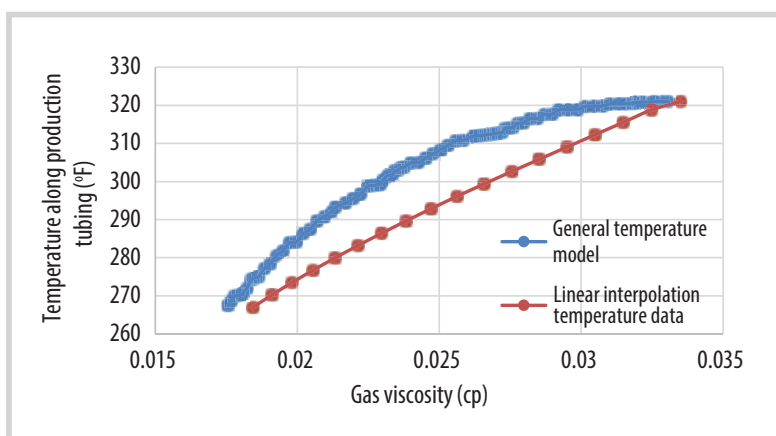


Figure 8. Gas viscosity analysis.

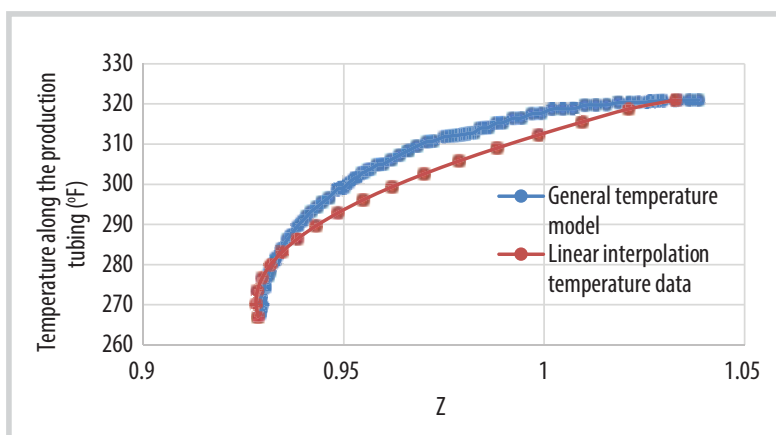


Figure 9. Z factor analysis.

at bottom hole shows the same value, 0.047 cp. It has a small different value in the well head between two temperature models, 0.017 and 0.018 cp, respectively. The gap between two curves in Figure 8 represents the actual change in gas viscosity inside the production tubing. When using linear interpolation temperature data, it highlights the mistake in generating the phase diagram or predicting the actual flow rate.

It is claimed that the temperature of the gas influences the change of the Z factor, and that the Z factor influences the pressure calculation and gas flow rate capability.

The method uses a pseudo temperature to find the value of Z by using the Beggs and Brill correlation in measuring the Z factor. The Z factor curve relating to the linear interpolation of temperature in bottom hole pressure prediction is virtually identical to the curve that is considered the temperature model.

The Z factor calculated in the well head gives the closest in value to the two curves at the bottom hole, 0.929 and 0.928. However, along the production tubing, there is a difference in value of Z factor as it considers the temperature drop in constant value. This will reveal the pressure profile calculation mistake.

3.4. Temperature effect on the pressure profile in production tubing

In a flowing fluid, one of the most critical values is pressure. If there is a pressure differential between the bottom hole and the well head (BHP > WHP), the fluid can flow. The pressure change in the production tubing is slightly affected by temperature. However, the temperature model alters the Z, viscosity, and other properties, all of which have an impact on the pressure value.

The Gray correlation is used to apply the pressure gradient. As a result, the pressure determined using the applied general temperature model has a high degree of accuracy when compared to the measured data.

The analysis used the same temperature profile value. As the difference in temperature at the top section is not considerable, the pressure profile applying the temperature drop in linear value is identical.

Between estimated and measured results, linear regression has been investigated. The R² value is 0.998. It is similar to the value of one. As a response, the pressure model has been

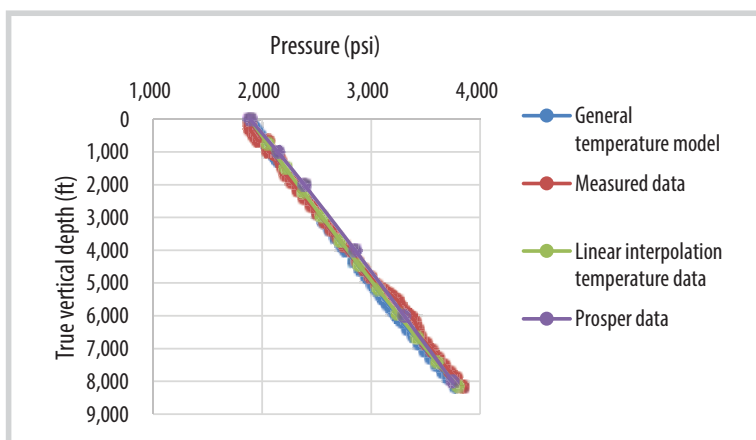


Figure 10. Pressure changes from surface - 8,100 ft of true vertical depth along production tubing.

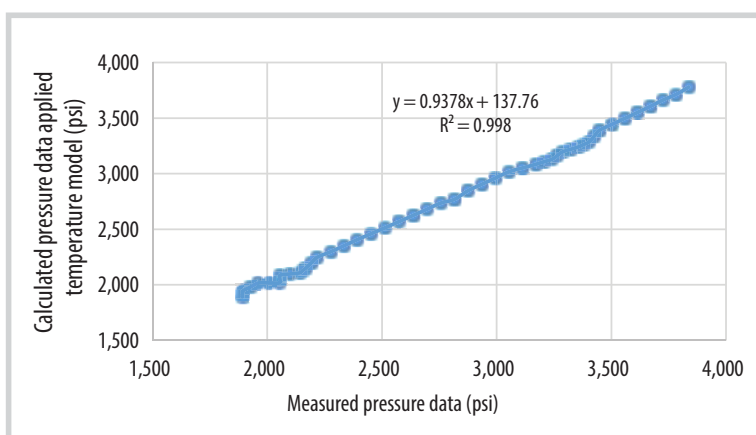


Figure 11. Data comparison of pressure in tubing from surface - 8,100 ft of true vertical depth.

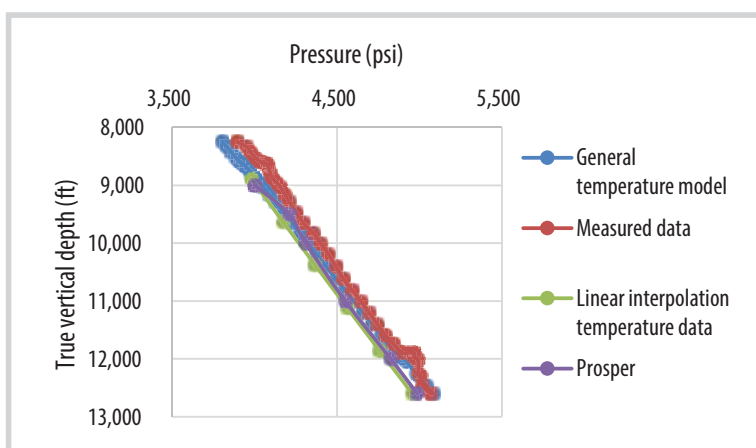


Figure 12. Pressure changes from 8,100 ft - bottom hole along production tubing. Pressure changes from 8,100 ft - bottom hole along production tubing.

Table 4. The value of bottom hole pressure

Model	Pressure (psi)
General temperature model	5,083
Measured data	5,066
Linear interpolation temperature data	4,956
Prosper	4,984

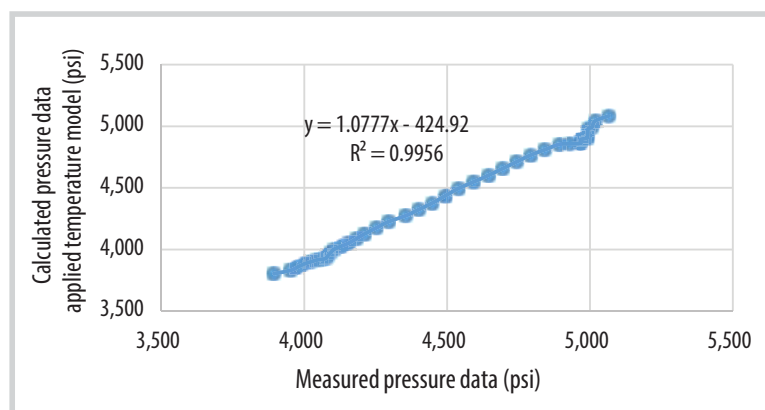


Figure 13. Data comparison of pressure in tubing from 8,100 ft - bottom hole.

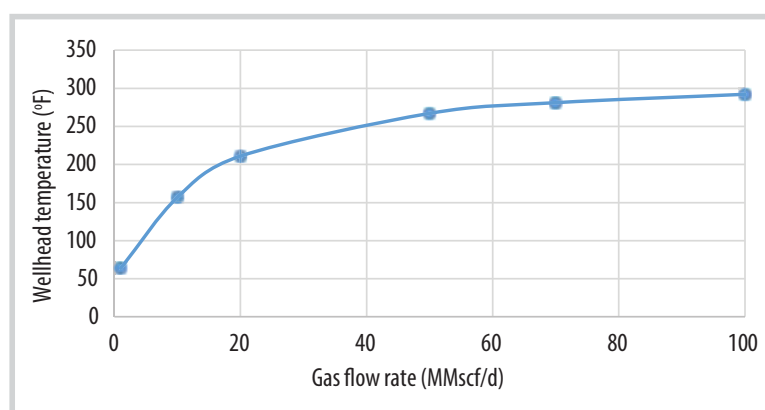


Figure 14. The relation between wellhead temperature and gas flow rate

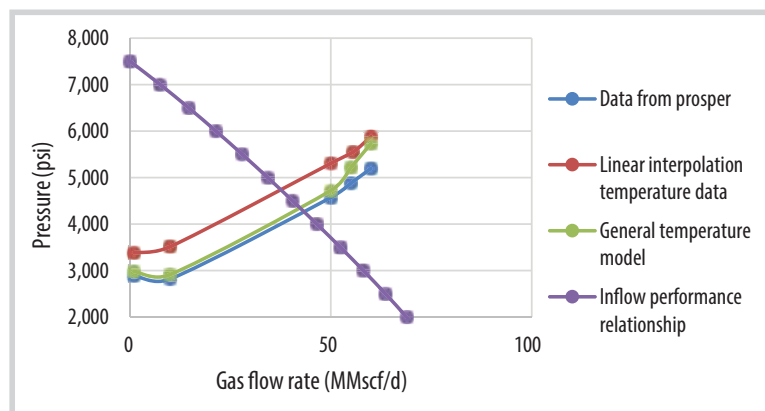


Figure 15. Gas well performance and compare the effect of temperature model.

Table 5. Well deliverability

Model	Bottom hole pressure (psi)	Qg (MMscf/d)
Linear interpolation temperature	4,789	38
General temperature	4,289	49
Prosper	4,223	51

corrected. It points out that if the surrounding region of tubing is only annulus and casing, there is no need to apply the heat transfer mechanism to generate tubing pressure profile.

At the section from 8,100 ft of true vertical depth to the bottom hole, the pressure traverse has been analysed:

With pressure line drawn by applying the general temperature model, the pressure figures have a high acceptance, compared to the measured data. On the other hand, with the line generated by Prosper software, the value obtained is quite close to the measured data. Meanwhile, there is certain difference in calculating pressure traverse without recognising the temperature change affected by the heat mechanisms. The comparison of bottom hole pressure data is shown in Table 4.

To equalise the calculated and measured pressure data, a linear regression has been drawn. The R² value is 0.9956. It has the same value as number one. Accordingly, the pressure model was approved.

3.5. Effect of gas produced on gas temperature

In any case of production, the wellhead temperature must be lower than that at the bottom hole. From Figure 10, if the bottom hole temperature is kept constant in 321°F, when the gas produced rate is 55 million standard ft³ per day, the wellhead temperature is 268°F, it can be concluded that when gas flows up to the wellhead, the higher rate of gas is produced, the lower the temperature loss will be due to the low effect of convection inside the production tubing. A low production rate gives low wellhead temperature as the heat mostly transfers to the ambient environment.

3.6. Temperature effect on gas production flow rate

The relation between gas temperature, pressure and flow rate within the production tubing can be seen in the vertical lift performance (VLP). In applying nodal analysis, various rates are calculated to find out the well operating point. From that, temperature change in the production tubing impacts on the gas production rate prediction. The reliability of vertical lift performance should be checked again.

Table 6. Gas composition

Gas composition (%)			
N₂	0.08	iC4	1.32
CO₂	0.07	nC4	2.14
H₂S	0	iC5	0.91
C1	70.5	nC5	1.01
C2	9.11	nC6	1.3
C3	1.32	C6+	8.23

Table 7. Reservoir input data

Pr (psi)	7,500
Tr (°R)	810
h (ft)	300
k (mD)	2
r _w (ft)	0.25
r _e (ft)	2,979
s	2
D, non - Darcy flow factor	0.00006

Table 8. Well depth

Measured depth (ft)	True vertical depth (ft)
0	0
6,662	6,620
13,419	12,731

Table 9. Well input data

Gas flow rate (MMscf/d)	55.5
Gas oil Ratio - GOR	7,690
Production tubing ID (inch)	3.826
Production tubing OD (inch)	5.042

The vertical lift performance is tested by applying the Gray correlation. The Prosper software gives a similar number in operating point compared with the curve used temperature model. The vertical lift performance which does not contain the temperature model has a lower value of well deliverability than the others. The gap between this vertical lift performance curve and the others can be explained by the impact of temperature on the pressure profile while increasing the flow. To generate vertical lift performance curve, it uses the value of Q: flow rate and temperature profile to predict the bottom hole pressure (BHP) and draw the relation between Q and the bottom hole pressure. If the temperature drop is in the linear gradient and the flow is too fast, there will be more errors in the pressure value. It should acquire the heat transfer model in wellbore to ensure the accuracy of well deliverability.

In comparison to the other models, the value of gas flow rate in the pressure without temperature model is lower, at 38 and 49,51 million standard ft³ per day, respectively. According to Table 5, if the pressure model does not account for temperature along the tubing, the produced gas flow rate will be reduced.

4. Conclusion

In order to produce single-phase gas in a gas well, the pressure gradient in the tubing must be reasonable. An incorrect value of gas flow rate will result from an error in pressure measurement. One of the variables suspected of causing errors in the pressure gradient measurement is the temperature model in the wellbore. There are some remarkable points in this study:

To predict bottom hole pressure, the temperature profile in the production tubing should be computed considering the specified heat transfer mechanism since it gives a small error. The gas temperature model is checked with the measured data and shows nearly accurate value. With the bottom hole temperature being 321°F, the gas test rate 55.5 million standard ft³ per day, the wellhead temperature calculated by heat transfer mechanism 268°F, the predicted bottom hole pressure is virtually accurate compared to pressure values that do not involve a heat transfer mechanism.

The heat transfer process in the wellbore happens in two main directions: horizontal: heat transfer from the production tubing to the annulus, casing or cement known as conduction, and vertical: heat changes based on the convection process in the production tubing. Conduction occurs at the top section of the well. Convection is the most critical part in decreasing the gas temperature due to fast flow rate at the well head. Radiation has a minor impact on the pipe wall. Hence, it should be taken into account in order to ensure the model's accuracy.

Fluid temperature has a significant impact on gas viscosity since it is directly related to the cooling of the gas flow. Once implementing the temperature model, the result shows that the viscosity at the wellhead is 0.017 cp. The Z factor equals 0.92 for the wellhead and 1.92 for the bottom hole, respectively. In addition to affecting the bottom well pressure value, these two parameters also influence gas flow

rate. Low gas viscosity and Z factor value due to incorrect temperature profile can result in low production rate and damage to the operation procedure because two-phase flow happens.

Gray correlation gives a high level of accuracy in the value of pressure profile compared between calculated and measured data. As higher flow rates the wellhead temperature is also high corresponding the flow rate prediction of well deliverability. The vertical lift performance model containing the temperature model gives a similar value of gas production rate as compared with the Prosper commercial software: 49 million standard ft³ per day and the bottom hole pressure is 4,289 psia. The correct vertical lift performance model delivers a great level of accuracy in determining the gas flow rate.

Acknowledgment

This research is sponsored by Ho Chi Minh City University of Technology under grant C2021-20-39.

6. References

[1] M. Rasin Tek, Donald L. Katz, Jack R. Elenbaas, Michael Whims, and Joseph L. Roberts, "Temperature and

pressure gradients in gas wells", *SPE Annual Fall Technical Conference and Exhibition, Houston, Texas, 1 - 3 October 1978*. DOI: 10.2118/7495-MS.

[2] Rajiv Sagar, D.R. Doty, and Zellmir Schmltdt, "Predicting temperature profiles in a flowing well", *SPE Production Engineering*, Vol. 6, No. 4, pp. 441 - 448, 1991. DOI: 10.2118/19702-PA.

[3] A.Aarvik, S. Djuve, and A. Valle, "Steady state calculations of wellbore and wellhead temperatures", *14th International Conference on Multiphase Production Technology, Cannes, France, 17 - 19 June 2009*.

[4] P. Experts, "IPM prosper user manual", 2009.

[5] Mehdi Kasbi, "Thermal insulation of tubing in the petroleum industry", 2018.

[6] H. Dale Beggs, *Production optimization using nodal analysis (1st edition)*. Oil & Gas Consultants International, 2008.

[7] Boyun Guo, William C. Lyons, and Ali Ghalambor, *Petroleum production engineering: A computer-assisted approach (4th edition)*. Elsevier, 2007.

MICRO/NANOSTRUCTURED ZNO-BASED SUPERHYDROPHOBIC STEEL SURFACE WITH ENHANCED CORROSION PROTECTION

Nguyen Thi Phuong Nhung¹, Nguyen Thi Ngoc Tien¹, Nguyen Hoang Luong¹
Tran Thu Hang², Nguyen Van Kiet¹, Nguyen Phan Anh¹

¹Petrovietnam University

²Petrovietnam Manpower Training College

Email: nhungntp@pvu.edu.vn

<https://doi.org/10.47800/PVJ.2021.06-07>

Summary

This paper presents a simple process of fabricating a superhydrophobic carbon steel surface with high water repellence and good corrosion resistance. The steel surface was covered by thin ZnO layers via various methods of sol-gel method, hydrothermal synthesis, and electrochemical deposition, then further functionalised with methyltrichlorosilane. Morphological features observed by a scanning electron microscope (SEM) show that ZnO layers are composed of micro/nanostructures. Furthermore, the chemical composition of these films has been analysed by an energy dispersive X-ray spectroscopy (EDX). An optimum experimental condition, based on the type of Zn deposition method, has been obtained to provide superhydrophobic properties with a water contact angle of $152 \pm 2^\circ$. In a 3.5 wt% NaCl solution, the corrosion resistance properties of the superhydrophobic ZnO-coated steel are found to be very good with an anti-corrosion efficiency of 93.12%.

Key words: Superhydrophobic, ZnO electrodeposition, micro and nanostructures, corrosion resistance.

1. Introduction

Carbon steel materials are widely used in the oil and marine industries due to its reasonable corrosion resistance, good strength, and high durability. However, carbon steel is generally susceptible to localised corrosions caused by Cl⁻, leading to massive economic losses every year. In fact, carbon steel corrosion is an oxidation process where the metal is the anode in an electrochemical cell and the electrolyte is the environment. In the past decades, various strategies have been developed to control and prevent the occurrence of carbon steel corrosion, where the basic concept is to remove one or more of the electrochemical cell components (anode, cathode, environment). The most popular method is to coat a steel surface with an anti-corrosive layer to provide a barrier between the steel surface and the corrosive environment. However, in the case of hydrophilic coating, it leads to steel corrosion because of the contact between the corrosive solution and the steel/coating interface. In contrast, in the case of

hydrophobic coating (unlike water), the repellent ability against the water of hydrophobic surface can reduce the contact area of corrosive liquid and the surface and hinder the migration of corrosive ions to the steel surface, leading to a decrease in the corrosion rate of material. In recent years, superhydrophobic steel surfaces (having a water contact angle higher than 150°) have attracted numerous research groups because of their features as a special anti-corrosion coating [1 - 3].

According to the micro/nano composite structures of natural surfaces such as lotus leaves, butterfly wings, and fish scales [4], researchers found that surface chemical composition and surface roughness were the key factors contributing to the formation of superhydrophobic surfaces. There are various methods to build superhydrophobic surfaces, including electrodeposition, anodic oxidation, chemical etching, and sol-gel methods. Most of the methods are based on the combination of (i) roughening the surface of low surface energy material, and/or (ii) modifying a rough surface by depositing low surface energy material. Chen et al. made the superhydrophobic steel surface by using polyurethane/nano-Al₂O₃ coating. The superhydrophobic aluminium-



Date of receipt: 25/2/2022. Date of review and editing: 25/2 - 29/4/2022.

Date of approval: 27/6/2022.

coated steel surface shows excellent anticorrosive performance with a contact angle of 151°. Xiang et al. fabricated a superhydrophobic surface on steel surface by combining two steps, including the formation of porous ZnO coating and modification of myristic acid. Chongwei et al. also built the superhydrophobic steel surface by a two-step process, involving the etching step with Piranha solution and fluorination treatment. The superhydrophobic steel surface exhibits high resistance to water, acid solution, and alkaline solution [5, 6].

In this work, the superhydrophobic surface of carbon steel was prepared in two steps: the carbon steel substrate was first covered by micro and nanostructured ZnO to increase the surface roughness, and then followed by a chemical modification with methyltrichlorosilane to reduce the energy surface thanks to $-CH_3$ group on the steel surface. One of the reasons to choose ZnO to create the superhydrophobic carbon steel is that ZnO layers have not only been widely used to prevent the corrosion of the steel surface but also easily modified chemically. In this study, micro and nanostructured ZnO coating was introduced into the carbon steel surface by using three coating protocols such as nanoparticles coating by sol-gel method, electrodeposition, and hydrothermal growth. Micro and nanostructured ZnO was deposited on the steel surface by one of three methods: sol-gel method, hydrothermal synthesis, and electrochemical deposition. The micro and nanostructure, wettability, and chemical composition of superhydrophobic coating were evaluated by scanning electron microscope (SEM), energy dispersive X-ray spectroscopy (EDX), and contact angle measurement. Moreover, the anti-corrosion property of coating was investigated via potentiodynamic polarisation curve acquired by electrochemical experiment in 3.5 wt% NaCl solution (using electrochemical equipment SP-300 system).

2. Materials and methods

2.1. Materials

Methyltrichlorosilane, ethanol, acetone, H_2SO_4 , H_2O_2 , NH_3 , and $Zn(CH_3COO)_2$ are obtained from Sigma-Aldrich. In this study, two kinds of steel substrates, API 5L X65 and CT3 are used. The X65 steel is obtained from VINA Tan Phat company and has the following composition: Fe (98.8%), C (0.12%), Mn (0.69%), Si (0.11%), Cr (0.02%), and Ni (0.01%). The CT3 steel is from China and consists of Fe (42.89%), C (0.14%), Mn (11.12%), Si (0.13%), Cr (0.02%), and Zn (0.51%).

2.2. Preparation of superhydrophobic steel surface

The fabrication process of the superhydrophobic carbon steel surface includes 2 steps: first, a thin layer of micro and nanostructured ZnO is deposited on the steel substrate, then this is followed by chemical treatment with methyltrichlorosilane.

2.2.1. Formation of micro and nanostructured ZnO coating

The steel surfaces are cut into 0.1 cm x 1 cm x 0.5 cm for the X65 substrate, and 1.5 cm x 3.0 cm x 3.0 cm for the CT3. The substrates are then polished by sandpaper (100, 200, and 600 grit) and subsequently degreased in acetone and ethanol, and finally rinsed with distilled water.

There are 3 methods to prepare the micro and nanostructured ZnO coating on the steel substrate: (i) sol-gel method, (ii) hydrothermal synthesis, and (iii) electrochemical deposition.

- Sol-gel method: Solution of ZnO seed layer is prepared by using the sol-gel method. Zinc acetate dihydrate (ZAD) is dissolved in absolute ethanol. Using a dropper, the 0.048 M ZAD solution is dropped onto a cleaned steel surface and left for 15 seconds, followed by a rinse with absolute ethanol; this step is repeated 15 times. The substrate is then annealed on a hot plate at 350°C for 1 hour. More details of the growth conditions can be found in the article by Suvindraj Rajamannickam [11].

- Hydrothermal synthesis: Zinc acetate dihydrate is dissolved in 250 ml of distilled water; 0.3 ml of ammonium hydroxide is then added to this solution and stirred at room temperature for 30 minutes. The steel substrate with the seed that was prepared previously by the same sol-gel method is placed vertically in this aqueous solution for 1 hour at 90°C. More details of the growth conditions can be found in the article by Wided Chebil et al. [2].

- Electrochemical deposition: The steel substrate is firstly dipped into 0.1 M HCl solution for 30 seconds before the zinc electrodeposition process is conducted for different time durations: 5 mins, 15 mins, 30 mins, and 60 mins. More details concerning this process are described in our previous article [10].

A two-electrode cell is used, in which the cathode is the steel substrate, the anode is a Zn metal sheet (0.2 x 2 x 5 cm) and the electrolyte is deionised water. A constant voltage of 1 V is applied between the two electrodes to grow the Zn layer in different durations. After electrolysis, the substrate is cleaned with deionised water and then

dried. Finally, the substrate is annealed in furnace at 250°C for 120 minutes to form a ZnO thin film coating on the steel surface.

2.2.2. Surface functionalisation by silanisation

The ZnO-coated steel substrates are UV/O₃ treated for 30 minutes to remove any organic contaminants and to generate surface hydroxyl -OH groups. The activated surface is then directly dipped into a solution containing 10 vol% methyltrichlorosilane in ethanol for 12 hours. The substrate is rinsed 3 times with ethanol and further dried under a gentle nitrogen flow, and finally kept in a clean oven at 120°C for 10 minutes.

2.3. Sample characterisations

Morphology and composition of the thin film is characterised by JEOL JSM-7600F SEM, X-ray microanalyser by Oxford Instruments EDS. The wetting properties of all substrates are determined by measuring static water contact angle with OCA - DataPhysics Instruments at 3 positions on each surface using 5 µl distilled water.

2.4. Corrosion resistance test

The corrosion tests are carried out at room temperature in a 3.5 wt% NaCl solution using the SP-300 system. The exposed coating area is 0.785 cm². Ag/AgCl and pure graphite electrodes are used as the reference and counter electrodes, respectively. Prior to the potentiodynamic polarisation test, the samples are stored in the solution for 1 hour to establish the open circuit potential (OCP). The potential of the electrodes is swept at a rate of 0.166 mV/s, ranging from an initial potential of -250 mV vs. E_{corr} to a final potential of -200 mV Ag/AgCl. Electrochemical impedance spectroscopy (EIS) is conducted using an SP-300 system with a commercial software programme. The amplitude of the sinusoidal peak - peak perturbation is 10 mV. The frequency varies from 100 kHz to 10 mHz.

3. Results and discussion

3.1. Surface morphology and wettability

Figure 1 reveals the SEM results of the surface morphology of carbon steel coated with and without different micro and nanostructured ZnO layers: (i) steel surface without coating ZnO layer (CTs-1); (ii) steel surface coated with ZnO particles by sol-gel method (CTs-2); (iii) steel surface with ZnO layer deposition by hydrothermal method (CTs-3); and (iv) steel surface with ZnO layer by electrochemical deposition.

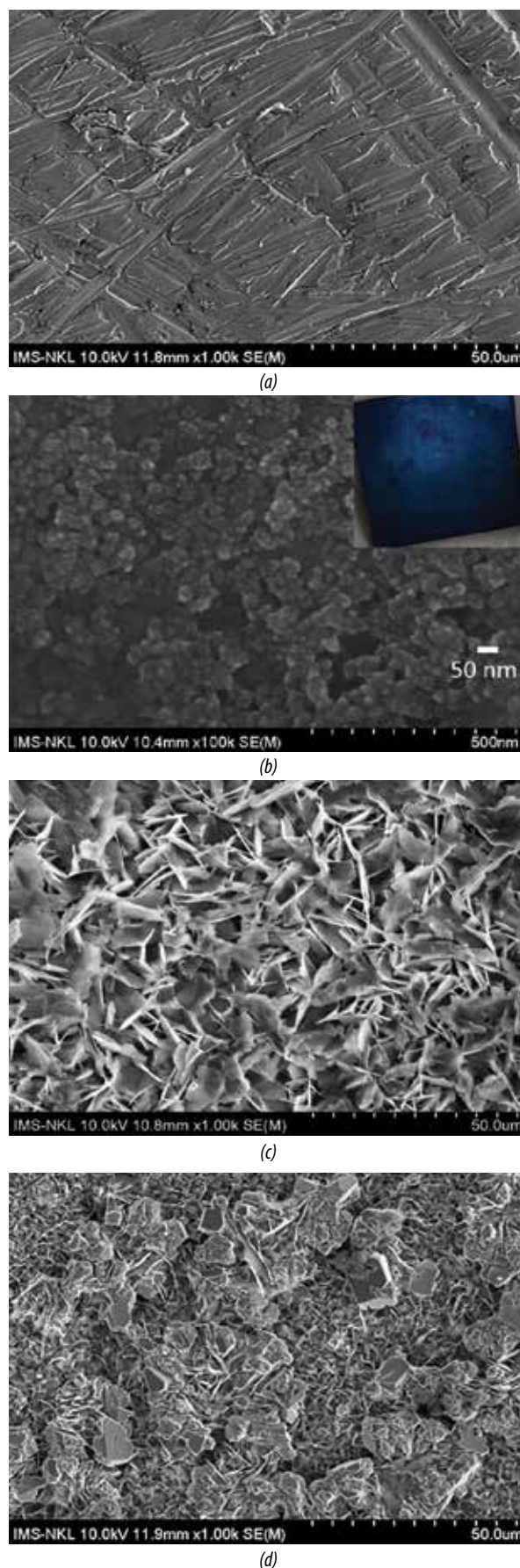


Figure 1. SEM morphology of (a) CTs-1, (b) CTs-2, (c) CTs-3, (d) CTs-4.

After chemical modification with methyltrichlorosilane, their hydrophobic ability is evaluated via water contact angle measurements. The results are shown in Figure 2.

As shown in Figure 1a, the ZnO-uncoated surface of CTs-1 is rough with some minor scratches, holes, and other defects. After chemical modification with silane, the contact angle increases from $63 \pm 2^\circ$ to $93 \pm 2^\circ$ (Figure 2).

According to the treatment with ZnO particles by sol-gel method, there are several nanoparticles of around 10 - 20 nm located on the CTs-2 substrate (Figure 1b). The corner of Figure 1b is a photograph of a steel surface with a ZnO seed layer. The bluish tinge appears after the seed layer is annealed. However, these particles are not distributed homogeneously, and the water contact angle is smaller, $73 \pm 2^\circ$ (Figure 2). It can be explained that the scratches, holes, and other defects on the original surface are filled with ZnO particles, making the surface less rough and more hydrophilic after chemical modification with silane.

When the CTs-2 substrate is immersed into the NH_3 solution, ZnO particles are transformed into a plate-like structure on CTs-3 (Figure 1c). A staggered coating distribution is also observed on the sample surface; the thickness and size of the coating are uniform and there is a gap between the lamellas. The structure of this composite interface greatly improves the surface roughness. Its hydrophobic property changes dramatically with a water contact angle of $142 \pm 2^\circ$.

In terms of electrochemical deposition, CTs-4 is covered with a new structure of two layers (Figure 1d).

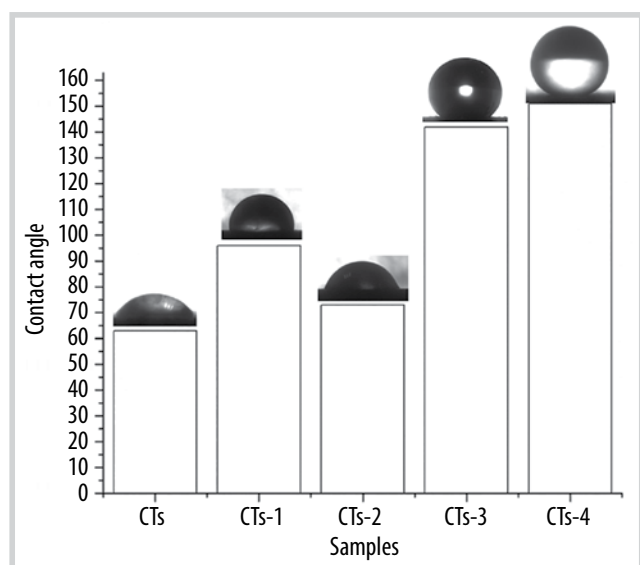


Figure 2. Contact angle of different samples: CTs, CTs-1, CTs-2, CTs-3, CTs-4.

The top layer presents a large amount of accumulated microparticles on the surface while the bottom layer possesses a plate-like structure. In this case, air can fill in these pores, preventing water droplets from entering and increasing the contact angle of the substrate. The surface becomes superhydrophobic with a contact angle of $151 \pm 2^\circ$.

In conclusion, micro and nanostructured ZnO can be formed on the steel surface by 1 of the 3 methods: deep coating to form the particles, hydrothermal growth, and electrochemical deposition. Each coating method results in different steel surface morphology. Compared to the other two, the electrochemical deposition offers a feasible method to control the coating thickness and the surface morphology. Therefore, the electrochemical deposition will be used in this investigation on superhydrophobic surface.

3.2. Effect of substrate type on formation of nanostructure

To evaluate the influence of substrate types on ZnO micro and nanostructure in the electrodeposition method, 2 carbon steel surfaces of CT3 and X65 substrates are considered. Figure 3 indicates the SEM results of carbon steel surface morphology before (CTs-1 and Xs-1 substrates) and after electrodeposition for 5 minutes (CTs-5 and Xs-2 substrates), and for 15 minutes (CTs-6 and Xs-3 substrates).

From Figure 3, after polishing by sandpaper (100, 200, and 600 grit), the morphology surfaces of two types of steel substrate, X65 and CT3, are not similar. Some minor scratches appear on the CT3 steel substrate (CTs-1) while small holes show on the X65 steel substrate (Xs-1). Obviously, the Xs-1 surface is rougher than the CTs-1; i.e. a higher amount of air can be trapped into the structure of the Xs-1 surface compared to the CTs-1 surface. It results in a higher hydrophobicity of the Xs-1 surface (CA = $126 \pm 2^\circ$) than that of the CTs-1 (CA = $93 \pm 2^\circ$) after the chemical modification with silane. Increasing time of electrochemical deposition leads to a larger thickness and a higher roughness of micro and nano ZnO cover:

+ After 5 minutes of electrochemical deposition, pores appear on the X65 substrate with higher density and size of around $0.25 \mu\text{m}$ (Xs-2 substrate's SEM image). Meanwhile, a high number of ZnO sphere particles grows on the CT3 surface (CTs-5 substrate's SEM image) with diameters of about $0.5 \mu\text{m}$. The Xs-2 and CTs-5 substrates,

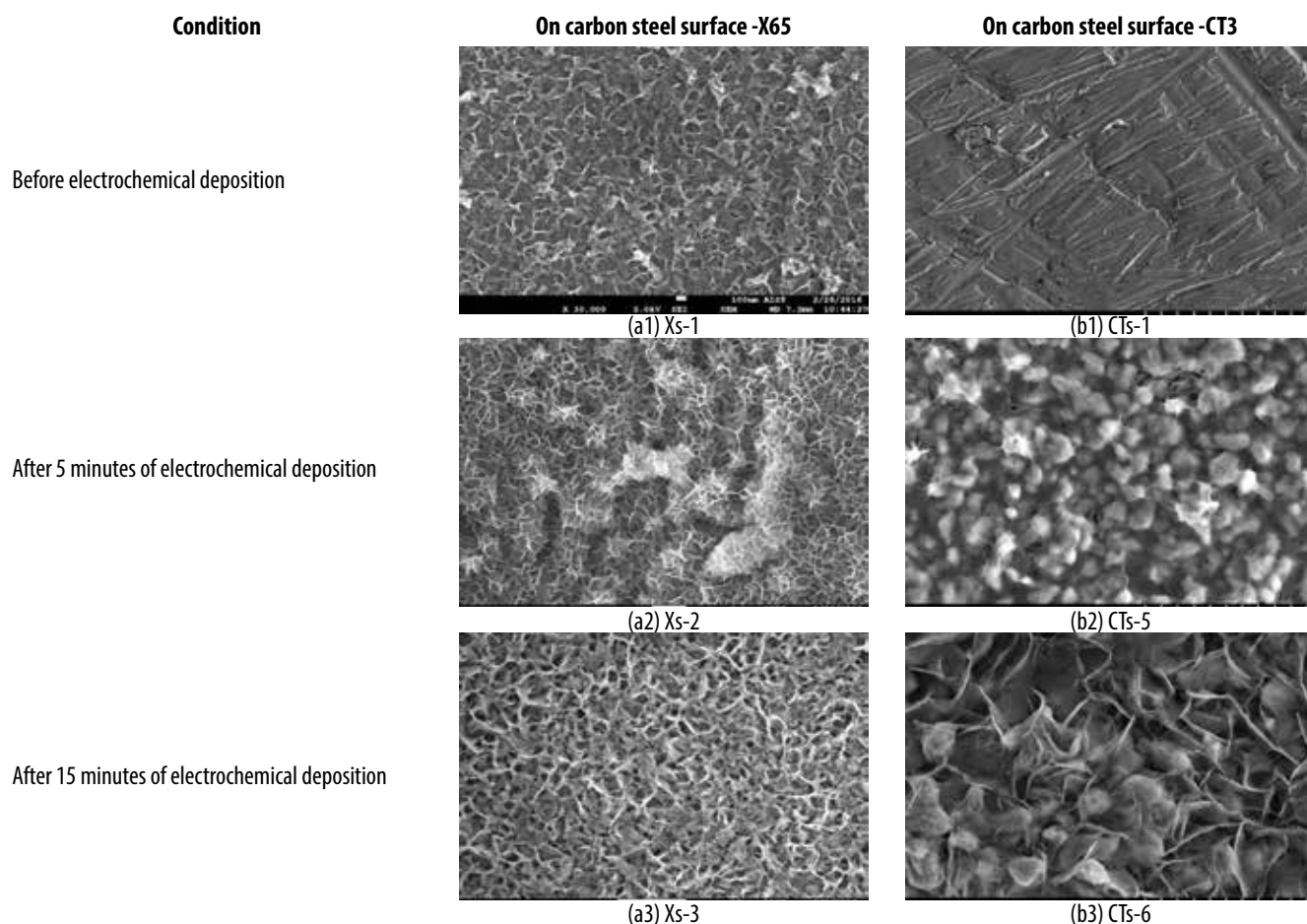


Figure 3. SEM morphology of (a1) Xs-1; (a2) Xs-2; (a3) Xs-3; (b1) CTs-1; (b2) CTs-5; (b3) CTs-6.

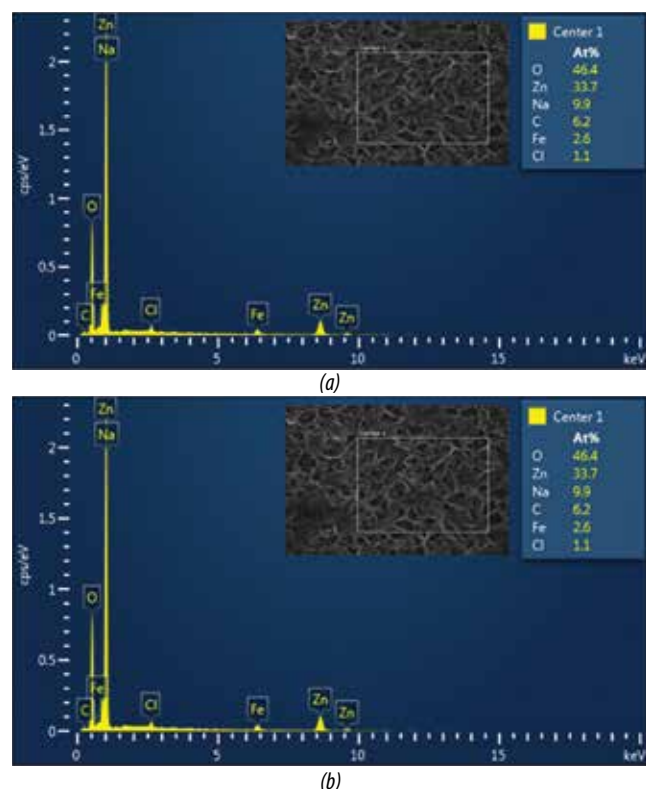


Figure 4. EDS analysis of the porous ZnO-coated steel surface (a) before silanisation and (b) ZnO coated steel surface with silanisation.

Table 1. Contact angle on different substrate: Xs-0; Xs-1; Xs-2; Xs-3; CTs-0; CTs-1; CTs-5; CTs-6

X65 steel substrate	CT3 steel substrate
54° ± 2° (Xs-0)	63 ± 2° (CTs-0)
126 ± 2° (Xs-1)	93 ± 2° (CTs-1)
130 ± 2° (Xs-3)	110 ± 2° (CTs-5)
152 ± 2° (Xs-2)	142 ± 2° (CTs-6)

with dramatically increasing hydrophobic properties, have a contact angle of 132 ± 2° and 112 ± 2°, respectively.

+ After 15 minutes of electrochemical deposition, the ZnO micro and nanostructure on the X65 substrate appears with a larger diameter and consists of double structure, including a small open circle structure and a small porous structure inside (Xs-3 SEM image). Meanwhile, in the case of the CT3 substrate, the appeared structure looks like a flower with a sphere particle (CTs-6 SEM image). In both substrates, the rough surface is upgraded, resulting in a significant rise in hydrophobicity on these substrates. Therefore, the CTs-6 surface is highly hydrophobic with a contact angle of 142 ± 2° and the Xs-3 surface becomes superhydrophobic with a contact angle of 152 ± 2°.

3.3. Chemical surface

The composition of ZnO thinly coated on steel substrate is analysed by EDS as shown in Figure 4a. EDS spectra show the presence of elements such as zinc (8.6 keV and 1.0 keV), oxygen (0.53 keV). From the data, it is apparent that thin ZnO layers have been successfully introduced through a simple deposition method, in agreement with the published data [12].

After silanisation, the composition of the ZnO-deposited steel interface is presented in Figure 4b. Compared to Figure 4a, it is important to note the appearance of Si atoms (1.7 keV) and the increase of C composition from 6.2% to 19.5% on the interface. These results are suitable for the silanisation process to form the CH₃-Si group on the ZnO-coated steel surface. In addition, the surface's wettability is changed after chemical modification. These results confirm that the silanisation of the ZnO-coated steel surface is successful.

3.4. Anticorrosion properties

Figure 5 presents the potentiodynamic polarisation curves of steel surface and ZnO-functionalised steel substrate. The substrate with coating shows a lower corrosion current density, resulting in improved corrosion resistance. In addition, it also shows a protected range in the anodic polarisation and there was no pitting observed up to 200 mV Ag/AgCl. The

rapid increase in current density in the anode can be attributed to the anodic current density associated with oxygen evolution.

In this figure, the cathode branch is divided into two regions at slightly variable current densities. Zone I corresponds to the area near the corrosive voltage. The shape of this region depends on the depth of the solution layer. For the depth of 1.0 - 10 cm of the solution, near E_{corr}, it is possible to observe the presence of an interference, which may relate to the reduction of corrosive products to be formed in a stable time. Zone II - in addition to 50 mV of corrosive voltage, the shape and relationship of this region are due to the reduction of oxygen and controlled by mass transfer. In this region, the process of reducing oxygen and corrosive products takes place and is controlled by the rate of oxygen diffusion. The length of this region increases gradually as the depth of the solution layer increases, which may indicate that the amount of oxygen removed is proportional to the volume of the solution.

Table 2 indicates the corrosion properties of steel substrate and the ZnO-functionalised steel substrate obtained from the polarisation test. The protective efficiency (P_i) of the coatings is determined by Equation (1):

$$P_i = 100 \times \left(1 - \frac{i_{corr}}{i_{corr}^0} \right) \tag{1}$$

where i_{corr} and i_{corr}⁰ are the corrosion current densities in the presence and absence of a coating layer, respectively. The electrochemical characteristics of the surface with ZnO-functionalised coating show a lower protective current density in comparison to the results of the steel substrate without coating. Table 2 indicates that the protective efficiency of surface with coating is quite high, 93.12%, indicating good corrosion protection.

Figure 6a indicates the Nyquist plots of steel surface without coating (black line) and ZnO-functionalised steel substrate (red line) in 3.5 wt%

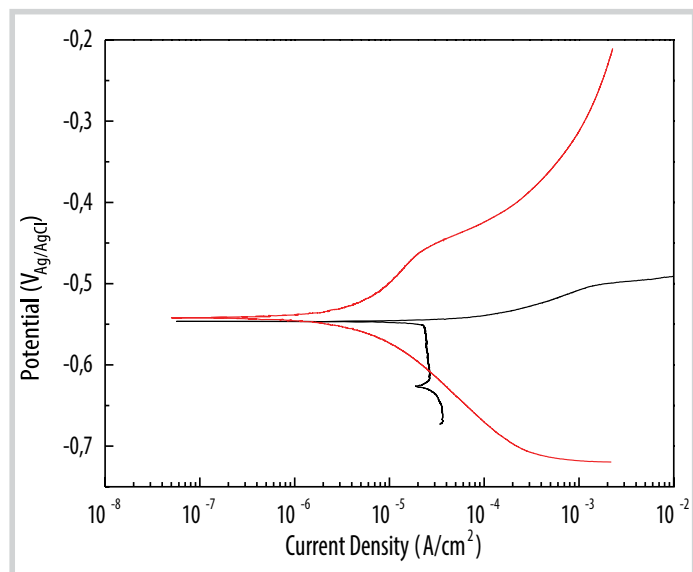


Figure 5. Potentiodynamic polarisation curves of steel surface without coating (black line) and ZnO functionalised steel substrate (red line).

Table 2. Corrosion properties of steel surface without coating and ZnO functionalised steel substrate

Specimen	E _{corr} (mV _{Ag/AgCl})	i _{corr} (×10 ⁻⁶ A/cm ²)	β _a (mV/decade)	-β _c (mV/decade)	η (%)
Steel substrate	-547	24.7	10.8	253.2	-
Coated steel	-542	1.7	86.7	68.4	93.12

NaCl solution after 1 hour immersion. The impedance diagrams of the coated substrate present a much larger impedance than the bare steel, indicating an effective barrier behaviour on the corrosion process. It is related to

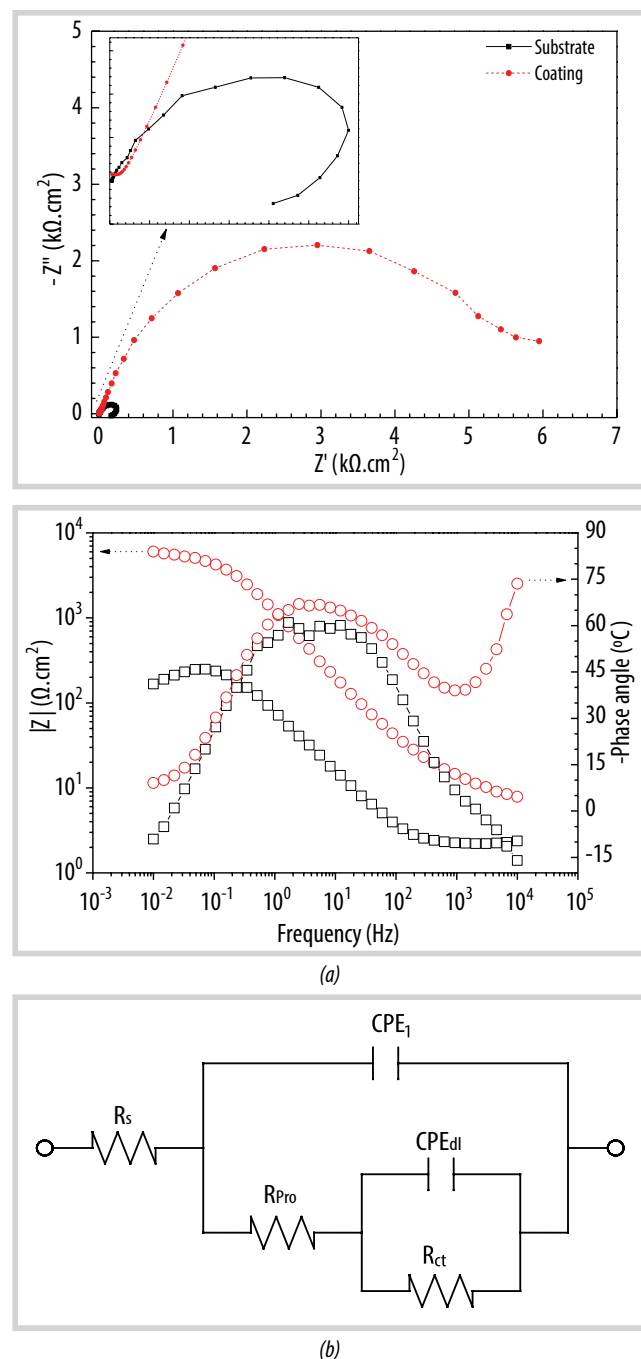


Figure 6. Nyquist and Bode plots of steel surface without coating (black line) and ZnO functionalised steel substrate (red line) (a); Proposed equivalent circuit for fitting EIS data (b).

the treatment process controlled by ZnO functionalisation with the $-\text{CH}_3$ group on the steel surface. In this study, the semicircle depression in the Nyquist diagram of the steel substrate without coating can be attributed to the heterogeneity of the steel surface, which is caused by the difference in droplet distribution and surface roughness. This effect is omitted due to a protective film formation, which acts as a physical barrier layer formation on the steel surface. The data typically shows a two-phase constant. Therefore, the corresponding equivalent circuit for fitting EIS data is proposed as shown in Figure 6b, where R_s represents the solution resistance between the reference and working electrodes; CPE_1 is the coating constant phase element; R_{coat} is the coating resistance; R_{ct} is the charge transfer resistance; and CPE_2 is the double layer constant phase element (R_{coat} is replaced by R_{rust} for the steel substrate). The ZSimpWin software is used to fit the EIS data to determine the optimised values for the protective film and charge transfer resistance, as well as protective layer and double layer capacitances, which are given in Table 3. The results show that the coating exhibits a high charge transfer resistance, indicating a low corrosion rate, as shown in Tables 2 and 3. Overall, a coating provides a good corrosion protection by improving the corrosion resistance of a steel substrate in 3.5 wt% NaCl solution.

4. Conclusion

We have successfully achieved the superhydrophobic steel surface with micro/nanostructured ZnO coating by different methods. The obtained superhydrophobic surface presents a water contact angle of $152 \pm 2^\circ$ with low hysteresis. Furthermore, the steel surface with ZnO-functionalisation also provides a good anti-corrosion property with a protective efficiency of 93.12%. Hence, through a simple process of ZnO deposition and silanisation, the steel substrate shows both superhydrophobic properties with low hysteresis and a good corrosion resistance.

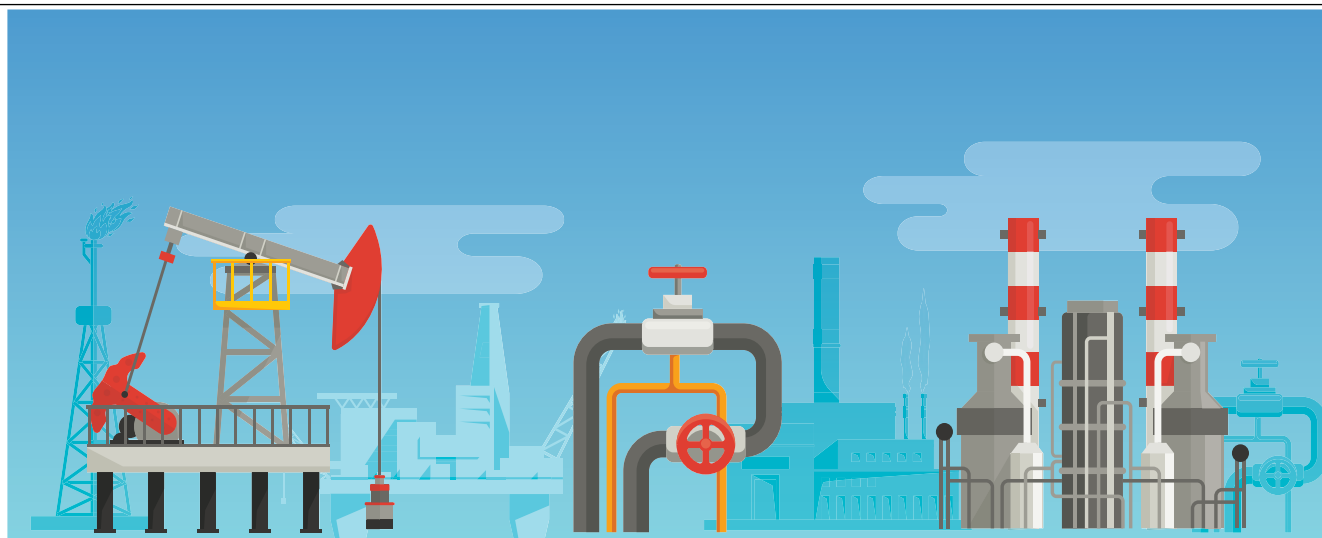
Acknowledgments: This work is funded by Petrovietnam University under grant code GV2004.

Table 3. The fitted results of EIS data

Specimen	R_s ($\Omega \cdot \text{cm}^2$)	CPE_{pro}		R_{pro} ($\Omega \cdot \text{cm}^2$)	CPE_{dl}		R_{ct} ($\Omega \cdot \text{cm}^2$)
		C ($\mu\text{F}/\text{cm}^2$)	n (0~1)		C ($\mu\text{F}/\text{cm}^2$)	n (0~1)	
Steel substrate	2.25	1536	0.8727	61.7	1266	0.8001	190
Coated-steel	3.45	159	0.8901	1039.4	41	0.9544	6964

References

- [1] Aziz Fihri, Enrico Bovero, Abdullah Al-Shahrani, Abdullah Al-Ghamdi, and Gasan Alabedi, "Recent progress in superhydrophobic coating used for steel protection: A review", *Colloids and Surfaces A: Physicochemical and Engineering Aspects*, Vol. 520, pp. 378 - 390, 2017. DOI: 10.1016/j.colsurfa.2016.12.057.
- [2] Wided Chebil, Anisha Gokarna, Afif Fouzri, Neje Hamdaoui, Komla Nomenyo, and Gilles Lerondel, "Study of the growth time effect on the structural, morphological and electrical characteristics of ZnO/p-Si heterojunction diodes grown by sol-gel assisted chemical bath deposition method", *Journal of Alloys Compounds*, Vol. 771, pp. 448 - 455, 2018. DOI:10.1016/j.jallcom.2018.08.280.
- [3] E. Vazirinasab, R. Jafari, and G. Momen, "Application of superhydrophobic coatings as a corrosion barrier: A review", *Surface and Coatings Technology*, Vol. 341, pp. 40 - 56, 2018, DOI: 10.1016/j.surfcoat.2017.11.053.
- [4] Joseph M. Mabry, Ashwani Vij, Scott T. Iacono, and Brent D. Viers, "Fluorinated polyhedral oligomeric silsesquioxanes (F-POSS)", *Angewandte Chemie International Edition*, Vol. 47, No. 22, pp. 4137 - 4140, 2008. DOI: 10.1002/anie.200705355.
- [5] Jiale Yong, Feng Chen, Qing Yang, Jinglan Huo, and Xun Hou, "Superoleophobic surfaces", *Chemical Society Reviews*, Vol. 46, No. 14, pp. 4168 - 4217, 2017. DOI: 10.1039/C6CS00751A.
- [6] Yuanyuan Miao, Dalei Zhang, Ning Cao, Liuyang Yang, Hong Ju, Rabah Boukherroub, Xueqiang Lin, Huiping Lin, and Youhai Jin, "Mussel-inspired superhydrophobic surfaces on 316L stainless steel with enhanced corrosion resistance", *Metallurgical and Materials Transactions A*, Vol. 51, pp. 909 - 919, 2020. DOI: 10.1007/s11661-019-05573-7.
- [7] Nguyen Thi Phuong Nhung, Renaud Dufour, Vincent Thomy, Vincent Senez, Rabah Boukherroub, and Yannick Coffinier, "Fabrication of superhydrophobic and highly oleophobic silicon-based surfaces via electroless etching method", *Applied Surface Science*, Vol. 295, pp. 38 - 43, 2014. DOI:10.1016/j.apsusc.2013.12.166.
- [8] Nguyen Thi Phuong Nhung, Pham Van Tong, Chu Manh Hung, Nguyen Van Duy, Nguyen Viet Chien, Nguyen Van Vinh, Nguyen Thai Tuyen, and Nguyen Duc Hoa, "Nanoporous ZnO nanostructure synthesis by a facile method for superior sensitivity ethanol sensor applications", *RSC Advances*, Vol. 6, No. 69, pp. 64215 - 64218, 2016. DOI: 10.1039/C6RA11531D.
- [9] Nguyen Thi Phuong Nhung, Philippe Brunet, Yannick Coffinier, and Rabah Boukherroub, "Quantitative testing of robustness on superomniphobic surfaces by drop impacts", *Langmuir*, Vol. 26, No. 23, pp. 18369 - 18373, 2010. DOI:10.1021/la103097y.
- [10] Nguyen Thi Phuong Nhung, Nguyen Viet Chien, Nguyen Dang Nam, Tran Phuong Huy, Nguyen Van Kiet, and Nguyen Van Duy, "Simple method to fabricate superhydrophobic carbon steel surface", *Petrovietnam Journal*, Vol. 10, pp. 44 - 47, 2016.
- [11] Suvindraj Rajamanickam, Sabah M. Mohammad, and Z. Hassan, "Effect of zinc acetate dihydrate concentration on morphology of ZnO seed layer and ZnO nanorods grown by hydrothermal method", *Colloid and Interface Science Communications*, Vol. 38, pp. 100312, 2020. DOI: 10.1016/j.colcom.2020.100312.
- [12] Shixiang Lu, Haiyan Gao, Wenguo Xu, Sabine Szunerits, and Rabah Boukherroub, "Fabrication of stable homogeneous superhydrophobic HDPE/graphene oxide surfaces on zinc substrates", *RSC Advances*, Vol. 6, No. 35, pp. 29823 - 29829, 2016. DOI: 10.1039/C6RA03730E.



WORLD OIL AND GAS MARKET

In “World Energy Investment 2022” report published by the International Energy Agency (IEA), world energy investment is set to rise over 8% in 2022 to reach a total of USD 2.4 trillion, above pre-Covid levels. Total upstream oil and gas investment is set to rebound by around 10% in 2022, led by the US majors, independents and NOCs in the Middle East... [1].

At USD 380 billion, upstream investment in 2021 was nearly 10%

greater than in 2020 but still less than 20% below pre-pandemic spending levels. Higher prices are expected to underpin a further 10% increase in 2022 on 2021 levels, according to the IEA’s World Energy Investment 2022 report. The focus in many cases has been on short-cycle investments that bring new supply to the market as quickly as possible, for example via tie-backs to existing projects and increased infill drilling [1].

The shift in overall spending towards

NOCs is a well-established trend and is set to continue. Middle Eastern NOCs’ spending is now well above pre-crisis levels. Saudi Aramco and Abu Dhabi National Oil Company (ADNOC) are looking towards aggressive growth following the 2020 downturn and have announced plans to increase investment spending by about 15 - 30% in 2022. Aramco’s spending is split roughly equally between its twin goals of increasing oil production capacity and domestic gas

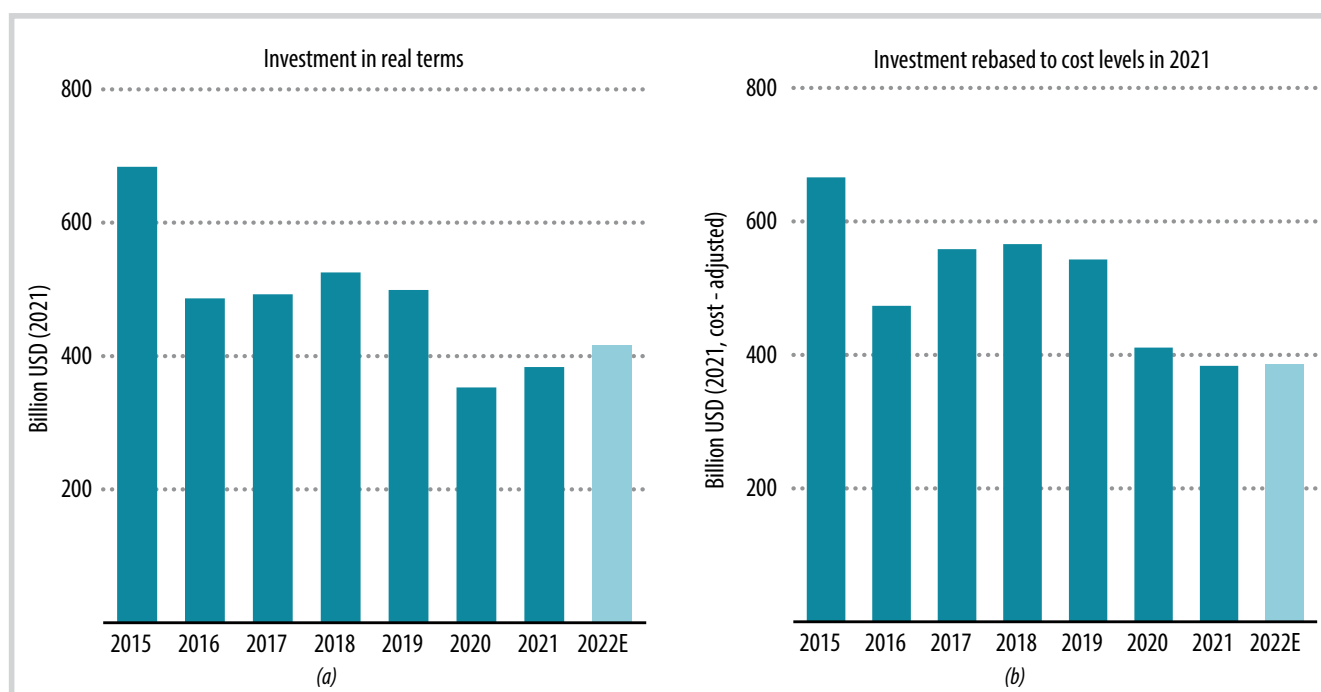


Figure 1. Global investment in upstream oil and gas in 2021, real terms (a) and rebased at constant 2021 costs (b), 2015 - 2022E.

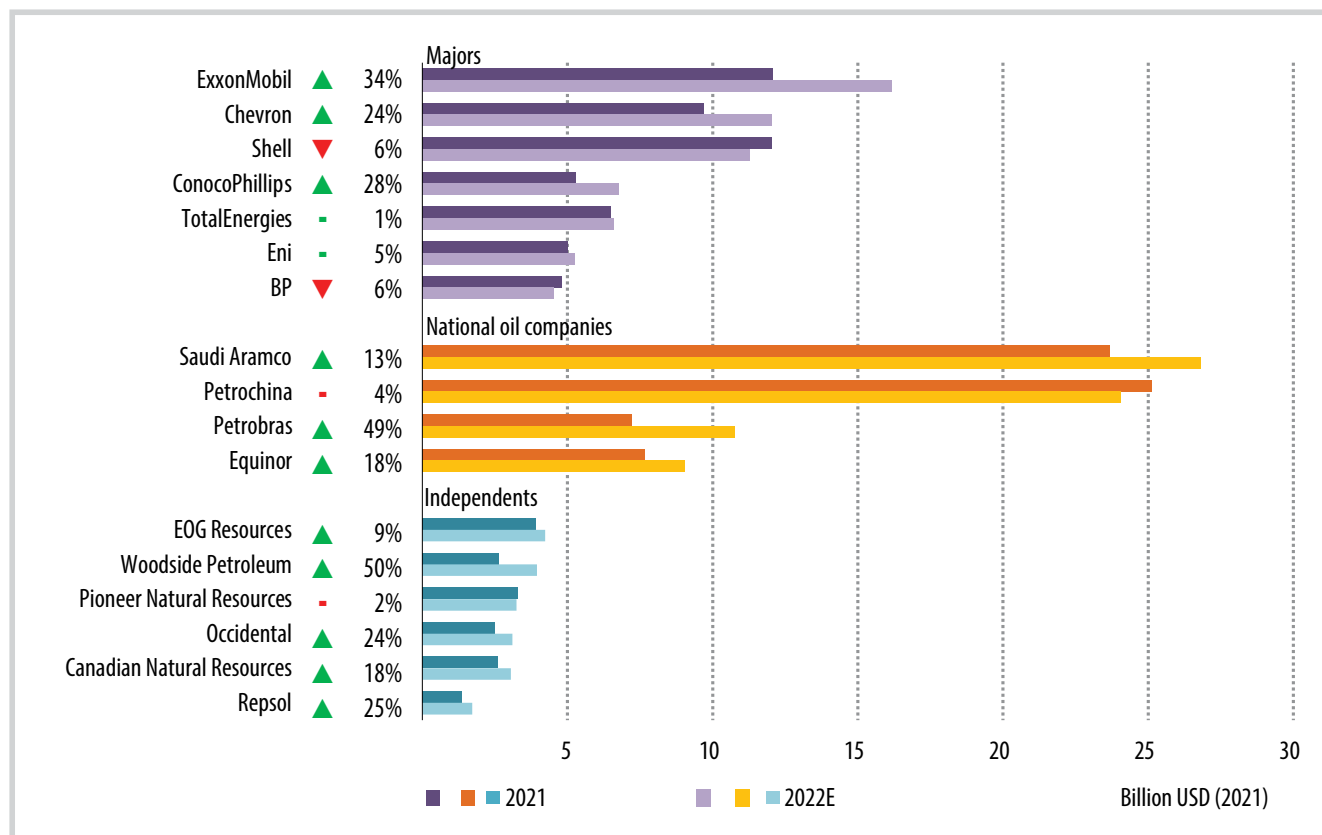


Figure 2. Upstream investment by selected oil and gas companies, 2021 and expected in 2022 [1].

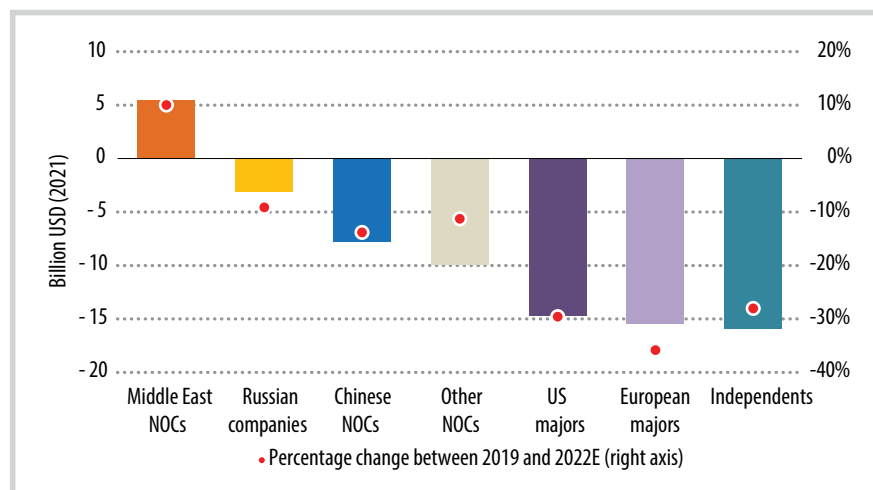


Figure 3. Estimated change in upstream spending by selected company types, 2019 - 2022E [1].

supply. Petrobras has announced plans to increase its spending by about 50% in 2022, after years focused on debt repayments.

Some Russian producers are reviewing their investment programmes due to sanctions and the announced exit of companies that have supported Russian supply growth since the 1990s. Rosneft's

spending will be watched closely as the ambitious strategy it laid out in 2021 so far remains in place with plans to increase overall oil and gas production by more than 20% to 2030 from 2021 levels.

Some of the largest increases in upstream investment in 2022 are expected to come from the US majors, which are looking to increase spending

by more than 30% in 2022. Meanwhile, planned upstream capital expenditure is essentially flat for the European majors in 2022, underscoring that their investment plans are driven more by long-term strategy commitments than by short-term prices. Independent US shale operators cut investment by around half in 2020 but announced activity levels indicate something of a rebound since then.

Nonetheless, investment in this area in 2022 is still expected to be around 30% below 2019 levels, given the focus on profitability and capital discipline rather than production expansion.

The upstream oil and gas industry has seen extreme volatility over the past decade. Investment reached its highest level in 2014 (at nearly USD 890 billion) but fell by over 45% between 2014 and 2016 as a result of the oil price crash, and

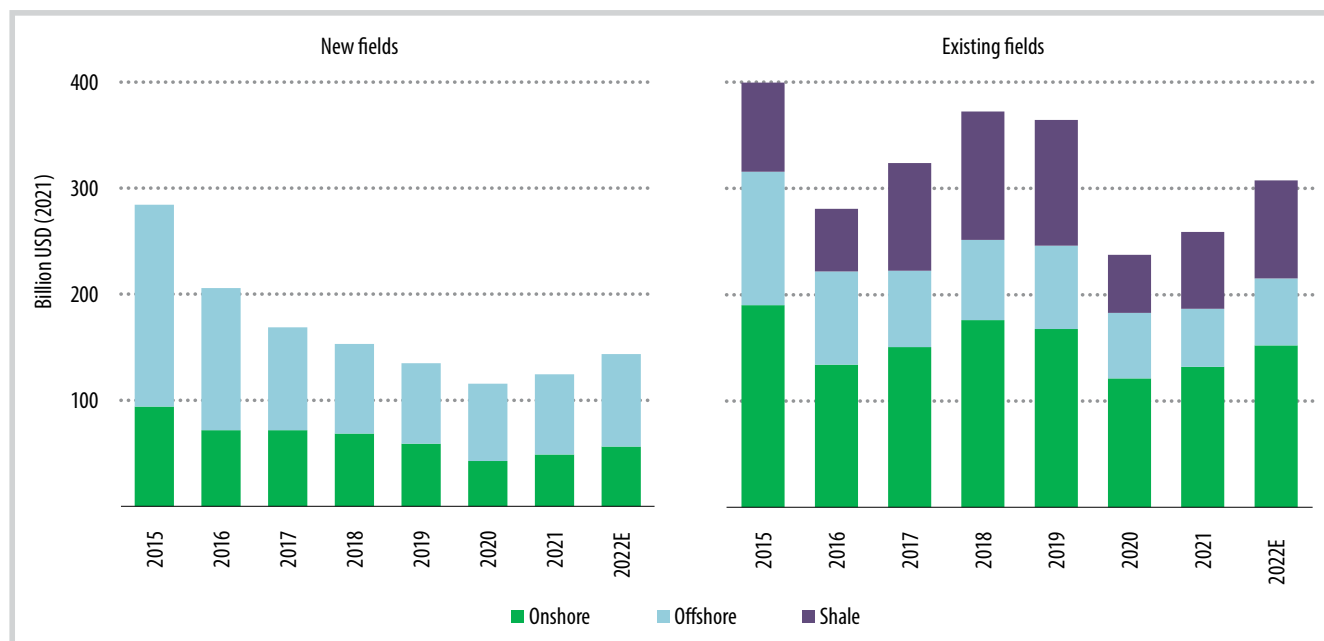


Figure 4. Upstream investment in new and existing oil and natural gas fields [1].

by a further 30% between 2019 and 2020 as a result of the pandemic [1].

For the moment, exploration activity remains well below levels prior to the 2015 oil price downturn; just under 10 billion barrels of oil equivalent were discovered in 2021, with exploration spending down 35% from 2019 levels.

Three discoveries account for about 40% of all announced oil and gas volumes discovered in 2021 are Zinichev in the Russian Arctic (discovered by Rosneft and BP), Baleine in Côte d'Ivoire (discovered by Eni), and North Sakarya in Turkey (discovered by TPAO).

The extension of the Guyana-Suriname basin by ExxonMobil, Hess and CNOOC in Guyana and TotalEnergies and APA Corporation in Suriname brought around 1.8 billion barrels of oil equivalent discovered volumes in 2021, with exploration success continuing in 2022 in Guyana and with Krabdagu in Suriname. The Shafag Asiman discovery in Azerbaijan was announced by BP and Socar, but few details on volumes were made public.

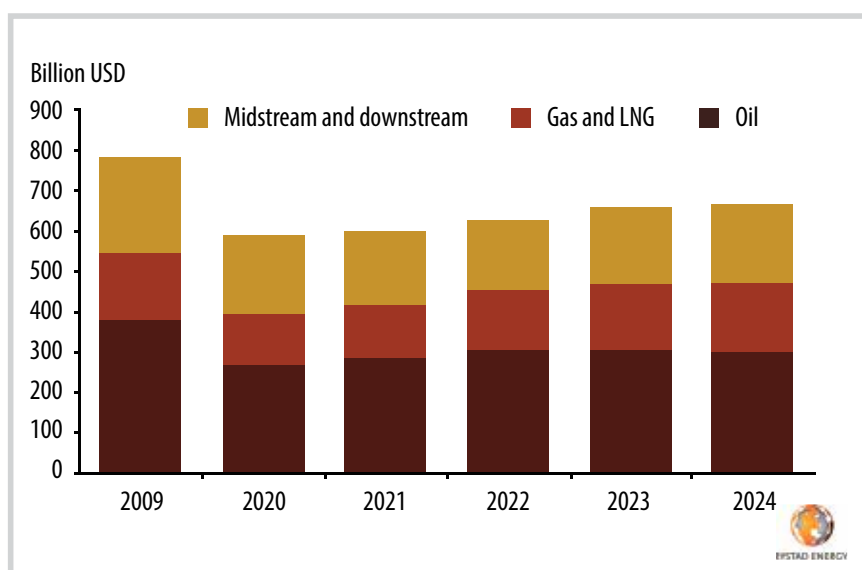


Figure 5. Global oil and gas investments by market [2].

The total volume of oil and gas achieving final investment decision (FID) increased by nearly 85% in 2021 to around 24 billion barrels of oil equivalent, reverting to the pre-pandemic level, with NOCs responsible for more than 75% of the total. This was underpinned by a push in the LNG export market, notably QatarEnergy's North Field East project and Gazprom continuing to progress Baltic LNG (although the future of the latter project is now in doubt).

Other development strategies have focused on projects with a short gap between investment and first production, that can make use of existing infrastructure and that can employ replication to lower costs.

For example, Shell Offshore Inc., a subsidiary of Royal Dutch Shell announced FID on its deepwater Whale field and aims to begin production within 2 years. The Whale development, owned by Shell Offshore Inc. (60% operator) and Chevron

U.S.A. Inc. (40%), is expected to reach peak production of approximately 100,000 barrels of oil equivalent per day and currently has an estimated recoverable resource volume of 490 million barrels of oil equivalent.

Eni announced plans to begin production from its 2021 discovery Baleine by 2023. The discovery well Baleine-1x, been drilled on the Baleine prospect, is the first exploration well drilled by Eni in the Ivory Coast, and the first commercial discovery in the country in 20 years. The potential of this discovery is estimated of over 2.0 billion barrels of oil in place and approximately 2.4 trillion ft³ (TCF) of associated gas, with potential upside.

ExxonMobil has made a final investment decision for the Yellowtail development offshore Guyana. The company's fourth and largest project in the Stabroek Block is expected to produce approximately 250,000 barrels of oil per day starting in 2025. Yellowtail production from the One Guyana floating production storage and offloading (FPSO) vessel will develop an estimated resource of more than 900 million barrels of oil. The USD 10 billion project will include 6 drill centres and up to 26 production and 25 injection wells. In many parts of the world, without a strong exploration funnel, FID opportunities will be increasingly limited in the future.

As regards US tight oil and shale gas, the number of rigs in operation is around 60% higher in the first quarter of 2022 than in the first quarter of 2021, but levels are still around 30% lower than in 2019, reflecting companies' focus on capital discipline and returning more revenue to shareholders. Private capital has grown from about one-quarter of investment in US shale between 2015 and 2019 to about one-third in 2021 [1].

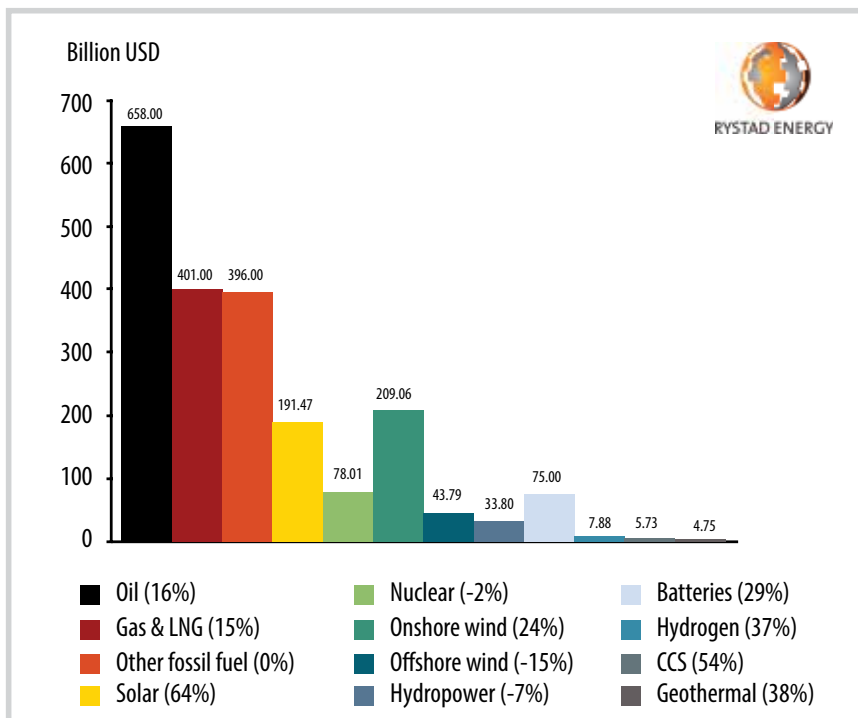


Figure 6. Forecast energy industry spending in 2022 by sub-sector [3].

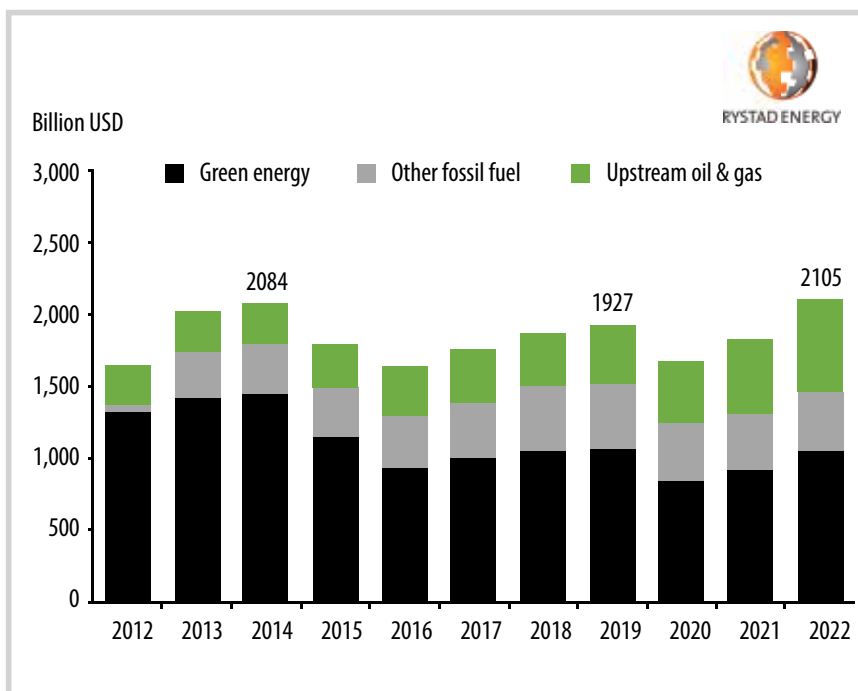


Figure 7. Energy industry spending by sector [3].

According to the Rystad Energy, global oil and gas investments will expand by USD 26 billion this year as the industry continues its protracted recovery from the worst of the pandemic. An analysis by Rystad Energy projects overall oil and gas investments will rise 4% to USD 628

billion this year from USD 602 billion in 2021 [2].

A significant factor behind the increase is a 14% increase in upstream gas and LNG investments. These segments will be the fastest-growing this year, with a jump in investments from USD 131

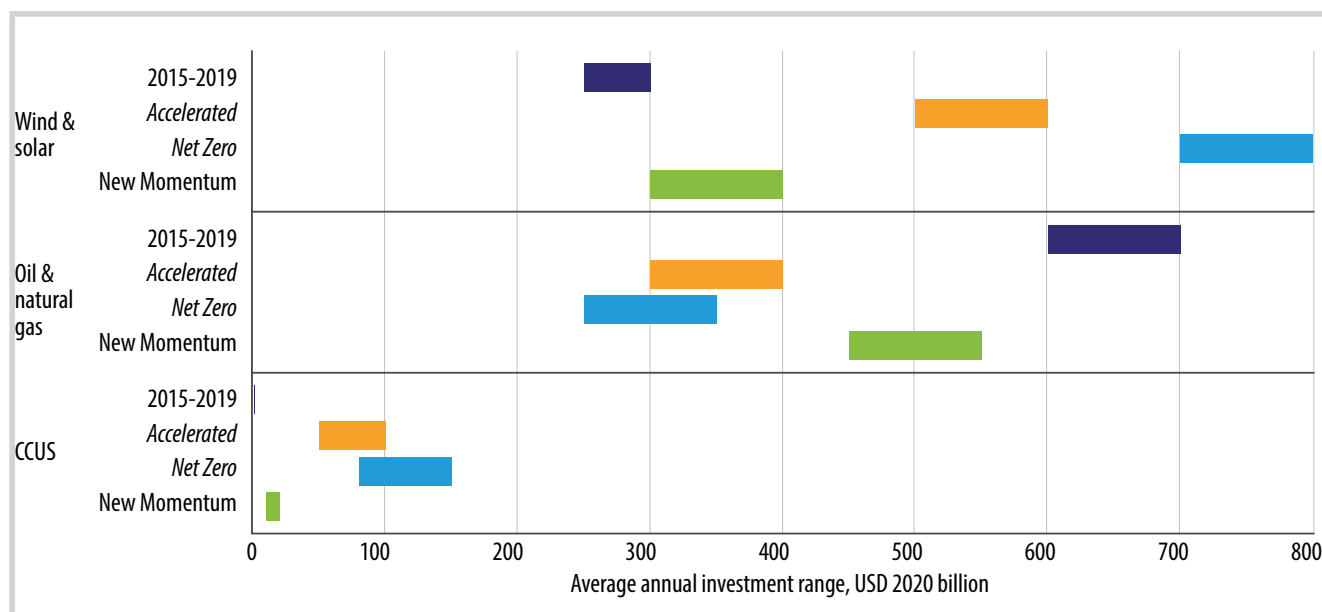


Figure 8. Average annual investment, history and 2020 - 2050 [5].

billion in 2021 to around USD 149 billion in 2022. Although this falls short of pre-pandemic totals, investments in the sector are expected to surpass 2019 levels of USD 168 billion in just 2 years, reaching USD 171 billion in 2024.

Upstream oil investments are projected to rise from USD 287 billion in 2021 to USD 307 billion this year, a 7% increase, while midstream and downstream investments will fall by 6.7% to USD 172 billion this year [2].

Drilling further into the numbers, global shale investments are forecasted to surge 18% in 2022, reaching USD 102 billion in 2022 compared with USD 86 billion in 2021. Offshore investments are set to increase 7%, from USD 145 billion to USD 155 billion, while conventional onshore will jump 8%, from USD 261 billion to USD 290 billion.

Regionally, Australia and the Middle East stand out, with Australia likely to see a jump in investments of 33%, thanks to greenfield gas developments. In the Middle East, investments will rise by an anticipated 22% this year as Saudi Arabia boosts its oil export capacity and

Qatar expands the production and export capacity of liquefied natural gas (LNG).

This year's investment growth is very much pre-programmed by the USD 150 billion worth of greenfield projects sanctioned in 2021, up from USD 80 billion in 2020. Sanctioning activity in 2022 is likely to closely match 2021 levels, with a similar amount of project spending to be unleashed over the short to medium term.

Sanctioning activity is set to rebound in North America, with over USD 40 billion worth of projects due for sanctioning in 2022. 6 LNG projects are expected to receive the green light, 5 in the United States and 1 in Canada. Offshore projects will also provide ample opportunities for contractors as TotalEnergies' North Platte project enters the final stage of its tender process and LLOG Exploration's Leon and Chevron's Ballymore developments in the US Gulf of Mexico look to proceed to the development phase in 2022. For Africa, however, 2022 is expected to be another quiet year with expected sanctioned projects worth a comparatively small USD 5 billion.

When it comes to offshore field sanctioning, there are around 80 projects worth a total of USD 85 billion in the global approvals pipeline for 2022. Of these, 10 are floating production storage and offloading units (FPSO), 45 involve subsea tiebacks, and 35 are grounded platforms. Latin America and Europe will be responsible for around 24% each of the total offshore sanctioning values next year, with deepwater expansions expected in Guyana and Brazil and Norway following recent tax changes.

For offshore contractors, the energy transition could be advantageous for wind power developments. Spending in the offshore wind sector reached almost USD 50 billion last year, double the 2019 levels. By 2025, we expect offshore wind investments will rise to USD 70 billion as demand for clean energy surges. By contrast, the offshore oil and gas sector is set to face a challenging energy transition period with oil demand likely to peak in the next 5 years, capping offshore investment at about USD 180 billion in 2025 [2].

Surging oil, gas and power prices

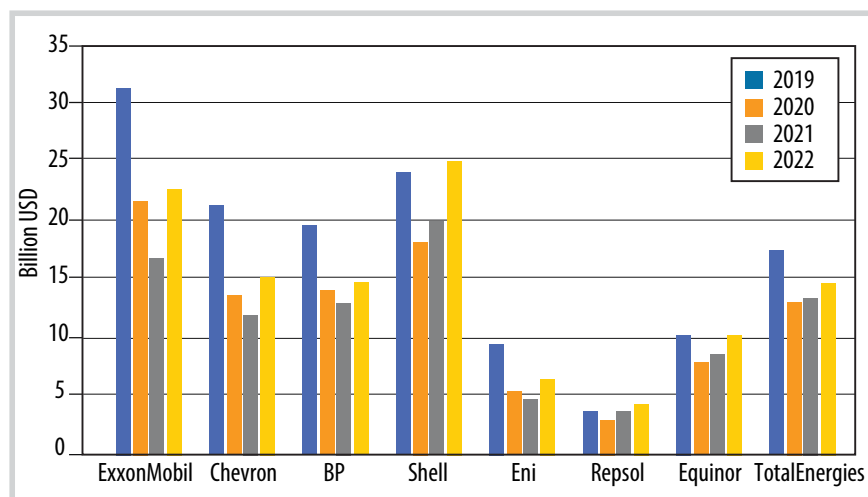


Figure 9. Total capital spending by major oil companies [6].

together with the European Union (EU)'s goals of becoming less dependent on Russian supplies and post-Covid-19 pandemic inflation will catapult global energy spending this year to USD 2.1 trillion, according to Rystad Energy's research. Upstream oil and gas spending is now projected to grow 16% - or USD 142 billion - compared to last year as oil and gas producers around the world up their investment budgets to increase output [3].

According to the IHS Market, global energy sector spending is forecast for 18% growth in 2021 - 2025 compared to the previous five-year period. Fossil fuel capital expenditure is projected to garner the most spending totalling USD 2.2 trillion in 2021 - 2025. Total upstream spending is expected to be 21% higher than transmission and distribution and outpace renewable spending by 36% in 2021 - 2025 [4].

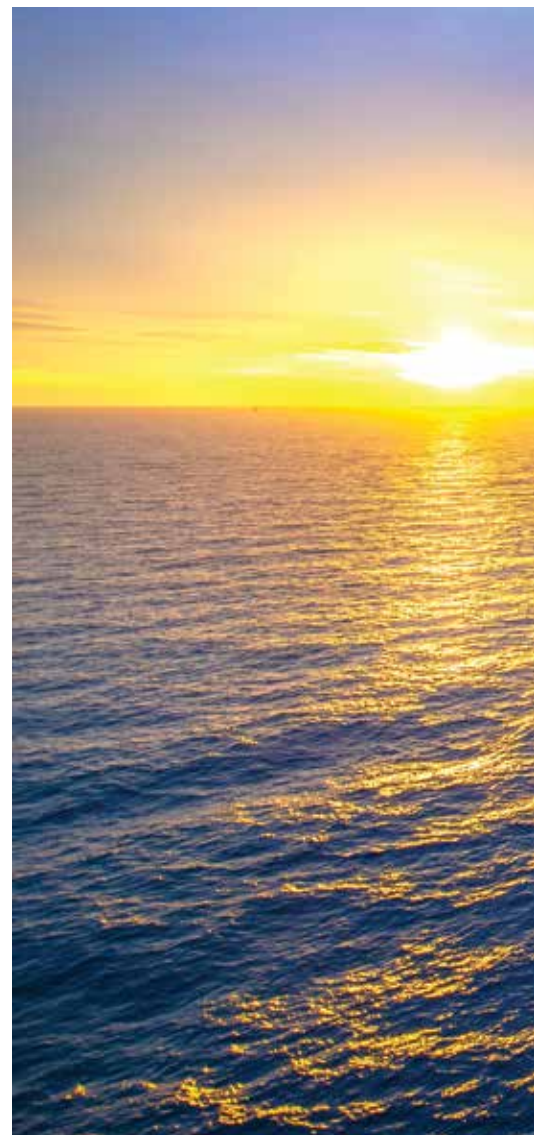
Oil demand increases to above its pre-Covid-19 level before falling further out. Declines in oil demand are driven by the increasing efficiency and electrification of road transportation. Natural declines in existing hydrocarbon production imply continuing investment in new upstream oil and gas is required over the next 30

years. The average annual investment in upstream oil and gas over the next 10 years consistent with the three scenarios is around USD 375 - 500 billion, compared with around USD 415 billion in 2020 [5].

According to OGJ [6], total capital spending by major oil companies, including ExxonMobil, Chevron, Shell, BP, Eni, Equinor and TotalEnergies, will rebound 24% in 2022 to USD 112.7 billion, but still below 2019 the pre-pandemic level of USD 136 billion (Figure 9).

ExxonMobil expects capital investments of USD 21 - 24 billion in 2022, and USD 20 - 25 billion per year through 2027. Cash flow and earnings from upstream operations are expected to increase, thanks to aggressive cost reductions and favourable investments in low-cost supply projects in Guyana, Brazil, and the Permian basin. Permian production growth is to be accelerated, guided to grow 25% in 2022 [7].

According to ExxonMobil, more than 90% of upstream planned capital investments through 2027 are expected to generate returns of greater than 10% at prices less than or equal to USD 35 per barrel of oil equivalent, while reducing upstream greenhouse gas (GHG)



emissions intensity by 40 - 50% through 2030, compared to 2016 levels. As part of its plan, ExxonMobil has committed USD 15 billion for lower-emission investments through 2027.

Chevron's capital and exploratory spending for 2022 is set at USD 15 billion, up from USD 11.7 billion in 2021 and USD 13.5 billion in 2020. The 2022 capital program includes about USD 800 million in lower carbon spending. In 2022, Chevron plans to spend USD 6.4 billion in US upstream and USD 6.2 billion in international upstream, respectively. In 2021, 2020, and 2019, US upstream spending was USD 4.7 billion, USD 5.1

Source: Shutterstock



billion, and USD 8.2 billion, respectively. Over the years, international upstream spending was USD 4.9 billion, USD 5.8 billion, and USD 9.6 billion, respectively.

Of the upstream business this year, about USD 8 billion is allocated to currently producing assets, with about USD 3 billion for Permian basin unconventional development and about USD 1.5 billion for other shale and tight assets around the world. In addition, USD 3 billion of the upstream program is planned for ongoing major capital projects, of which about USD 2 billion is related to projects at Tengiz field in Kazakhstan. Finally, some USD 1.5 billion is set for

exploration, early-stage development projects, midstream activities, and carbon reduction opportunities.

ConocoPhillips expects capital expenditures of USD 7.2 billion in 2022, up from USD 5.3 billion in 2021. The increase reflects the addition of Shell's Permian basin properties and other investments. The capital plan includes funding for ongoing development drilling programs, major projects, exploration and appraisal activities, base maintenance.

Capital expenditures by NOCs, led by Middle Eastern companies, are increasing in 2022. According to the results of a poll of 170 oil and gas companies conducted

by Barclays Bank in the period from 16th November to 14th December 2021, Kuwait Oil Co. reduced spending by 42% in 2021 and plans to increase capital spending by 30% to USD 4.6 billion in 2022. Efforts to increase capacity to 3.5 million barrels per day by 2025 from the current 2.6 million barrels per day drives the increase in capital expenditures.

Abu Dhabi National Oil Co. (ADNOC) has similar plans to increase production levels to 5 million barrels per day by 2030 from the current 4.2 million barrels per day. ADNOC expects to increase its capital spending by 11% to USD 8 billion in 2022.

Saudi Aramco plans to boost its

capital spending to USD 40 - 50 billion in 2022, with further growth expected until around the middle of the decade. Saudi Aramco also wants to raise crude oil "maximum sustainable capacity" to 13 million barrels per day by 2027 and boost gas production by more than 50% by 2030 [8].

Capital expenditures in Latin America are expected to increase by 28% to USD 24.8 billion in 2022, following an increase of 17% in 2021, according to the Barclays survey. In addition to increased capital spending of Latin American companies, the majors and North American independents are stepping up development offshore Guyana, Suriname, and Brazil.

Petrobras is raising its 2022 - 2026 capital spending plan to USD 60 - 70 billion from the current USD 55 billion program for the 2021 - 2025 period, with a major focus on exploration and production in Brazil's presalt area.

References

- [1] IEA, "World energy investment 2022", 6/2022. [Online]. Available: <https://www.iea.org/reports/world-energy-investment-2022>.
- [2] Rystad Energy, "Global oil and gas investments to hit \$628 billion in 2022, led by upstream gas and LNG", 11/1/2022. [Online]. Available: <https://www.rystadenergy.com/newsevents/news/press-releases/Global-oil-and-gas-investments-to-hit-628-billion-in-2022-led-by-upstream-gas-and-LNG/>.
- [3] Rystad Energy, "Global energy spending set to reach record high of over \$2 trillion in 2022, led by oil and gas", 7/4/2022. [Online]. <https://www.rystadenergy.com/newsevents/news/press-releases/global-energy-spending-set-to-reach-record-high-of-over-2-trillion-in-2022-led-by-oil-and-gas/>.
- [4] IHS Market, "Global energy sector capex poised for a strong rebound", 4/3/2022. [Online]. Available: <https://ihsmarkit.com/research-analysis/global-energy-sector-capex-strong-rebound.html>.
- [5] BP, "Energy outlook 2022". [Online]. Available: <https://www.bp.com/content/dam/bp/business-sites/en/global/corporate/pdfs/energy-economics/energy-outlook/bp-energy-outlook-2022.pdf>.
- [6] Conglin Xu, "Oil, gas companies to boost spending in 2022", 4/4/2022. [Online]. Available: <https://www.ogj.com/general-interest/economics-markets/article/14270831/oil-gas-companies-to-boost-spending-in-2022>.
- [7] ExxonMobil, "ExxonMobil details plans to lead in earnings and cash flow growth, energy transition", 2/3/2022. [Online]. Available: https://corporate.exxonmobil.com/News/Newsroom/News-releases/2022/0302_ExxonMobil-details-plans-to-lead-in-earnings-and-cash-flow-growth-energy-transition.
- [8] Saeed Azhar and Maha El Dahan, "Saudi Arabia hikes oil investments as it profits from price surge", 20/3/2022. [Online]. Available: <https://www.reuters.com/business/energy/saudi-aramco-2021-profit-soars-higher-oil-prices-2022-03-20/>.



Connecting Resources - Transferring Knowledge

Established in 2011, **Advanced Training Center (ATC)** is a part of PetroVietnam University (PVU). ATC has the function of organising advanced and specialised training in the fields of oil and gas and energy. With a team of prestigious domestic and foreign lecturers, ATC focuses on designing training programs on engineering, technology, operation, optimisation and lean production, maintenance, and repairing construction in upstream, midstream, and downstream, transportation, distribution, technical services, and HSE. In addition, ATC regularly updates programs to improve leadership, management, and professional skills for human resources, solutions for digital transformation, energy transition, and recreate its organisational culture for businesses to achieve breakthrough and sustainable growth. ATC has the mission of "connecting resources - transferring knowledge", synthesising intellectual strength in the industry nationwide and worldwide, contributing to the development of high-quality human resources for Petrovietnam and Vietnam's oil and gas industry. The Center has always improved and applied modern models and methods in new contexts to bring practical values to learners, managers, and businesses.

PETROVIETNAM UNIVERSITY (PVU)- ADVANCED TRAINING CENTER (ATC)
762 Cach Mang Thang Tam street, Long Toan ward, Ba Ria city, Ba Ria - Vung Tau province
Tel: (+84-25) 43738879 | Fax: (+84-25) 43733579 | Mobile: (+84) 909656998 | Email: atc@pvu.edu.vn
Ho Chi Minh: VPI Office in HCMC, Lot E2b-5, D1 street, Saigon Hi-Tech Park, Tan Phu ward, Thu Duc city
Hanoi: VPI Tower, 167 Trung Kinh street, Yen Hoa ward, Cau Giay district
Website: www.atc.pvu.vn | FB: <https://www.facebook.com/Petroexperts>

INVITATION TO WRITE FOR THE PETROVIETNAM JOURNAL

Petrovietnam Journal is the official scientific journal of the Vietnam Oil and Gas Group (Petrovietnam). Over 40 years of establishment and development, the Petrovietnam Journal has affirmed the role of the first national publication of the Vietnam Oil and Gas sector, which publishes the results of domestic scientific and technological researches and introduces scientific and technological advances in the domestic and international petroleum industries.

The Petrovietnam Journal releases monthly in Vietnamese (10 issues/year) and English (2 issues/year). The Journal's readers are the Party's and the State's leaders; Vietnamese and international management agencies, research and training institutions in the oil and gas sector; leaders of Petrovietnam and its member units; scientists, officers and employees of the oil and gas industry and others, oil and gas contractors, joint venture companies, international organisations, foreign businesses and investors.

The content of the Petrovietnam Journal covers all aspects of Petrovietnam's activities:

- ▶ *The orientations for Petrovietnam's development;*
- ▶ *Achievements in scientific research and technological development from upstream to downstream as well as petroleum economic and management studies;*
- ▶ *Experiences and initiatives of technical improvement and application of scientific research results, innovations and inventions, and measures to improve organisation and management in order to enhance the efficiency of production and business;*
- ▶ *Information about scientific and technological advances in the world's oil and gas sector;*
- ▶ *Production and business activities of Petrovietnam;*
- ▶ *Information about products and services of Petrovietnam.*

Along with the development of the Vietnam Oil and Gas Group, the Petrovietnam Journal has become a scientific and technological forum for Vietnam's oil and gas sector, and also the voice of the scientists as well as businesses producing and trading in oil and gas in Vietnam and abroad.

In order to meet the readers' demand for information, the Petrovietnam Journal looks forward to receiving the enthusiastic collaboration of scientists, officers, and employees inside and outside the industry. Every author, every article will practically contribute to the development of the oil and gas industry, and be a bridge between Vietnam's oil and gas industry and international friends and partners.

With our sincere thanks,